UNIVERSITY OF CALIFORNIA, SAN DIEGO

Non-Foster Circuits for High Performance Antennas: Advantages and Practical Limitations

A dissertation submitted in partial satisfaction of the
requirements for the degree of
Doctor of Philosophy

in

Electrical Engineering (Communication Theory and Systems)

by

Minu Mariam Jacob

Committee in charge:

Professor Daniel F. Sievenpiper, Chair
Professor James Buckwalter
Professor Gert Cauwenberghs
Professor Brian G. Keating
Professor Vitaliy Lomakin

2016

The Dissertation of Minu Mariam Jacob is approved and is acceptable in quality and form for publication on microfilm and electronically:

_____

_____

_____

_____

_____

Chair

University of California, San Diego

2016

DEDICATION

To my parents and my sisters

TABLE OF CONTENTS

LIST OF FIGURES

LIST OF TABLES

ACKNOWLEDGEMENTS

I consider it a privilege and a blessing to have had Prof. Daniel Sievenpiper as my advisor throughout my graduate program. His technical vision, breadth of experience and his ability to see the big picture and the heart of any research topic is matched by his patience, unwavering support and encouragement. I am truly grateful to him for enabling me to come this far.

I would also like to thank my committee members Prof. James Buckwalter, Prof. Gert Cauwenberghs, Prof. Brian G. Keating and Prof. Vitaliy Lomakin for taking the time to offer suggestions and comments over the years.

I am very thankful to Prof. Gabriel Rebeiz and his students for letting me borrow their equipment and use their lab space whenever I was in a pinch.

The course of my PhD has been greatly enriched by the wonderful people at the Applied Electromagnetics Lab, from whom I've learnt many things and with whom I've spent many enjoyable hours. I would especially like to thank Jiang Long for being so helpful and supportive in our joint struggle to understand non-Foster circuits, and for answering my incessant questions.

Over the years, I've been very lucky to have made some great friends at UCSD. The trips we've taken, the fun weekends and the many coffees shared have in no small part helped me retain my sanity. I hope these friendships continue over to the next phase of our lives.

And finally to my family - I dedicate this thesis to them. To my sister Deepa for convincing my father that it was a good idea for me to come to UCSD, for giving me a home away from home and for being my emergency contact in every way. To my sister Simi for her ability to comfort me in any situation, for her faith in me and for her patronage which allowed me to survive during lean times. To my brothers-in-law Joji and Prathap, and my nephews Ari and Rehan for filling my holidays with warmth,

laughter and love. To my mother for being my greatest ally, my best teacher and my greatest support. To my father for being my rock, for giving me the opportunities to pursue my dreams and for inspiring me through his life. I love you both.

The material in this dissertation is based on the following papers which are either published, under review or in preparation for submission.

Chapter 3 is based on and mostly a reprint of the paper: M. M. Jacob, J. Long, and D. F. Sievenpiper, "Non-Foster Loaded Parasitic Array for Broadband Steerable Patterns," *Antennas and Propagation, IEEE Transactions on*, vol. 62, pp. 6081-6090, 2014.

In Chapter 4, Section 4.1 and Section 4.3 are based on the paper: M. M. Jacob and D. F. Sievenpiper, "Gain and Noise Analysis of Non-Foster Matched Antennas," under review at *Antennas and Propagation, IEEE Transactions on*.

Chapter 5 is based on the paper: M. M. Jacob and D. F. Sievenpiper, "Gain and Noise Analysis of Non-Foster Matched Antennas," under review at *Antennas and Propagation, IEEE Transactions on*.

Chapter 6 is based on the following papers: M. M. Jacob, J. Long, and D. F. Sievenpiper, "Nonlinear effects of non-Foster matching networks," in *Antennas and Propagation and USNC/URSI National Radio Science Meeting, 2015 IEEE International Symposium on*, 2015, pp. 1248-1249 ; M. M. Jacob and D. F. Sievenpiper, "Non-Foster Matched Antennas for High-Power Applications," in preparation.

The dissertation author was the primary author of the work in these chapters, and co-authors have approved the use of the material for this dissertation.

VITA

2009	Bachelor of Technology, Amrita School of Engineering, Coimbatore, India.
2011	Master of Science in Electrical Engineering, University of California, San Diego, USA.
2011–2016	Research Assistant, University of California, San Diego
2016	Doctor of Philosophy, University of California, San Diego

PUBLICATIONS

M. M. Jacob and D. F. Sievenpiper, "Non-Foster Matched Antennas for High-Power Applications," in preparation.

M. M. Jacob and D. F. Sievenpiper, "Gain and Noise Analysis of Non-Foster Matched Antennas," under review at *Antennas and Propagation, IEEE Transactions on*.

M. M. Jacob, J. Long, and D. F. Sievenpiper, "Nonlinear effects of non-Foster matching networks," in *Antennas and Propagation and USNC/URSI National Radio Science Meeting, 2015 IEEE International Symposium on*, 2015, pp. 1248-1249.

M. M. Jacob, J. Long, and D. F. Sievenpiper, "Non-Foster Loaded Parasitic Array for Broadband Steerable Patterns," *Antennas and Propagation, IEEE Transactions on*, vol. 62, pp. 6081-6090, 2014.

M. M. Jacob, J. Long, and D. F. Sievenpiper, "Noise in non-Foster antenna matching circuits," in *Antennas and Propagation Society International Symposium (APSURSI), 2013 IEEE*, 2013, pp. 2205-2206.

Minu Jacob, Jiang Long, Dan Sievenpiper, Broadband Non-Foster Matching of an Electrically Small Loop Antenna, in *Proc. IEEE Antennas Propag. Soc. Int. Symp. (APSURSI)*, 2012.

Jiang Long; **Jacob, M. M.**; Sievenpiper, D.F., "Broadband Fast-Wave Propagation in a Non-Foster Circuit Loaded Waveguide,"*Microwave Theory and Techniques, IEEE Transactions on*, vol.62, no.4, pp.789,798, April 2014.

G. Fei, Z. Fushun, L. Jiang, **M. Jacob**, and D. Sievenpiper, "Non-dispersive tunable reflection phase shifter based on non-Foster circuits," *Electronics Letters*, vol. 50, pp.

1616-1618, 2014.

Jiang Long, **Minu Jacob**, Dan Sievenpiper, Electronically Steerable Antenna Using Superluminal Waveguide and Tunable Negative Capacitors, in *Proc. IEEE Antennas Propag. Soc. Int. Symp. (APSURSI)*, 2012.

D. F. Sievenpiper, D. C. Dawson, **M. M. Jacob**, T. Kanar, S. Kim, J. Long and R. G. Quarfoth, "Experimental Validation of Performance Limits and Design Guidelines for Small Antennas," *Antennas and Propagation, IEEE Transactions on*, vol. 60, pp. 8-19, 2012.

D. Sievenpiper, **M. Jacob** and J. Long, "Active electromagnetic structures, metamaterials, and antennas," *Antenna Technology (iWAT), 2012 IEEE International Workshop*, 2012, pp. 289-292.

ABSTRACT OF THE DISSERTATION

Non-Foster Circuits for High Performance Antennas: Advantages and Practical Limitations

by

Minu Mariam Jacob

Doctor of Philosophy in Electrical Engineering (Communication Theory and Systems)

University of California, San Diego, 2016

Professor Daniel F. Sievenpiper, Chair

The demand for miniaturized, broadband communication systems has created a need for electrically small, broadband antennas. However, all passive electrically small antennas have a fundamental gain-bandwidth limitation related to their electrical size, as first described by Wheeler and Chu. This limitation can be overcome using active non-Foster circuits (negative inductors and/or negative capacitors), which can deliver a broadband input match with active matching techniques, or can help reduce phase dispersion using negative delay effects. This thesis will illustrate the advantages of non-Foster circuits in obtaining broadband small antennas, in addition to examining their

practical limitations due to noise in receive applications, and nonlinearity in transmit applications.

Chapter 1

Introduction

An increasing demand for smaller, faster communication systems has resulted in rapid developments in the field of semiconductor devices, leading to high performance analog and digital systems with steadily shrinking form factors. However, the antenna is an intrinsic component of communication systems with fundamental performance limitations based on the physical size at the operating wavelength. This limitation becomes especially restrictive as the antenna's physical size becomes comparable to the operating wavelength. In antenna arrays, variation in phase delays with frequency (phase dispersion) also causes bandwidth limitations. Therefore it is important to study the physical limitations of antennas, and develop novel techniques to bypass those limitations.

1.1 Small Antennas

In 1947, Wheeler defined a small antenna as one whose maximum dimension is smaller than the radianlength, where the radianlength is defined as the wavelength divided by 2π [1, 2]. He then characterized such an antenna as a lumped capacitor or inductor with an associated radiation resistance, and derived the maximum radiation power factor of that antenna. The maximum radiation power factor is equivalent to the inverse of the minimum quality factor of that antenna. These findings where echoed by Chu [3], who used spherical wave functions to identify a theortical minimum bound on

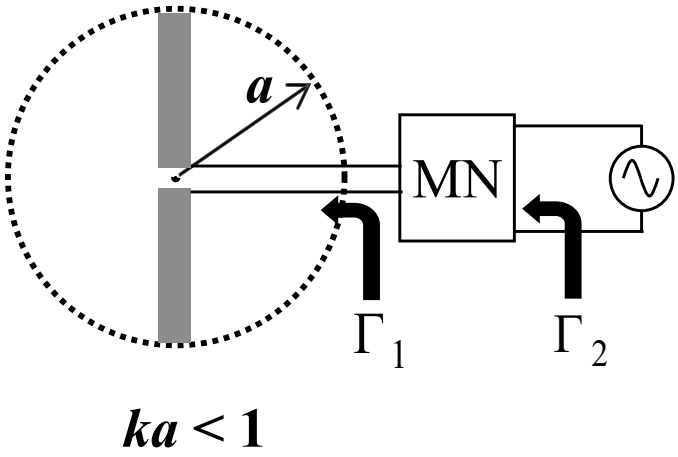

Figure 1.1. Impedance matching network for a small antenna

the quality factor of a small antenna. Further work by Hansen[4], McLean[5] and others [6] culminated in the closed form equation for the minimum achievable quality factor for a small antenna of electrical size *ka* as given below.

$$Q_{min} = \frac{1}{ka} + \frac{1}{n(ka)^3}. \tag{1.1}$$

Here k is the wave number, equivalent to the inverse of the radianlength, a is the radius of a sphere that circumscribes the antenna and n is either 1 or 2 depending on the number of modes contained within the antenna.

Since a small antenna has $ka < 1$, it has an intrinsically large quality factor as evident from (1.1). This is the minimum achievable quality factor, leading to an upper bound on the maximum achievable bandwidth for a small antenna of size ka. If the antenna is lossy, the bandwidth 'increases' at the cost of reduced effficiency η of the antenna. Further, the bandwidth also 'increases' by tolerating a lower quality match, leading to a higher reflection coefficient Γ_1 in Fig. 1.1 and a corresponding increase in the voltage standing wave ratio ($VSWR$). Therefore, a figure of merit that takes into account the efficiency and reflection coefficient can be given as [7, 8]

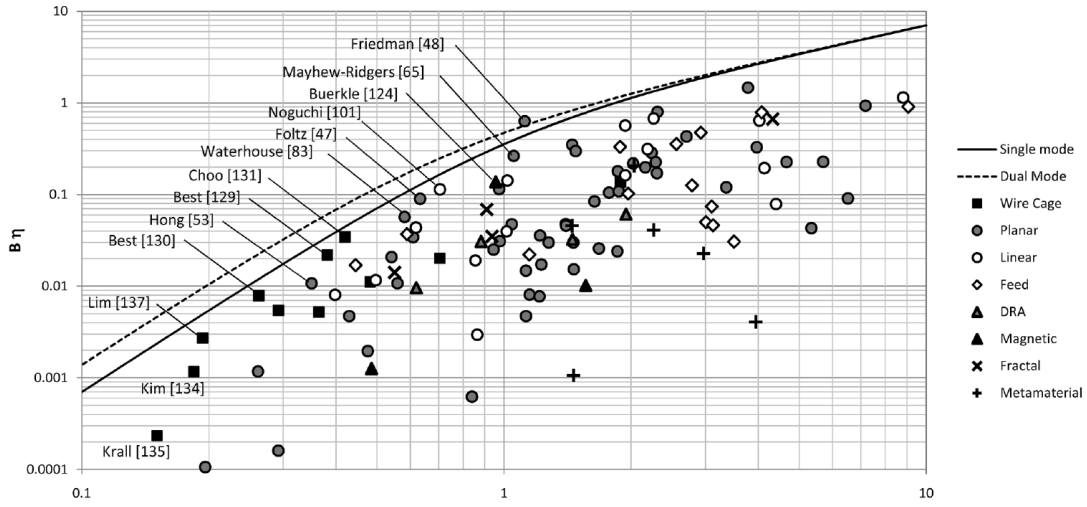

Figure 1.2. Bandwidth-efficiency product for published small antenna designs [8]

$$B\eta = \frac{1}{Q}\left(\frac{VSWR-1}{\sqrt{VSWR}}\right). \tag{1.2}$$

where B is the fractional bandwidth of the self-matched antenna. Using (1.2) and (1.1), the maximum achievable bandwidth for a small antenna of size ka and a given efficiency η can be obtained for a required VSWR. This was then compared to the bandwidth-efficiency of published small antenna designs with measured bandwidth results, as shown in Fig. 1.2 taken from [8]. The results confirm the Wheeler-Chu bandwidth limits for self-matched small antennas. However, this bandwidth can be further improved with additional matching networks (Fig. 1.1).

The large quality factor of a small antenna results in an antenna impedance with a large reactance and a small radiation resistance. Intuitively, it can be understood that a large reactance leads to a narrow band impedance match with conventional passive matching techniques. The maximum achievable bandwidth for a load of quality factor Q using an infinite-tuned lossless passive matching network is given by the Bode-Fano limit [9, 10],

$$B \leq \frac{1}{Q} \frac{\pi}{\ln\left(\frac{1}{\Gamma_{max}}\right)}, \tag{1.3}$$

Here Γ_{max} is the maximum allowable reflection coefficient, given by Γ_2 in Fig. 1.1.

Thus, high Q small antennas have a small maximum achievable impedance matching bandwidth B as dictated by (1.3). However, this limit only applies to passive matching techniques.

1.2 Non-Foster Elements

Foster's reactance theorem [11] states that all lossless passive two-terminal devices must have an impedance with a reactance and susceptance that has a positive slope with frequency. An element that violates this property by having a reactance which has a negative slope with frequency is therefore called a 'non-Foster' element. If one could think of a 'negative inductor' whose reactance is $-j\omega L$, such an element would be a non-Foster element. A 'negative capacitor' of reactance $\frac{j}{\omega C}$ would also be a non-Foster element. On the Smith Chart (Fig. 1.3), it can be seen that the impedance of Foster inductors and capacitors goes clockwise with frequency, whereas that of non-Foster elements goes counter-clockwise with frequency. This remarkable property leads to many interesting and novel applications.

1.2.1 Advantages

Non-Foster reactances with a negative frequency slope can be used to completely cancel equivalent Foster reactances with a positive frequency slope. Therefore non-Foster reactances can be used to achieve very high bandwidths in impedance matching applications [12]. The counter-clockwise direction of non-Foster elements on the Smith Chart can also be characterized as a 'negative delay'. The reflection phase from

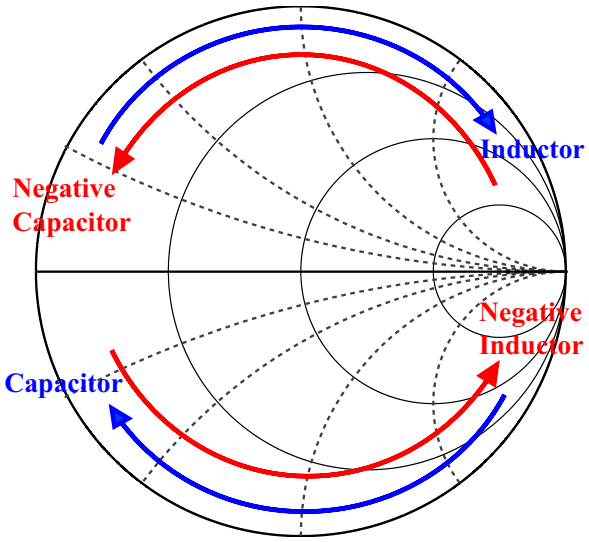

Figure 1.3. Foster and non-Foster elements on a Smith Chart

non-Foster elements has a positive slope with frequency, which can be used to cancel conventional phase delays with negative slopes, resulting in reduced phase dispersion [13]. A transmission line loaded with non-Foster elements can be used to realize a non-dispersive fast-wave transmission line [14], which can be used to design squint-free leaky wave antennas [15] and true time delay components in squint-free arrays [16].

Negative inductors and negative capacitors do not exist as passive components in nature, and must therefore be generated using active circuits. The most popular circuit is the Negative Impedance Convertor (NIC) circuit introduced by Linvill [17], employing a cross-coupled transistor topology to negate an attached RLC network. This circuit will be reviewed in detail in Chapter 2, followed by details on performance advantages with non-Foster loaded antennas in Chapters 3 and 4.

1.2.2 Limitations

The cross-coupled transistor topology of the Negative Impedance Convertor circuit uses positive feedback to generate non-Foster impedances. This however results in very sensitive stability issues, which will be discussed in various sections throughout

this thesis. Further, the active transistors generate noise which can degrade performance in certain small signal applications, as discussed in detail with reference to non-Foster matched receive antennas in Chapter 5. Active devices also have nonlinearity issues, which become evident in high power applications. This has been discussed with reference to non-Foster matched transmit antennas in Chapter 6.

1.3 Dissertation Organization

This thesis presents the design and applications of non-Foster circuits for high performance antennas, and objectively analyzes their true performance advantage taking into account the limitations of the non-Foster circuit.

Chapter 1 introduces the fundamental bandwidth limitations of small antennas, and also introduces non-Foster circuits with some of their performance-enhancing traits in antenna applications.

Chapter 2 presents design, simulation and measurement results of non-Foster negative inductor circuits and details two antenna applications with such circuits.

Chapter 3 presents the non-Foster loaded parasitic array that uses non-Foster elements to cancel phase dispersion and achieve an instantaneous broadband squint-free pattern.

Chapter 4 presents non-Foster matched small antennas with two design examples that exhibit broadband matching bandwidths that overcome the Wheeler-Chu bandwidth limit.

Chapter 5 examines the advantage of broadband non-Foster matched antennas in receive applications. A noise model is shown for the general non-Foster circuit, and received signal to noise ratio (SNR) comparisons have been shown between a non-Foster matched small antenna and a gain-enhanced small antenna to assess the true performance advantage with non-Foster matching.

Chapter 6 explores the performance of broadband non-Foster matched antennas in transmit applications, presenting measured results of input match variation and non-linear tone generation at high power. The gain and output third order intercept point (OIP3) of the non-Foster matched antenna attached to a transmit amplifier have been compared to that of the unmatched antenna attached to a transmit amplifier.

Chapter 7 summarizes the conclusions and discusses directions for future research on non-Foster applications for antennas.

Chapter 2

Non-Foster Circuits: Design and Applications

Non-Foster impedances cannot be obtained with passive devices, and must therefore be generated using active circuits. Extensive studies have been done on the cross-coupled transistor topology first introduced by Linvill [17] as the Negative Impedance Convertor (NIC) circuit used to generate non-Foster impedances. In this chapter, we will present measurement results of NIC circuits for a -30 nH negative inductor and a tunable negative inductor that tunes from -60 nH to -30 nH. Two applications of negative inductors will be shown, which will be further expanded in the following two chapters.

2.1 Non-Foster Circuit Topology

All active circuits that generate non-Foster impedances work on the basic principle of inverting the current through a load while maintaining the voltage across it, or of inverting the voltage across a load and maintaining the current through it, leading to a negated load impedance. The Negative Impedance Convertor has the basic topology shown in Fig. 2.1 [17, 18, 19, 20, 12]. It can be configured either as a one-port network (unbalanced) to be used as a shunt element, or as a two-port network (balanced) to be

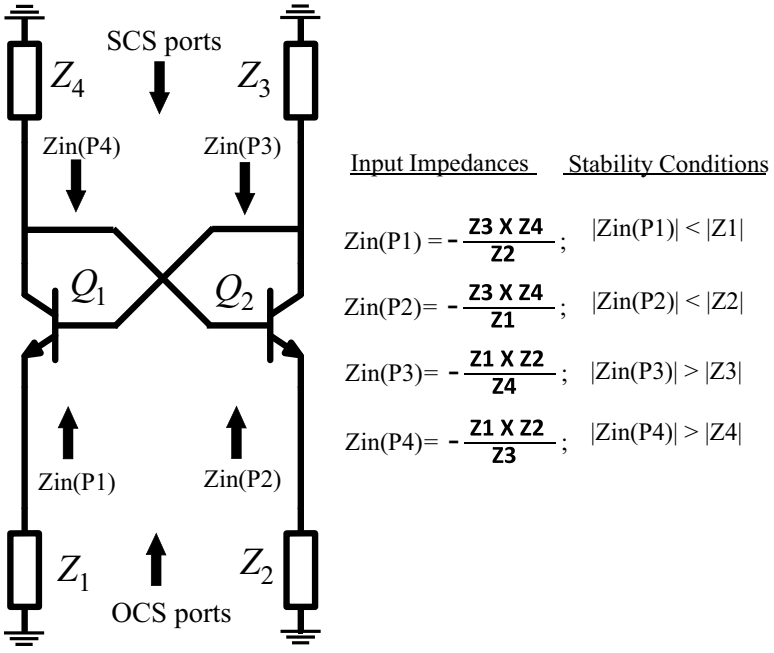

Figure 2.1. Circuit topology of a Negative Impedance Convertor(NIC) circuit with the associated input impedances and stability conditions

used a floating series element. When used as a single-ended one-port network, the input impedance at each of the 4 ports has the simplified form shown in Fig. 2.1. More detailed equations on the input impedance of the NIC in the balanced and unbalanced mode will be presented in Chapter 6.

It can be seen from Fig. 2.1 that the NIC has a positive feedback network. This leads to instability unless the NIC is properly loaded with the required impedances to guarantee stability. Many techniques to analyze and ensure stability have been shown in [21, 22, 23]. There are two basic simplified conditions for stability: (1) If the input to the NIC is at the emitter of the transistor, the NIC will be open circuit stable (OCS) by ensuring that the NIC sees an open circuit at its input. (2) If the input to the NIC is at the base-collector junction, the NIC will be short circuit stable (SCS) by ensuring that the NIC sees a short circuit at its input. These are the extreme conditions however, and stability is usually achieved by connecting a load with a larger impedance magnitude than

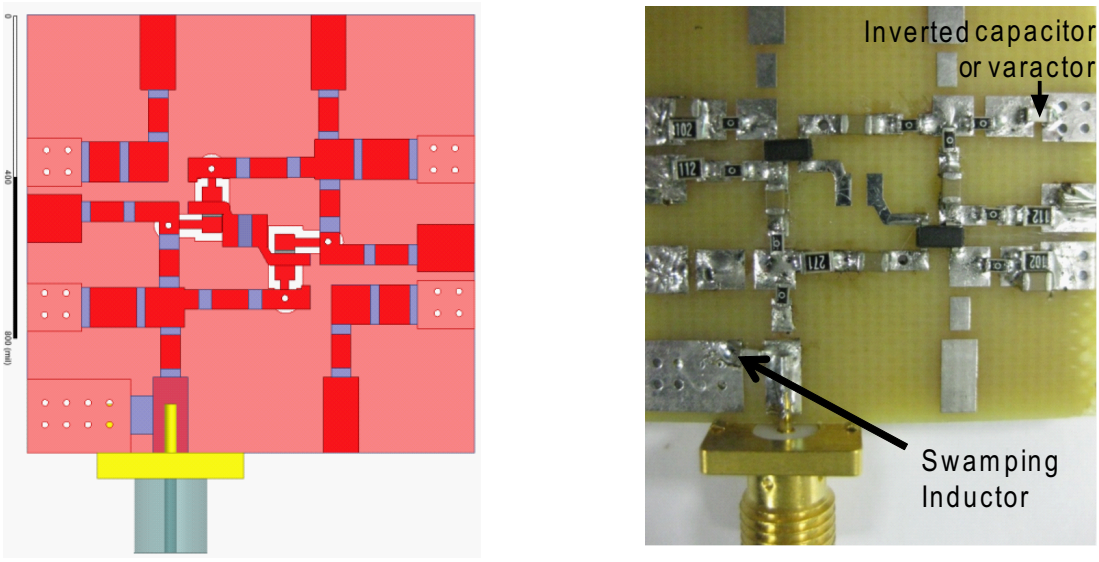

(a) (b)

Figure 2.2. (a) Co-simulation model of the NIC. (b) Fabricated circuit of a negative inductor

that of the input impedance at the OCS ports, and by connecting a load with a smaller impedance magnitude than that of the input impedance at the SCS ports. Care must be taken to ensure that the impedance conditions are satisfied throughout the bandwidth of operation of the NIC.

2.2 Circuit Simulation and Measurement

The design of an NIC circuit for a specific required impedance must take into account the parasitics of the circuit layout and those of the attached devices. An accurate simulation technique that closely matched measurements was obtained by first doing a full-wave simulation of the generalized layout in Ansys HFSS [24] as shown in Fig. 2.2(a), using lumped ports (gray patches) in place of the attached devices. Accurate device models from the vendors are later attached to the full-wave model using co-simulation techniques in Keysight ADS [25]. The layout was fabricated on 64 mil FR-4 substrate as shown in Fig. 2.2(b). The fabricated circuit (and simulation model)

has a swamping impedance which is attached to ensure stability, and which will be de-embedded after measurements to calculate the generated non-Foster impedance.

2.2.1 Fixed Negative Inductor

A -30 nH circuit was designed using techniques presented in [12], wherein tuning elements are used to control the loss and bandwidth of the circuit. In general, a non-Foster circuit has trade-offs between bandwidth, loss and 'flatness' of the negative inductance value or negative capacitance value across the bandwidth of operation of the NIC. This particular circuit was designed to optimize for bandwidth and flatness of the negative inductance, and therefore the loss is not an optimum value. However the loss can be reduced by sacrificing some of the other figures of merit.

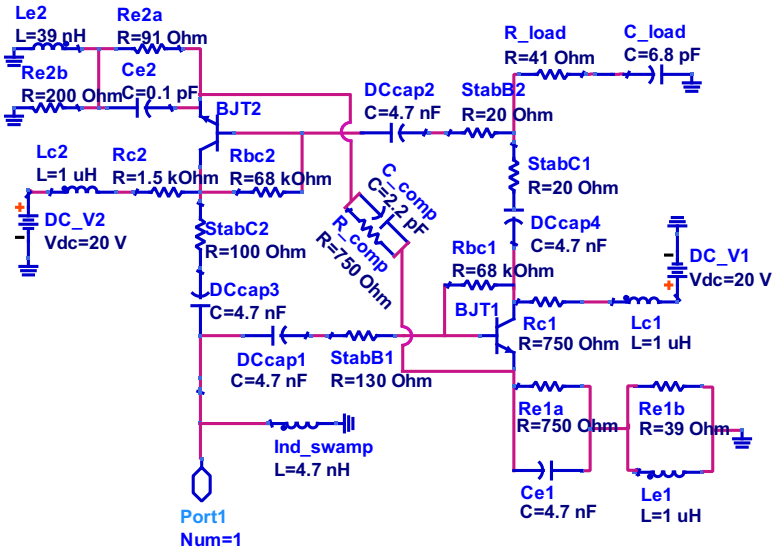

Figure 2.3. Negative inductor schematic

The circuit schematic is as shown in Fig. 2.3. It is configured as a short circuit stable (SCS), unbalanced NIC with a swamping inductance of 4.7 nH at the input. Resistive loss has been added in the cross-coupled paths to reduce the feedback gain for stability. The negative inductance is generated by inverting the capacitor *C_load* in the schematic. The simulated and measured results are shown in Fig. 2.4 after

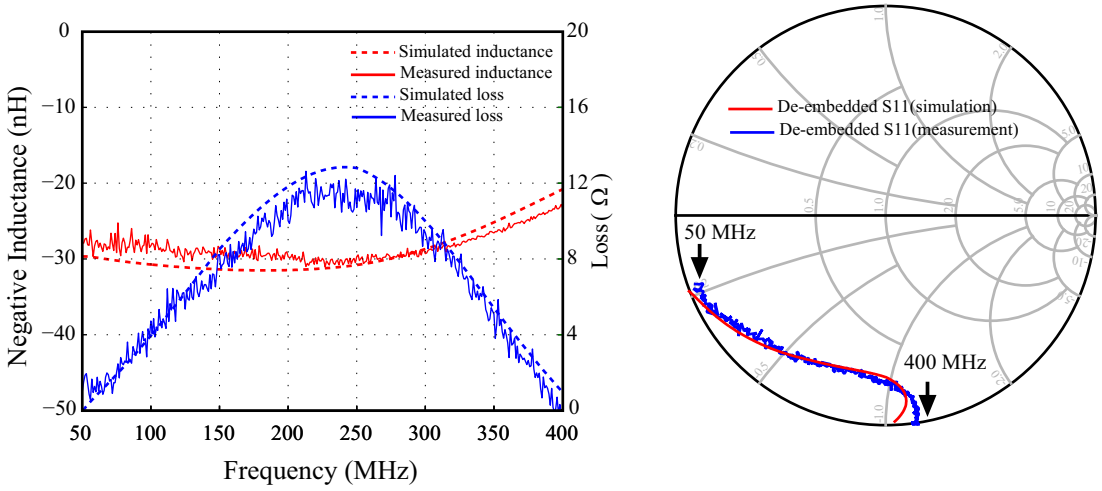

(a) (b)

Figure 2.4. (a) Simulated and measured negative inductance and loss. (b) De-embedded S_{11} from simulation and measurement

de-embedding the swamping inductance. The de-embedded S_{11} can be seen to move counter-clockwise at the edge of the Smith Chart (indicating low loss).

2.2.2 Tunable Negative Inductor

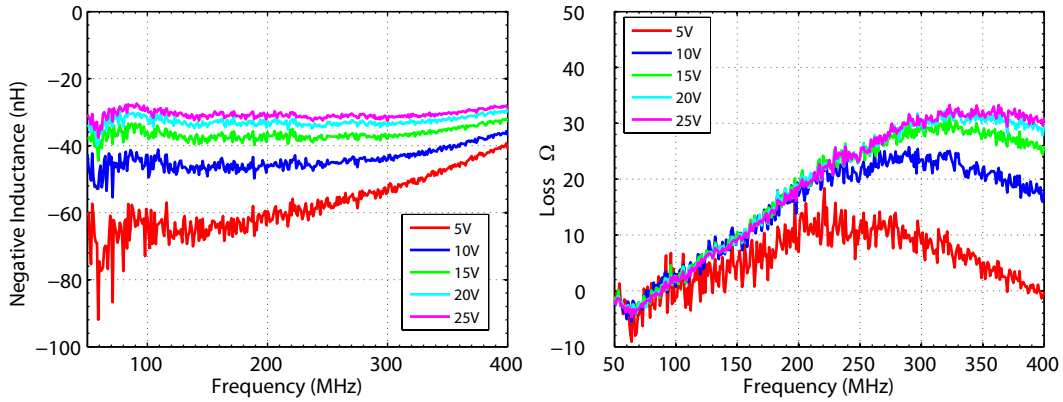

(a) (b)

Figure 2.5. Measured results showing (a) negative inductance and (b) loss of a tunable negative inductor with an inverted varactor

A tunable negative inductor can be obtained by replacing the capacitor *C_load*

with a varactor. Preliminary measurements with a varactor generated results shown in Fig. 2.5. The loss however, varies with the tuning voltage as well, becoming considerably high at high tuning voltages. Therefore, a tunable non-Foster impedance must not only take into account the reactance, but must also have a tunable loss compensation technique. A tunable low loss negative inductor has since been designed by White et. al, [26] (with a small negative loss resistance) using the IBM 8 HP process as an integrated chip.

2.3 Applications

Negative inductors designed using the above techniques can be effectively used in the following applications.

2.3.1 Broadband Impedance Matching

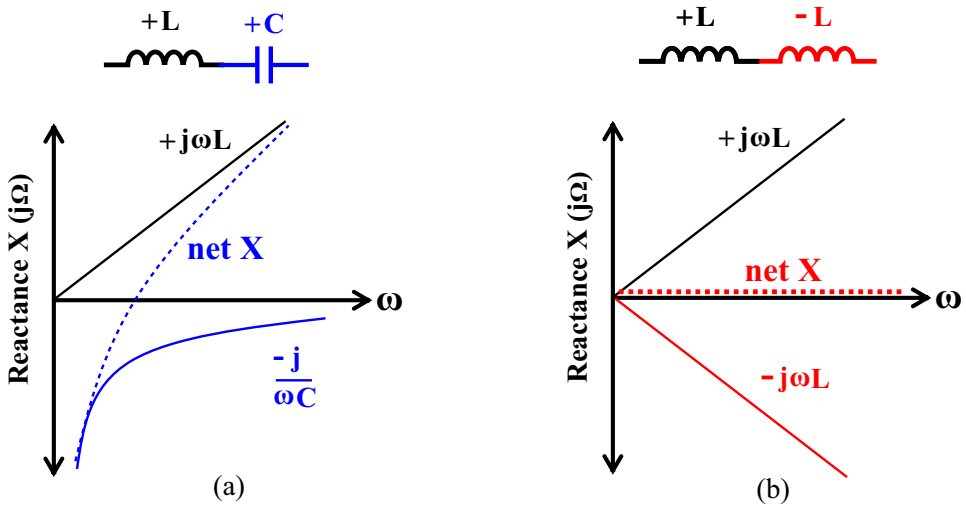

Figure 2.6. (a) Conventional reactance cancellation of an inductor with a capacitor. (b) Non-Foster reactance cancellation of an inductor with a 'negative' inductor

As previously mentioned, conventional passive matching techniques have limitations in the maximum achievable matching bandwidth set by the Bode-Fano limit

[10, 9, 27]. Consider a positive inductor matched with a capacitor in Fig. 2.6(a). It can be seen that the reactance of the inductor is perfectly cancelled by the reactance of the capacitor at only one specific frequency, resulting in a non-zero net reactance at all the other frequencies. A multi-tuned passive matching network will be able to cancel the reactance at many different frequencies, but will never be able to achieve infinite matching bandwidth. On the other hand, if one could attach a negative inductor in series with the positive inductor as shown in Fig. 2.6(b), with both having the same inductance magnitude, then a perfect reactance cancellation could be achieved across infinite bandwidth. In fact, it will be shown later that non-Foster circuits can not only cancel reactance, but can also transform resistance to any required value with specifically designed non-Foster matching networks.

This technique of impedance matching with non-Foster elements is especially useful for small antennas, which have a large reactance arising from their intrinsically high Q, leading to a much lower bound on the maximum bandwidth that can be achieved with passive matching (1.3). Further, small antennas have a radiation resistance that is very small, in addition to being frequency dependent. Chapter 4 will present non-Foster matching techniques which can remove the frequency dependence of radiation resistances, in addition to transforming them to the required resistance value.

2.3.2 Cancellation of Phase Dispersion

Delay-induced phase dispersion can cause a reduction in instantaneous bandwidth in applications where an electric field propagates through a physical distance. If one could imagine a 'negative distance', such dispersion effects could be effectively cancelled. It can be shown that the negative inductor could be approximated as a negative delay line.

A shorted delay line that is less than a quarter wavelength is equivalent to an

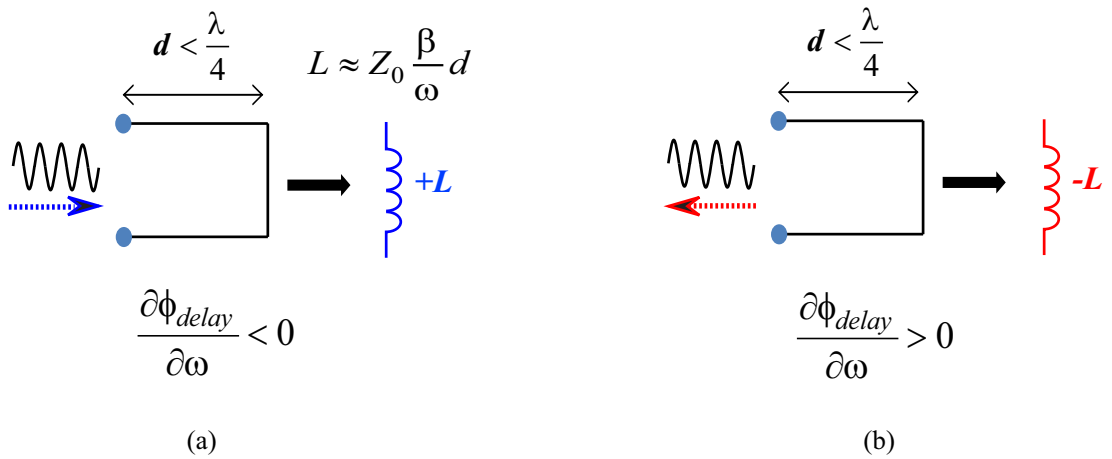

Figure 2.7. (a) Positive delay associated with reflection from a positive inductor. (b) Negative delay associated with reflection from a negative inductor

inductor.

$$L = \frac{Z_0}{\omega} tan(\beta d) \tag{2.1}$$

Here Z_o is the characteristic impedance of the line, ω is the frequency, β is the propagation constant and d is the length of the delay line. For very short delay lines, the above equation can be approximated as

$$L \approx Z_0 \frac{\beta}{\omega} d \tag{2.2}$$

Thus a short delay line is proportional to an inductance. In a similar fashion, a short negative delay line would be proportional to a negative inductance. This can also be understood by observing the counter-clockwise direction of a non-Foster inductor on a Smith Chart, which implies that the reflection phase from a non-Foster element has a positive derivative with respect to frequency. On the other hand, Foster reflection phases have a negative derivative with respect to frequency. Thus by choosing the right non-Foster impedance, we can cancel delay-induced phase dispersion. This will be

the premise of the next chapter, which details a non-Foster loaded parasitic array to eliminate phase dispersion and generate squint-free patterns.

2.4 Summary

The circuit topology for the Negative Impedance Convertor has been described and two design examples have been shown for a negative inductor circuit. Two applications of negative inductors have also been presented, which will be expanded further in the following two chapters.

Chapter 3

Non-Foster Loaded Parasitic Array for Broadband Steerable Patterns

Advancements [28] in mobile communications have led to a need for broadband, low cost, light weight antenna array systems with electronically steerable beams and nulls. Phased array antennas with true time delay beamforming can provide broadband (squint-free) beam or null steering, but at the cost of a complex feed network and complicated RF signal processing circuitry [29]. On the other hand, steerable parasitic arrays such as Electronically Steerable Parasitic Array Radiator (ESPAR) antennas involve only a single fed element along with one or more parasitic elements attached to tunable impedances, and can provide low cost beam or null steering [30, 31, 32]. However, parasitic arrays have a limited instantaneous squint-free bandwidth, typically 10-15%.

In parasitic arrays, the radiated field from the driven element couples to the parasitic elements, gets reflected from the attached load impedances, and is re-radiated back into free space where it adds to the direct radiation from the driven element to form a beam or null pattern [33]. The phase delays incurred over the coupling, reflection and re-radiation process is frequency dependent, leading to a beam or null squint effect beyond a small bandwidth of operation. The dispersive phase delay associated with propagation through physical distances or reflection from Foster impedances (passive components

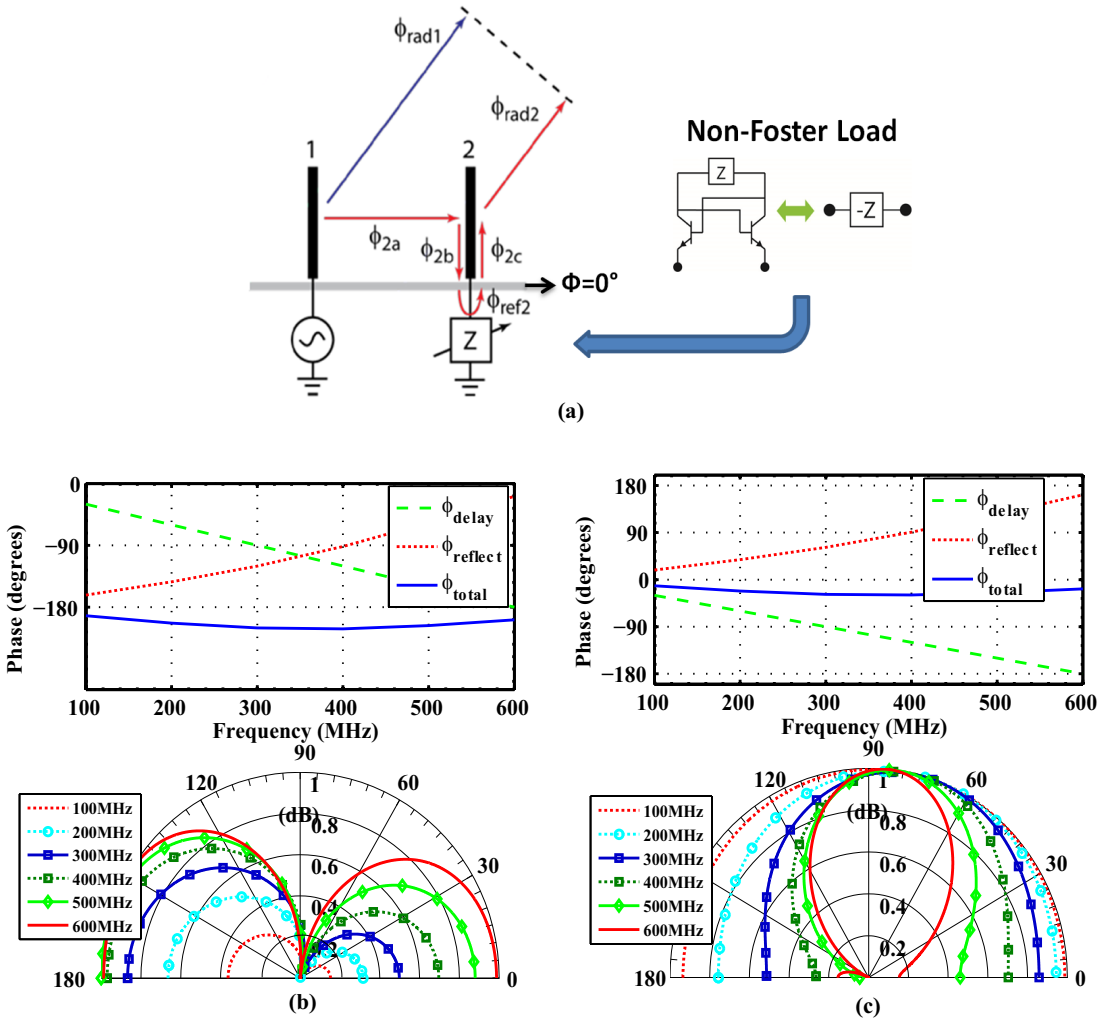

Figure 3.1. (a) A two element non-Foster loaded parasitic array model used to calculate the total phase dispersion due to propagation and reflection. (b) Cancellation of the delay phase with the reflection phase from a $-L\,||\,-C$ load to obtain a net phase of 180° at $\phi = 90^\circ$ and a resultant broadband null from 100-600 MHz. (c) Cancellation of the delay phase with the reflection phase from a series $-L-C$ load to obtain a net phase of 0° at $\phi = 90^\circ$ and a resultant broadband beam from 100-600 MHz.

of $+L$ and/or $+C$) has a negative slope with frequency. To cancel this inherent phase dispersion and achieve broadband performance, we require a dispersive element that has an equivalent positive phase dispersion slope. This can be obtained with negative delay elements or alternatively, with non-Foster impedances.

Non-Foster impedances are components such as negative inductors and/or negative capacitors whose reactance has a negative slope with frequency [11]. They are realized using active, transistor based Negative Impedance Convertor (NIC) or Negative Impedance Inverter (NII) circuits [17, 12]. We have reported different applications of these circuits, as active matching networks to overcome the bandwidth limitations of small antennas [28], and in superluminal waveguides for broadband leaky-wave antennas [15, 34]. Further, the negative slope of the reactance of non-Foster impedances translates to a positive slope in their reflection phase, which can be estimated as an equivalent negative delay. In this paper, we utilize the negative delay characteristics of non-Foster elements to broaden the bandwidth of parasitic arrays by attaching non-Foster loads (active components of $-L$ and/or $-C$) at the parasitic elements to provide a positive-slope reflection phase that cancels the negative-slope propagation phase to eliminate phase dispersion. We can also achieve beam or null steering by tuning the non-Foster load impedances to provide the required phase for a null or beam in a particular direction.

This paper introduces basic array theory for a two element parasitic array to identify the non-Foster circuit required for broadband beams or nulls. For a small array, the beam will be very broad, but the null will be much narrower. It is much easier to see and quantitatively define the null position (a sharp dip) than the beam position. For this array, the 'squint-free bandwidth' or equivalently, the 'null bandwidth' is the bandwidth within which all frequencies have the same squint-free null angle. A two element parasitic array is designed for the operation frequencies appropriate for discrete device NICs, and array theory is used to calculate non-Foster impedances required for broadband nulls at different azimuth angles. EM/circuit co-simulation has been used to calculate radiation patterns for different non-Foster parasitic loads and these have been compared with those of passive parasitic loads to show that non-Foster parasitic loads achieve broader squint-free bandwidths for almost all azimuth angles. Stability conditions are analyzed

for NICs attached to parasitic antennas, and a stable NIC is fabricated and attached to the parasitic antenna. Measurements for a broadband, broadside null have been performed and compared to co-simulation patterns, demonstrating an almost 2:1 instantaneous null bandwidth. This can be compared to one of the broadest reported bandwidths for a conventional parasitic array [35] which contains 24 parasitic elements that are switched on or off to produce two separate partially overlapping beam steering modes achieving a total simulated 2:1 gain bandwidth. However, the instantaneous bandwidth during a single mode of operation is less than 2:1. In contrast, the non-Foster parasitic array has a measured instantaneous 2:1 bandwidth with just one parasitic element. However, the tunability of this particular non-Foster array is limited by the stability constraints of the NIC. Design considerations to improve stability of the non-Foster parasitic array over a broad tuning range have been presented.

3.1 Parasitic Array Design and Fabrication

A simple two element parasitic array loaded with a non-Foster impedance has been modeled as shown in Fig. 3.1. The elements are assumed to be infinitesimally small with a 25 cm separation between them. The array factor patterns for two non-Foster loads, namely a parallel $-L\,||{-}C$ impedance of $-12\text{nH}\,||-5\text{pF}$ and a series $-L{-}C$ impedance of $-12\text{nH}\,-5\text{pF}$ have been shown in Fig. 3.1(b) and Fig. 3.1(c) respectively. The coupling phase or delay phase delay from the driven element to the parasitic element has a negative slope with frequency (as seen in the phase plots of Fig. 3.1(b) and Fig. 3.1(c)). The reflection phase $\phi_{reflect}$ from the non-Foster load will have a positive slope with frequency (as seen in the phase plots of Fig. 3.1(b) and Fig. 3.1(c)). The array factor patterns are obtained after adding the propagation delay phase and the reflection phase from the attached load. We see that when the non-Foster load is a parallel $-L\,||{-}C$ impedance of $-12\text{nH}\,||-5\text{pF}$, the reflection phase from it cancels

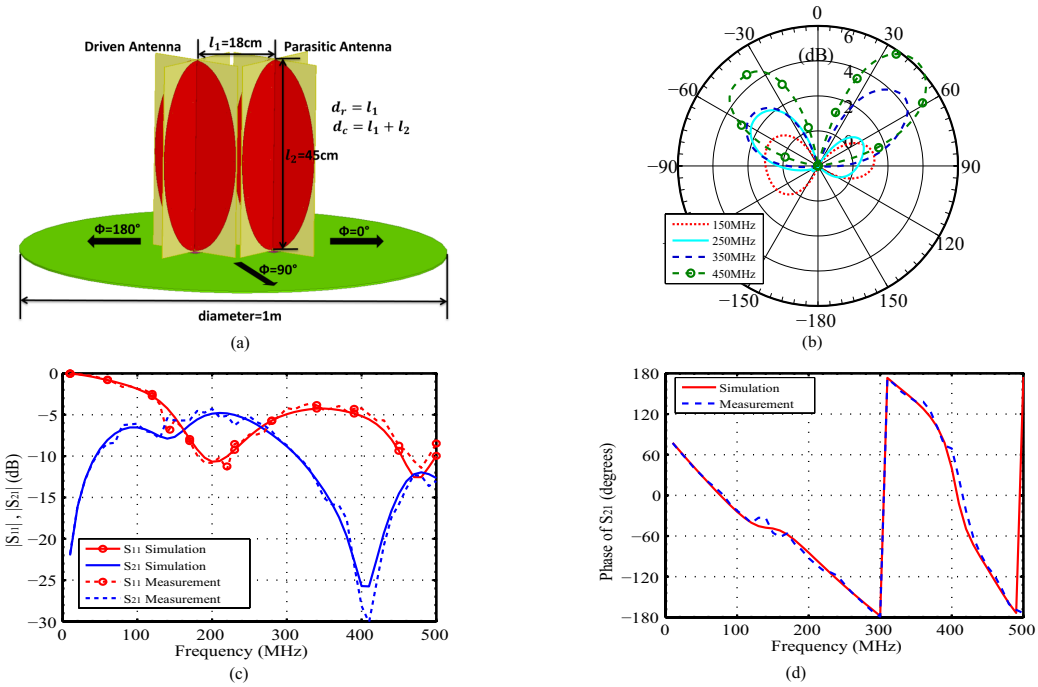

Figure 3.2. (a) Simulated two element array. (b) Simulated elevation patterns of a single antenna. (c) Simulated and measured $|S_{11}|$ (dB) and $|S_{21}|$ (dB). (d) Simulated and measured phase of $|S_{21}|$.

the delay induced phase dispersion to provide a net phase ϕ_{total} of around -180° from 100-600 MHz at $\phi = 90^\circ$ along the azimuth, leading to a broadband null (Fig. 3.1(b)). When the non-Foster load is a series $-L-C$ impedance of -12nH -5pF, the reflection phase from it cancels the delay induced phase dispersion to provide a net phase ϕ_{total} of around 0° from 100-600MHz at $\phi = 90^\circ$, leading to a broadband beam (Fig. 3.1(c)). This simplified model provides the same squint-free patterns across a 6:1 bandwidth. However in reality, the matching and coupling characteristics of the antennas, unwanted scattering effects, non-uniform radiation patterns and non-ideal non-Foster loads reduce the achievable bandwidth.

In a parasitic array, the driven antenna should be well matched to accept incoming signals and should also have a high enough gain to be able to radiate to the parasitic elements. The distance between the driven element and the parasitic elements should be

optimized to have sufficient coupling between them while reducing unwanted scattering. The design of the antennas should also take into consideration the practical performance limits of NICs. Since discrete device NICs can only generate broadband, high quality factor non-Foster impedances for frequencies less than 400 MHz, a prototype of a two element parasitic array was designed for those frequencies. At those low frequencies, an antenna array that could achieve good matching and coupling with uniform patterns across a broad bandwidth was difficult to design due to the following tradeoffs: large antennas are needed for broadband match; however, large antennas have non-uniform patterns within the required range of frequencies. Small antennas provide uniform patterns, reduced spacing and less unwanted scattering, but do not have the required matching or gain. It will also be shown later that the parasitic antennas impedance should satisfy the stability conditions of the NIC.

Optimized simulations in Ansoft HFSS yielded a bulb-shaped monopole array design that provided the required matching and coupling characteristics across the broadest possible bandwidth (150 MHz-350 MHz) with uniform patterns in those frequencies. The monopole had a height of 45 cm, width of 24 cm, and the distance between the driven and parasitic element was 18 cm. The antennas were mounted on a circular aluminum ground plane of diameter 1m (Fig. 3.2(a)). The elevation patterns of a single bulb-monopole antenna mounted on the ground plane are simulated and shown in Fig. 3.2(b). Due to the finite ground plane, we see that the angle of maximum radiation is not horizontal for high frequencies. This can be corrected using a ground plane with a conducting sleeve as described in [36]. The elevated main beams at frequencies above 350 MHz limit the highest frequency that can be observed in the squint-free null bandwidths, as can be seen in the next section. The azimuth patterns of a single bulb-monopole antenna are omnidirectional for these frequencies. The parasitic array design was fabricated and tested and found to agree well with simulations. The sim-

ulated and measured matching (S_{11}) and coupling (S_{21}) characteristics of the passive array are shown in Fig. 3.2(c) and Fig. 3.2(d). Ideally, S_{11} should be as small as possible, indicating a good impedance match, and S_{21} should be close to 1, indicating good coupling between the two antennas. But due to the tradeoffs mentioned before, a good match and high coupling could not be achieved across the entire bandwidth. However, the measured pattern results of the non-Foster array follow the theoretical array theory (that assumes ideal S_{21}) sufficiently well to indicate that the performance of the two element array falls within acceptable limits.

3.2 Non-Foster Parasitic Arrays - Theory and Bandwidth Improvement

3.2.1 Array Theory to Identify Non-Foster Impedances for Null/Beam Tuning

The fabricated 2 element antenna array can be modeled using the schematic shown in Fig. 1(a), where antenna 1 is the driven element and antenna 2 is the parasitic element. The array factor can then be derived as

$$AF = 1 + |S_{21}| \times e^{j(\phi_{coupling}+\phi_{reflection}+\phi_{radiation})}, \tag{3.1}$$

where,

$$\phi_{coupling} = \phi_{2a} + \phi_{2b} + \phi_{2c} = \frac{\pi}{2} - k \times d_c = \angle S_{21} \tag{3.2}$$

$$\phi_{radiation} = \phi_{rad2} = k \times d_r \times cos(\phi) \tag{3.3}$$

$$\phi_{reflection} = \phi_{ref2} \tag{3.4}$$

Here, $\phi_{coupling}$ is the coupling phase from antenna 1 to antenna 2, and is the total sum of the propagation phase ϕ_{2a} along the distance of separation, along with the propaga-

tion phase ϕ_{2b}+ϕ_{2c} through the parasitic antenna (Fig. 3.1(a)). The coupling phase is equivalent to $\frac{\pi}{2} - k \times d_c$ where the added phase of $\frac{\pi}{2}$ is due to the capacitive coupling of the monopole array. The variable k is the wavenumber, and d_c is the coupling distance which equals the distance of separation plus the antenna height. The term $\phi_{radiation}$ is the radiation phase which denotes the difference in the far-field radiated phase between the driven element and the parasitic element for an azimuth angle ϕ where ϕ has the values denoted in Fig. 3.2(a). It is equivalent to $kd_r cos(\phi)$, where d_r is equal to the distance of separation. The term $\phi_{reflection}$ is the reflection phase ϕ_{ref2} from the load attached to the parasitic antenna.

For easier analysis, we assume that the coupling loss $|S_{21}|$ is negligible. In order to get broadband nulls along an azimuth angle ϕ, the sum of the coupling phase, reflection phase and radiation phase should equal π radians. This means that the reflection phase should be

$$\phi_{reflection} = \pi - \phi_{coupling} - \phi_{radiation}, \tag{3.5}$$

which implies,

$$\phi_{reflection} = \pi - \frac{\pi}{2} + k \times d_c - k \times d_r \times cos(\phi). \tag{3.6}$$

In other words,

$$\phi_{reflection} = \pi - \angle S_{21} - k \times d_r \times cos(\phi). \tag{3.7}$$

From 3.6, we observe that in order to achieve 180° of total phase across a broad bandwidth, the reflection phase will need to have a positive slope with frequency (since d_c will always be greater than d_r). This reflection phase can be obtained with non-Foster impedances ($-L$,$-C$).

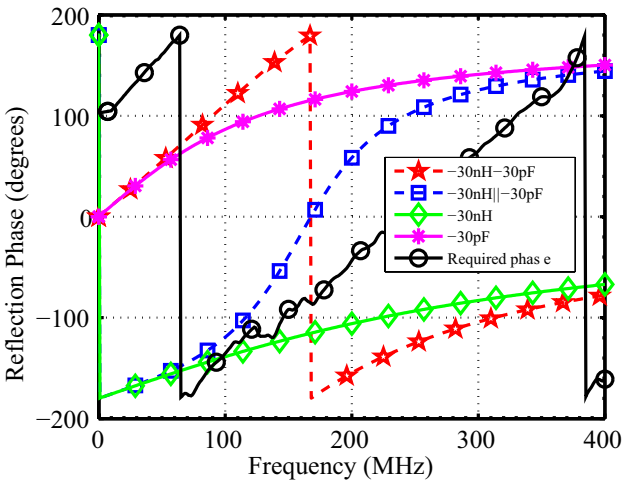

Figure 3.3. Required non-Foster reflection phase for getting a squint-free null along 180° for the fabricated array, and the reflection phase of ideal $-L$, $-C$ components.

3.2.2 Tunable Nulls with Ideal $-L||-C$

The measured S_{21} data of the parasitic array is used to calculate the required non-Foster reflection phase. To identify the $-L$,$-C$ combination needed for providing the required phase, we first calculate the reflection phase needed to produce a null along say, $\phi = 180^\circ$ (in the direction away from the parasitic antenna) using 3.7. This phase has a positive slope as can be seen from Fig. 3.3. When we simulate the reflection phases of $-L$, $-C$, series $-L-C$ and parallel $-L\,||-C$, we see that a parallel $-L\,||-C$ can give us the required reflection phase in the entire operation region of the parasitic array (150-350 MHz), as seen in Fig. 3.3. The reflection phase of the series $-L-C$ can also approximate the required phase, but only for a limited low frequency region. By choosing the correct value of $-L$ and $-C$, we can dictate the slope and resonance frequency of the reflection phase. Even if the phase of S_{21} is not exactly linear with respect to frequency, we can tune the values of $-L$ and $-C$ to get the required phase slope.

Fig. 3.4 shows the reflection phase required for squint-free nulls along the angles

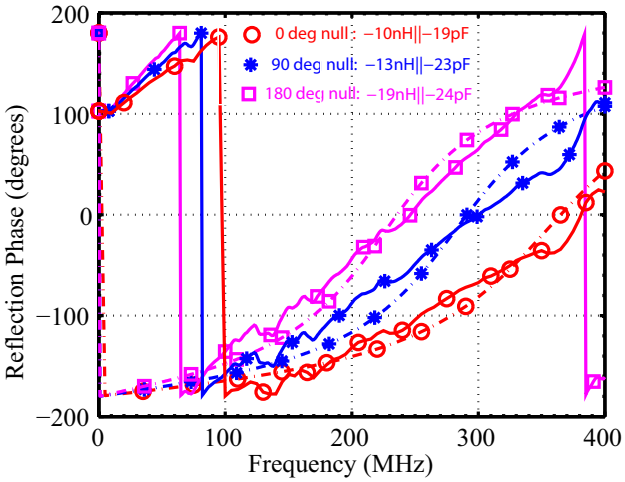

Figure 3.4. Required non-Foster reflection phase calculated using array theory for a broadband null at 0°, 90° and 180° (solid lines). Reflection phase of $-L$ $||-C$ impedances (dotted lines) that approximate the theoretical phase curves.

of $\phi = 0°$, $\phi = 90°$ and $\phi = 180°$, calculated using 3.7. The directions of these angles with respect to the driven and parasitic antennas are shown in Fig. 3.2(a). As the null angle increases, the reflection phase slope becomes steeper. With non-Foster impedances of $-L$ $||-C$, we can achieve good approximations of the theoretical reflection phase curves. The $-L$, $-C$ values required for each of the 3 null directions are also given in Fig. 3.4.

Using Ansoft HFSS and Ansoft Designer, we were able to dynamically link the parasitic array EM model to a circuit model of $-L$ $||-C$ to get radiation patterns for different values of $-L$ and $-C$ in the region of operation of the parasitic array (150-350 MHz). The azimuth patterns obtained from co-simulations are shown in Fig. 3.5. For the 0° null case (Fig. 3.5(a)), we obtained broadband nulls when the parasitic antenna was shorted (-1 nH load), similar to the case of a reflector antenna. For the 90° null (Fig. 3.5(b)) and 180° null (Fig. 3.5(c)), the values of $-L$ and $-C$ obtained from Fig. 3.4 had to be modified slightly in order to broaden the bandwidth. This might be due to scattering effects that were unaccounted for in the simple mathematical phase

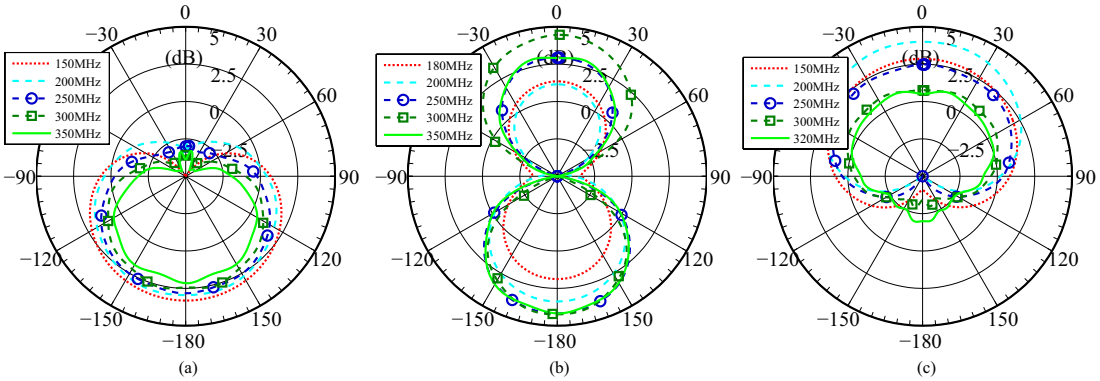

Figure 3.5. Broadband nulls obtained from ideal $-L$,$-C$ co-simulations with antenna array. (a) Null at 0° obtained with -1nH. (b) Null at 90° obtained with -15nH $||-23$pF. (c) Null at 180° obtained with -19nH $||-30$pF.

calculation. The lowest and highest frequencies providing squint free nulls are shown for each of the 3 null directions, along with some intermediate frequencies. From these, we see that we can achieve the broadest bandwidth for the 0° null. As the null angle increases, the bandwidth decreases. However, null tuning can be achieved across all azimuth angles, with broader bandwidths than those obtained with traditional Foster parasitic arrays.

3.2.3 Squint-Free Bandwidth Improvement

We will verify the improvement in squint-free bandwidth by studying the maximum achievable bandwidth with both Foster and non-Foster loads for different null angles. Simulations were done using the designed two element bulb-monopole array and various Foster loads ($+L$, $+C$ combinations) and non-Foster loads ($-L$, $-C$ combinations). The parasitic loads that gave the broadest squint-free bandwidth for nulls at 0°, 45°, 90°, 135° and 180° are shown in Table 3.1. While assessing the bandwidth for each null angle, we allowed a $\pm 20^\circ$ variation around the null angle considered for both the Foster and non-Foster cases. We also optimized for parasitic loads that resulted in patterns where the null gain was at least 3 dB lower than the beam gain for all frequen-

cies in the squint-free bandwidth. In general, it is more difficult to obtain squint-free nulls than it is to obtain squint-free beams, due to the formation of small backlobes or sidelobes that could change the null position, while the beam position remains the same. The results are summarized in Fig. 3.6.

Table 3.1. Squint-free null frequencies for non-Foster and Foster parasitic loads

Null Position	Non-Foster Load and the Squint-Free Frequencies	Foster Load and the Squint-Free Frequencies
0°	Short : 150-350 MHz	Short : 150-350 MHz
45°	-13nH $\|\|$ -17pF: 170-350 MHz	31pF : 190-350 MHz
90°	-15nH $\|\|$ -23pF: 180-350 MHz	30nH $+5$pF : 220-300 MHz
135°	-16nH $\|\|$ -28pF: 180-330 MHz	10nH $+6.5$pF : 210-200 MHz
180°	-19nH $\|\|$ -30pF: 150-320 MHz	Open : 170-220 MHz

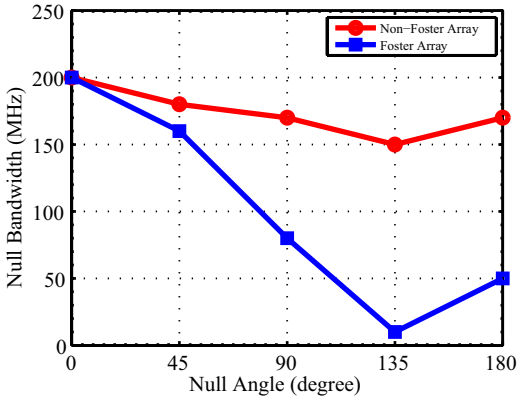

Figure 3.6. Bandwidth of squint-free nulls for different null positions obtained with the non-Foster and Foster parasitic loads in Table 3.1.

We see that for the 0° null angle, the parasitic element acts like a reflector and so we can achieve the broadest possible bandwidth with a short. As the null is tuned away from the parasitic element, the maximum achievable bandwidth decreases for both Foster and non-Foster loads. Nevertheless, we see that non-Foster elements can provide a larger bandwidth of squint-free nulls compared to Foster elements for almost all azimuth angles.

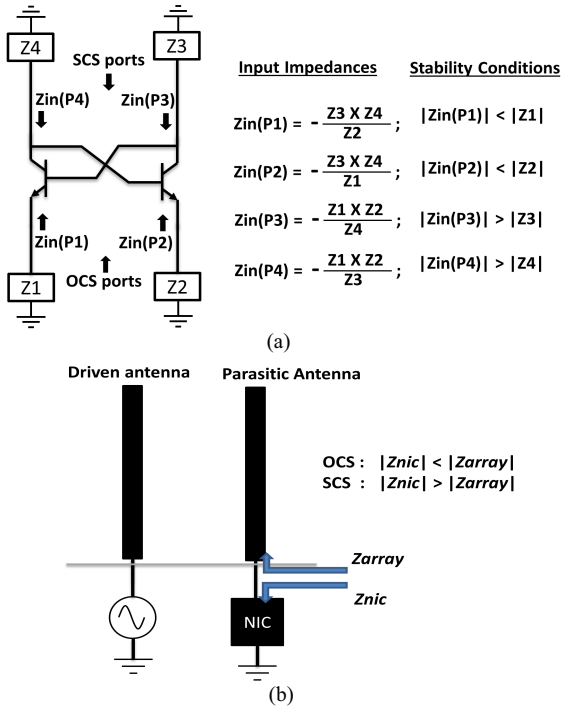

Figure 3.7. (a) General topology of a Negative Impedance Convertor (NIC) circuit and the input impedances seen into each of the four ports. (b) OCS and SCS stability conditions of the NIC attached to the parasitic antenna.

The non-Foster impedances in Table 3.1 can be achieved using discrete device NICs for the operation frequencies of the designed parasitic array. However, the stability constraints of NICs pose a considerable challenge, as shown in the next section.

3.3 NIC Design and Stability Considerations

Non-Foster impedances can be implemented using Negative Impedance Convertor (NIC) circuits or Negative Impedance Invertor (NII) circuits [17, 18]. These circuits have a general cross coupled transistor topology (Fig. 3.7(a)). The input impedance seen at each of the 4 ports, and the conditions for stability at each of those ports are also shown in Fig. 3.7(a). A primary challenge in the design of NICs is to maintain stability while generating broadband, low loss non-Foster reactances. A number of theories have

been suggested to analyze the stability constraints of NICs [21, 37, 22, 23].

3.3.1 Stability Analysis

In general, if Z_{nic} is the required input impedance of the NIC and Z_{load} is the load impedance to be attached at the input, the two stable conditions of the NIC are as follows:

(1) If $|Z_{load}| > |Z_{nic}|$, then the NIC should be implemented in its open circuit stable (OCS) configuration with its input at the transistor's emitter.

(2) If $|Z_{load}| < |Z_{nic}|$, then the NIC should be implemented in its short circuit stable (SCS) configuration with its input at the transistor's base/collector.

Fig. 3.7(b) shows the stability criteria for our two element parasitic array with an NIC attached to the parasitic antenna. Z_{array} is the impedance seen by the NIC looking into the parasitic antenna and Z_{nic} is the input impedance of the NIC. Fig. 3.8 displays the magnitude of Z_{array}, along with the magnitude of the NIC impedance Z_{nic} for the different $-L$,$-C$ values taken from Fig. 3.5 for different null angles.

For the 0° null angle using a -1nH load, $|Z_{nic}|$ is always less than $|Z_{array}|$ and so the NIC will be stable in its OCS configuration (Fig. 3.8(a)).

For the 90° null angle using a -15nH $||-23$pF load, $|Z_{nic}|$ is less than $|Z_{array}|$ up to 260 MHz (OCS condition), and $|Z_{nic}|$ is greater than $|Z_{array}|$ above 260 MHz (SCS condition). This means that the NIC has to have the OCS configuration to be stable under 260 MHz, while simultaneously requiring the SCS configuration to be stable above 260 MHz (Fig. 3.8(b)).

For the 180° null angle using a -19nH $||-30$pF load, the NIC has to have the OCS configuration up to 120 MHz, SCS configuration from 120 MHz-240 MHz, and OCS configuration again from 240 MHz-400 MHz (Fig. 3.8(c)).

This implies that for the NIC to be stable across the entire bandwidth of oper-

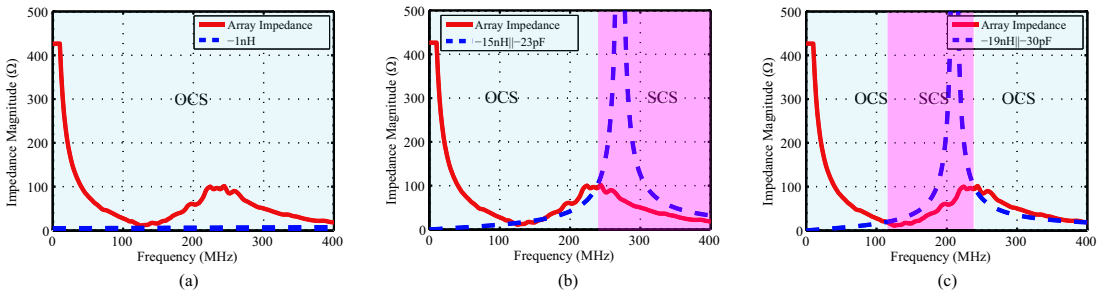

Figure 3.8. Required stability conditions of the non-Foster impedances when loaded to the antenna array for the (a) 0° null using -1nH, (b) 90° null using -15nH $||-23$pF, and (c) 180° null using -19nH $||-30$pF.

ation, the NIC impedance should be either completely above or completely below the antenna array impedance for all frequencies of interest. For the monopole array considered here with a parallel $-L\,||{-}C$, the NIC has to have the OCS configuration for low frequency stability (since $-L\,||{-}C$ is a short at low frequencies while the monopole is an open at low frequencies). Further, in order to maintain OCS stability across the entire bandwidth of operation, we have to reduce the quality factor Q of the NIC impedance so that its peak impedance during its resonance is less than the antenna impedance at that frequency. This means that we will have to sacrifice the nullforming performance of the parasitic array. Even with those conditions, it is still not possible to achieve the 180° null angle with the NIC since the Q of the NIC would have to be far too low in order to satisfy OCS stability conditions around 100 MHz. Therefore, we see that the tunability and nullforming capabilities of the parasitic array are restricted by the stability conditions of the non-Foster impedance.

3.3.2 Circuit Design and Fabrication

From the stability analysis, we know that the NIC circuit has to have an OCS configuration, with its input at one of the transistor emitters. Since we require a parallel $-L\,||{-}C$ impedance, we can either use a Negative Impedance Convertor (NIC)

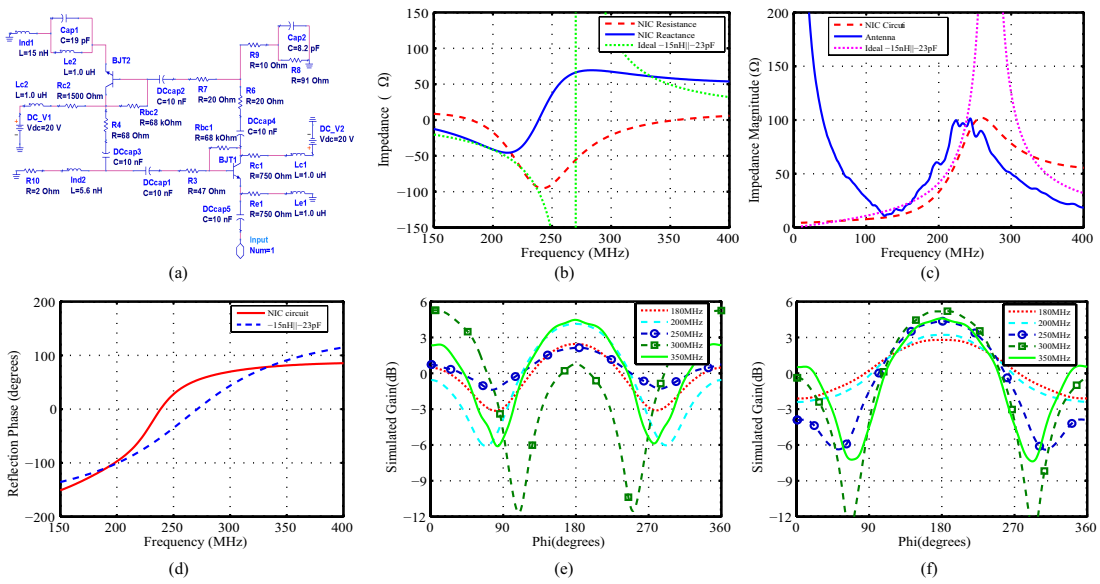

Figure 3.9. (a) NII circuit design for getting a 90° null and (b) the simulated real and imaginary non-Foster impedance of the circuit compared to the ideal impedance required. (c) The reduced quality factor of the circuit impedance to achieve stability with the antenna impedance. (d) Reflection phase of the NII circuit compared to the ideal required reflection phase. (e) Radiation patterns obtained from co-simulations with the NII circuit and array. (f) Radiation patterns obtained from co-simulations after changing the NII circuit impedance.

configuration to negate the impedance of a positive parallel $+L\,||{+}C$, or we can use a Negative Impedance Invertor (NII) configuration to negate the admittance of a positive series $+L{+}C$. We chose to use the NII configuration, since it would help us transition into a tunable circuit (using a tunable varactor in the NII circuit will give us a tunable $-L$ impedance) [26].

The NIC circuit for the 0° null angle is trivial since we can get the same result with a short circuit. The NIC circuit for the 180° null angle has too many stability constraints with this particular antenna impedance for it to be physically realizable. Therefore we chose to implement the circuit needed for a 90° null angle (NIC impedance of $-15\text{nH}\,||-23\text{pF}$). In order for the NIC to be OCS stable with the antenna, we will have to reduce the NICs quality factor Q, and slightly push the resonance of the NIC to lower

frequencies so that the NICs peak impedance is not much higher than the antennas peak impedance.

Fig. 3.9(a) shows the schematic of an NII circuit that gives us an impedance equivalent to $-L\,||{-}C$. The impedance of the NII circuit seen looking into the emitter of BJT1 is inversely proportional to the emitter load of BJT2 and directly proportional to the loads at the two base-collector junctions as shown in the schematic of Fig. 3.7(a). Since the emitter load of BJT2 is a series LC impedance of Ind1 and Cap1, the impedance of the NII will take the form of a parallel $-L\,||{-}C$ impedance as required. The loads at the two base-collector junctions, namely R9+(Cap2||R8) and R10+Ind2 have been chosen to optimize the quality factor Q of the circuit. Resistors R3, R4, R6 and R7 have been used to stabilize the circuit. The circuit layout was simulated in Ansoft HFSS and the device models were attached and optimized in Agilent ADS to provide a high enough Q for the circuit that it would produce broadband 90° null patterns, yet a low enough Q that it would be stable with the antenna. The resistance and reactance of the simulated NII (taking into account all the component and layout parasitics) is shown in Fig. 3.9(b).

Fig. 3.9(c) shows the simulated impedance magnitude of the stable NII circuit along with the antenna impedance and the ideal $-L\,||{-}C$ impedance. The circuit was tuned to the edge of stability where the circuit impedance magnitude has just crossed over the antenna impedance magnitude, as seen in Fig. 3.9(c). We see that the Q has been reduced and that the resonance has been slightly pushed to lower frequencies. Even though the NII impedance is still greater than the antenna impedance at higher frequencies, the gain of the NII is sufficiently less at those frequencies to prevent instability. However, this is the edge of stability and a slight shift of the resonance to higher frequencies causes instability.

In Fig. 3.9(d), the input reflection phase of the NII has been compared to the

ideal required reflection phase from -15nH $||-23$pF. The greatest variation in phase from the ideal case is observed around 250 MHz, which corresponds to the resonant frequency of the NII (Fig. 3.9(b)). The impedance of the NII has been significantly damped at the resonant frequency to provide stability, leading to a phase variation around that frequency.

Fig. 3.9(e) shows the patterns obtained by dynamically linking the simulated circuit with the EM model of the antenna. Although the null angle is not as uniform as for the ideal $-L||-C$ case, it is still an improvement over the bandwidth and nullforming performance obtained from Foster loads. A broadband squint-free 90° null was obtained from 180-350 MHz.

To obtain steerable squint-free beams or nulls, we need tunable $-L$ impedances and $-C$ impedances. These can be obtained with a tunable negative capacitor with an NIC and a varactor, and a tunable negative inductor with an NII and a varactor. With integrated circuit technology, we can design tunable NICs or NIIs that can provide high quality factor non-Foster impedances in the UHF frequencies [26]. It is also feasible to switch between fixed $-L$,$-C$ impedances based on the beam/null angle required. In the NII schematic of Fig. 3.9(a), the main components affecting the impedance of the circuit are the inductor Ind1 and capacitor Cap1 at the emitter of BJT2. The capacitor Cap1 can be replaced by a varactor to enable tunability, resulting in a tunable $-L$ at the input. The inductor Ind1 cannot be tuned in this NII configuration, so the $-C$ value of this NII circuit cannot be tuned. We will get the best possible beam/null steering capabilities with two separate circuits for a negative inductor and negative capacitor, so that either can be individually tuned to provide the required reflection phase for any beam/null direction. With only a tunable varactor in place of the capacitor Cap1 in the NII circuit, we can only achieve certain null positions. When Cap1 is changed from 19pF to 10pF, we see from the co-simulation patterns that the null position moves from

90° to about 60° (Fig. 3.9(f)).

Due to the one port configuration of the NII, and the fact that it is stable only when attached to the antenna (equivalent to some RLC impedance), we could not get a de-embedded measurement of the NII. However, our simulation techniques have proven to be very reliable with other NIC designs and measurements [38, 34] and so we proceeded to pattern measurements with the parasitic array.

3.4 Squint-Free Pattern Measurements

The NII was fabricated and attached to the base of the parasitic antenna. We then supplied the required DC voltage to the NII circuit and attached the driven antenna to a spectrum analyzer so that any instability in the NII would be coupled from the parasitic antenna to the driven antenna and show up as peaks above the noise floor in the spectrum analyzer. We also tested our stability analysis by trying to push the $-L\,||{-}C$ resonance to slightly higher frequencies and found that it did indeed lead to instability. After implementing the stable circuit shown in Fig. 3.10(a), we measured the parasitic array's patterns in an anechoic chamber as shown in Fig. 3.10(b). Although the chamber's dimensions were too small for accurate low frequency gain measurements, we did get sufficiently smooth patterns with null positions that agreed with simulations (Fig. 3.10(c)). The measurements were plotted after normalizing each frequency's pattern separately to its minimum measured gain value to get a null gain relative to beam gain for each frequency. The normalized gain values shown have not been calibrated for the path loss and the gain of the receiving horn antenna, and so the measurements are only indicative of the null positions and not the actual gain. The actual gain can be observed from the co-simulation patterns shown in Fig. 3.10(e). The co-simulation patterns have further been normalized and plotted in Fig. 3.10(d).

We see from the measurement patterns (Fig. 3.10(c)) and the co-simulation pat-

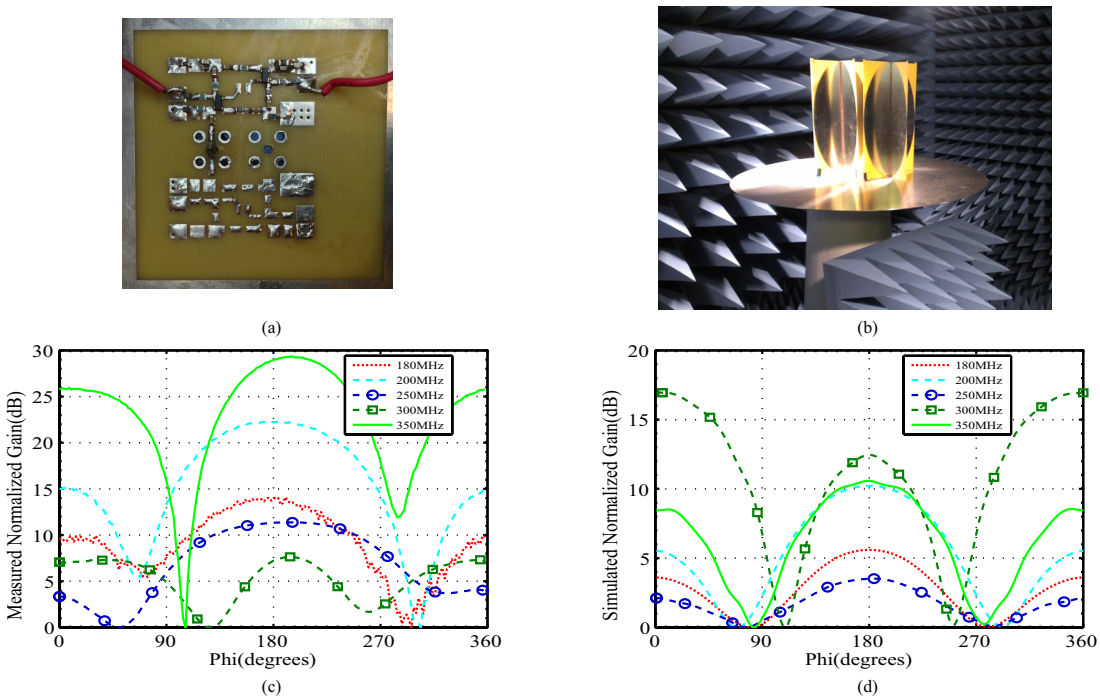

Figure 3.10. (a) Fabricated NII circuit. (b) Measurement setup in an anechoic chamber. (c) Measured normalized gain patterns. (d) Co-simulated normalized gain patterns.

terns (Fig. 3.10(d)), that the null positions for all frequencies from 180-350 MHz have less than a $\pm 30^\circ$ variation about 90° and 270°. The frequencies from 240-310 MHz show the biggest variation from the 90° null position compared to the co-simulation patterns, since that frequency region corresponds to the resonance region of the NII making it very sensitive to component variations in the circuit. Thus we see that the null forming performance of the NII is affected by the $-L\,||-C$ resonance of the NII and the stability constraints requiring the NII to have low Q and a lower resonant frequency. However, these measured results display a squint-free bandwidth that is more than a factor of 2 better than the bandwidth obtained with Foster parasitic loads. This non-Foster parasitic array was designed to demonstrate its squint-free nullforming capability, so gain analysis and optimization has not been done. Further studies can be done to improve the gain using better antenna and array designs. The nullforming capabilities in the resonant re-

gion of the circuit can also be improved using antenna designs that impose less stringent stability requirements on the non-Foster circuit. For a non-Foster parasitic array operating at higher frequencies, accurate gain measurements could be obtained to validate the simulated gain.

3.5 Design Considerations for a Stable, Tunable, Broadband Parasitic Array

It was shown that the tunability of the parasitic array was restricted by the stability constraints of the NIC set by the impedance of the parasitic antenna. We will introduce an alternate approach to design a stable, broadband non-Foster parasitic array with tuning capabilities. First, it is important to choose an NIC that has similar impedance curves as the antenna array to prevent the NIC impedance from crossing over the antenna impedance in the frequencies of interest. This means that for a loop antenna array, we should choose a parallel $-L\,||-C$ (both have a parallel LC impedance magnitude), and for a dipole array, we should choose a series $-L-C$ (both have a series LC impedance magnitude). Then, we have to design the coupling distance dc such that the required non-Foster phase can be obtained with the NIC. For example, assuming we have a dipole array (requiring a series $-L-C$), we have to design the array such that the coupling distance dc (distance of separation+ antenna height) leads to a theoretical non-Foster reflection phase that can be achieved by a series $-L-C$. If the coupling distance dc is too large, then the required non-Foster reflection phase will undergo a second resonance (from -180° to $+180^\circ$), which cannot be achieved by a series $-L-C$.

Once the total coupling distance dc is known, the antenna height or size can be chosen such that it has sufficient gain and matching, and the antenna separation can be chosen to have sufficient coupling. The antenna impedance can further be optimized to provide broadband stable conditions for the NIC. This technique of using non-Foster

circuit loads is especially suited for parasitic arrays with a few antenna elements so that the coupling between the elements is clearly defined and the required non-Foster reflection phase can be easily achieved with an NIC. For elements with more than one parasitic element, the coupling between the elements is defined by a coupling matrix, which can be used in the array factor equation to determine the required non-Foster reflection phase. Alternatively, optimization techniques mentioned in [30] and [39] can be used to find the reactive loads for multiple frequencies in a required broad bandwidth, and the calculated reactances will be found to follow a non-Foster reactance curve versus frequency.

Another important consideration in an active non-Foster circuit is the noise generated by the circuit and the resulting SNR degradation. When the signal coupled to the parasitic element is reflected by the non-Foster circuit attached to the parasitic element, a frequency dependent noise generated by the circuit is added to the existing environmental noise in the signal. The noise performance of non-Foster parasitic arrays is beyond the scope of this paper, but we are currently studying noise characteristics of non-Foster circuits to analyze the possible tradeoffs between bandwidth improvement and SNR degradation.

3.6 Conclusion

A novel technique has been introduced to eliminate beam/null squint arising from phase dispersion in parasitic arrays. Using non-Foster loaded parasitic elements, we can compensate for the propagation delay phase by introducing an equivalent negative delay associated with the reflection phase of non-Foster elements. An additional phase could also be imposed by the non-Foster elements to achieve a beam or null. Further, by tuning the non-Foster impedance, we could tune the angle of the beam/null. We have developed the theory of non-Foster parasitic arrays to show that a non-Foster reflec-

tion phase is required for a frequency-independent beam/null angle, and to identify the non-Foster impedance required for a particular beam/null angle. We have tested this theory with a two element monopole array and ideal $-L$, $-C$ impedances. A non-Foster circuit designed to achieve squint-free null patterns has been fabricated, and measurements of squint-free radiation patterns have been compared with simulation results. Stability constraints of the NIC relating to the antenna impedance have been identified, and an approach to mitigate stability and tunability constraints has been suggested. We have also examined the bandwidth advantage of non-Foster parasitic arrays over Foster parasitic arrays. Our measurement results verify the theoretical analysis, and demonstrate scope for improvements. This prototype could be improved to include tunable $-L$ and $-C$ circuits to obtain reconfigurable squint-free patterns. A further study on the bandwidth-tunability-nullforming tradeoffs could be useful in developing an electronically tunable, broadband, low cost parasitic array without beam/null squint.

Chapter 3 is based on and mostly a reprint of the following paper: M. M. Jacob, J. Long, and D. F. Sievenpiper, Non-Foster Loaded Parasitic Array for Broadband Steerable Patterns, *IEEE Trans. Antennas Propag.*, vol. 62, no. 12, pp. 60816090, 2014.

Chapter 4

Broadband Non-Foster Matching for Small Antennas

A study of small antennas shown in [8] reinforces the bandwidth-efficiency-size constraints of all measured small antennas available in literature. Chapter 1 introduced the theory behind the intrinsically small bandwidth of small antennas, and Chapter 2 presented an approach to match the impedance of small antennas using non-Foster circuits to overcome the bandwidth limitations.

This chapter will present a general non-Foster matching network for a small dipole and a small loop antenna model based on Wheeler's antenna models. Then two design examples will be presented for non-Foster matched small antennas whose bandwidth exceeds the Wheeler-Chu bandwidth limits.

4.1 Broadband Ideal Non-Foster Match for Small Antennas

It is well known that electrically small antennas hava a high quality factor Q with the minimum achievable Q being physically limited by the electrical size of the antenna ka as seen in (1.1). In order to use non-Foster reactances to cancel the large reactance of the small antenna and overcome the quality factor limitation, it is helpful to calculate

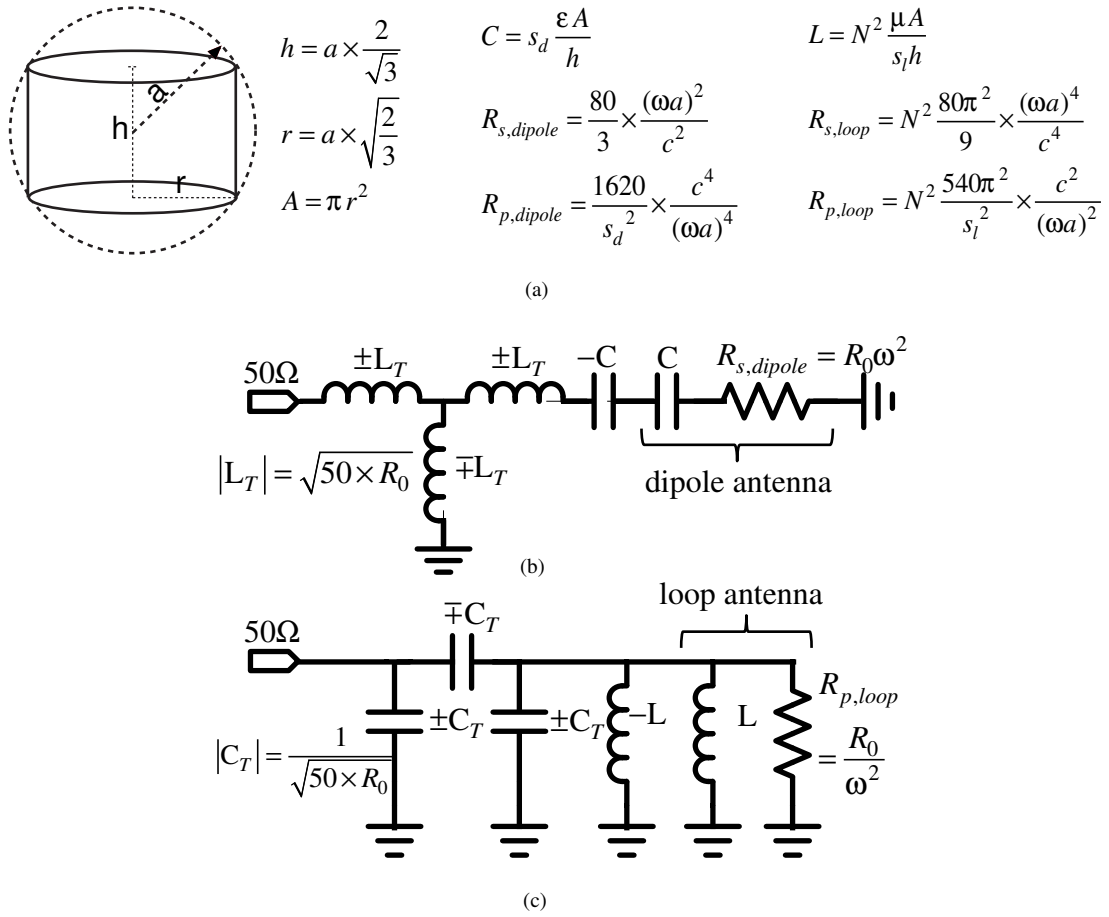

Figure 4.1. (a) Wheeler's model of a capacitive small dipole antenna and an inductive small loop antenna. (b) Broadband non-Foster matching network for a small dipole antenna. (c) Broadband non-Foster matching network for a small loop antenna.

the reactance of a small antenna. In 1947, Wheeler [1] modeled an electrically small dipole antenna as a parallel plate capacitor and a small loop antenna as an inductive coil, both occupying a cylindrical volume of height h and a radius r. Assuming that this cylinder is circumscribed in a sphere of radius a, the height and radius of the cylinder that maximizes its volume (thus minimizing the quality factor of the small antenna), can be mathematically derived to be $h = a\frac{2}{\sqrt{3}}$ and $r = a\sqrt{\frac{2}{3}}$. For a cylinder of such dimensions, the capacitance of the dipole antenna, the inductance of the loop antenna, and their respective radiation resistances and reactances can be found from [1] as shown

in Fig. 4.1(a). Here $R_{s,dipole}$ and $R_{s,loop}$ are the series radiation resistances of the dipole and the loop antenna. $R_{p,dipole}$ and $R_{p,loop}$ are the radiation resistances in parallel after transforming the antenna models from a series configuration to a parallel configuration. Since small antennas have a high quality factor, the reactances are approximately the same in both the series and parallel configurations, and so the capacitance of the dipole antenna and inductance of the loop antenna are the same in both configurations. s_d and s_l are shape factors for the dipole and the loop antenna, details on which can be found in [1]. Although more accurate expressions can be found for specific antenna types, the models used here are useful for identifying trends for small dipole and loop antennas.

It is apparent that even if the capacitance and inductance of the dipole and loop antennas were cancelled by ideal non-Foster elements, the frequency dependent radiation resistances of the antennas would prevent them from attaining a broadband match to a constant 50Ω. In [40], a solution was presented in terms of a dynamic dispersive impedance transformer with complementary Foster and non-Foster inductances that can transform a radiation resistance with a squared frequency dependence into a constant resistance, in this case 50Ω as shown in Fig. 4.1(b) for a dipole antenna. However, this solution would not work for a loop antenna whose radiation resistance has a fourth power dependence on frequency. We therefore introduce a new scheme of a dynamic dispersive impedance transformer for a loop antenna (Fig. 4.1(c)). Since loop antennas are usually matched with short circuit stable non-Foster inductances in shunt for stability, the parallel model of the loop antenna is considered. We observe that the shunt conductance of the loop antenna has a squared frequency dependence. This leads to an impedance transformer circuit with complementary Foster and non-Foster capacitances that can transform the frequency dependent conductance into a constant 50Ω as shown in (Fig. 4.1(c)). It should also be noted that both the inductive and capacitive non-Foster impedance transformers can be configured either as a π-network or a T-network.

While these ideal non-Foster matching schemes sound promising, in reality, minimizing the number of non-Foster elements is ideal for stability and simplicity.

4.2 Fabricated Non-Foster Match for a Capacitively Loaded Loop Antenna

A non-Foster match was designed for a capacitively loaded loop antenna [41, 42] as shown in Fig. 4.2. The antenna consists of a semi-circular loop antenna that is resonated in the near-field by a capacitive field that is realized using a cage like structure with a gap. The antenna can be matched in the required frequency range by further loading the gap with a capacitor. Alternatively, the impedance required to resonate the antenna across a broad bandwidth can be obtained as the interpolation of the impedances of all the individual resonating capacitors, and such an impedance will be found to have a non-Foster reactance. The required non-Foster reactance can also be obtained by looking into the input impedance at the gap, and negating the reactance of that impedance.

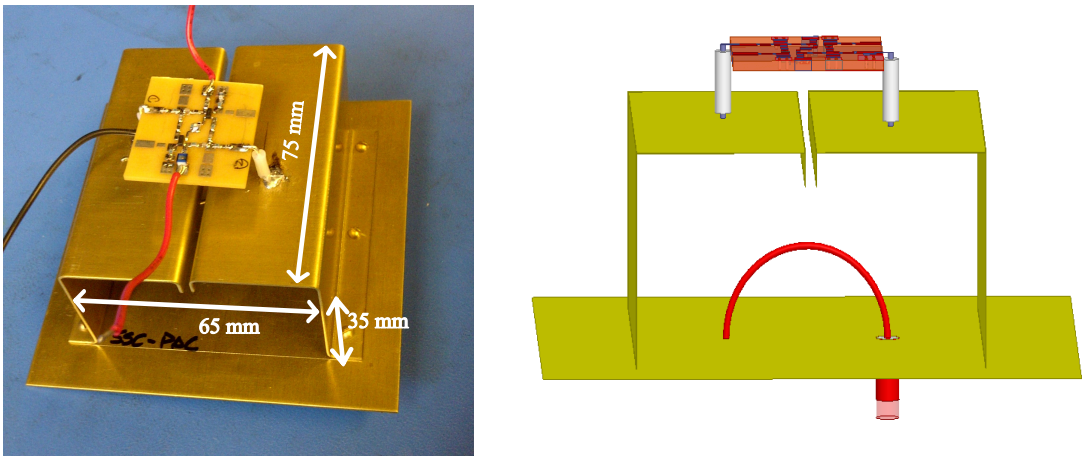

(a) (b)

Figure 4.2. (a) Fabricated non-Foster match for a capacitively loaded loop antenna. (b) Cosimulation model of the NIC circuit with the antenna.

The required non-Foster impedance was found to have a parallel $-L||-C$ re-

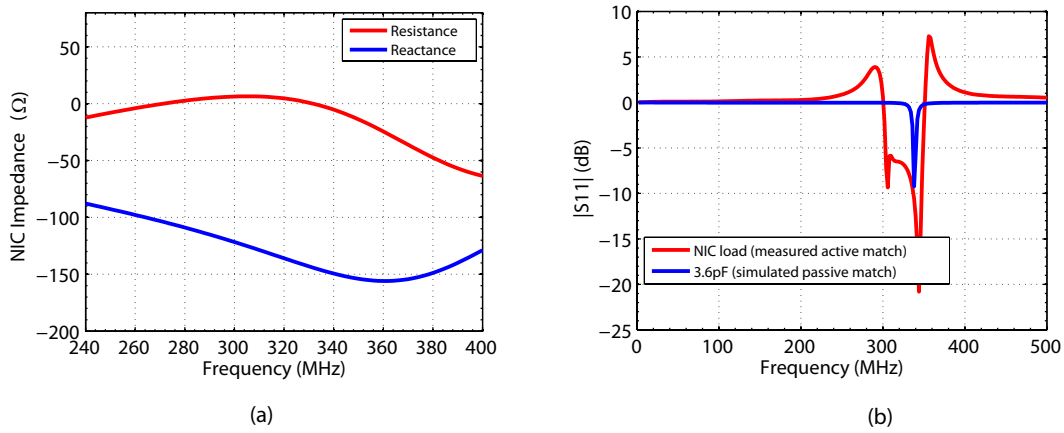

Figure 4.3. (a) Simulated NIC impedance. (b) Measured input match with the NIC circuit compared to the simulated passive match

actance. A full-wave simulation was performed with the antenna and the NIC layout as shown in Fig. 4.2(b). The simulated NIC impedance is shown in Fig. 4.3(a) and the measured input match of the non-Foster loaded antenna (at the input of the semi-circular loop underneath the ground plane) is shown in Fig. 4.3(b). It can be seen that the NIC offers a broadband -6 dB match from 303 MHz to 348 MHz, about 10 times the matching bandwidth offered by a resonating capacitor of 3.6 pF. At the mid-band matching frequency, the electrical size of the antenna(including the ground plane) is found to be ka=0.54. At this electrical size, the non-Foster matched bandwidth is equal to 1.1 times the Wheeler-Chu bandwidth limit. It can further be seen that the NIC loss is low in the matching bandwidth, ensuring a reactive match rather than a lossy match.

4.3 Fabricated Non-Foster Match for a Cylindrical Slot Antenna

A cylindrical slot antenna of diameter 16 cm, height 20 cm with a resonant slot of width 3 mm was designed as shown in Fig. 4.4(a). For this antenna, we designed a non-Foster matching network consisting of a $-97\ nH||-5.4\ pF$ NFC, and an inductive

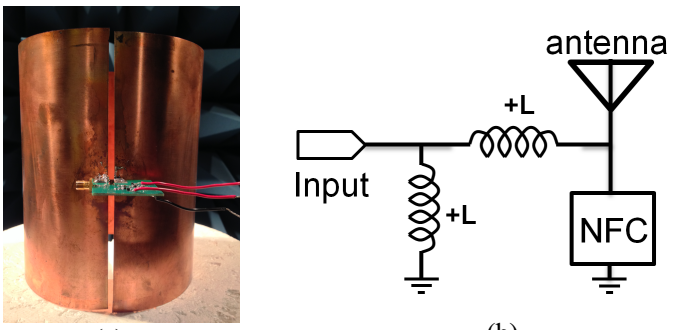

(a) (b)

Figure 4.4. (a) Cylindrical slot antenna with active matching network circuit. (b) Active matching network model with the inductive transformer and non-Foster circuit (NFC)

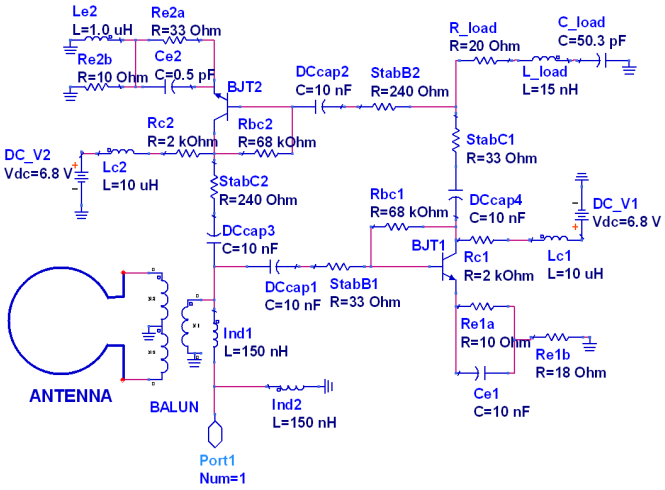

Figure 4.5. Schematic of the non-Foster matching network.

resistance transformer as shown in Fig. 4.4(b). The NFC cancels the reactance of the antenna, and the inductive transformer transforms the antenna's resistance to 50 ohm. The circuit schematic has been detailed in Fig. 4.5.

A co-simulation technique was used wherein an electromagnetic simulation software such as Ansys HFSS [24] was used to extract the layout parasitics and a circuit simulation software such as Keysight ADS [25] was used to attach actual device models to the layout. The transistors used were Avago AT41511 BJTs. The circuit was optimized to have low loss in the matching bandwidth, while providing the necessary reactance to cancel the reactance of the antenna. The NFC was designed to be stable with

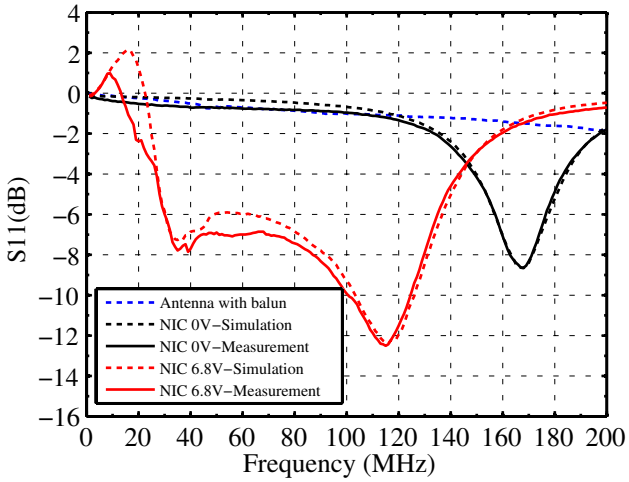

Figure 4.6. $|S_{11}|$ of the passive antenna and the NFC matched antenna.

the inductive resistance transformer and the antenna; therefore an accurate de-embedded NFC measurement could not be obtained. The $-L||-C$ circuit was implemented as a short circuit stable (SCS), single ended configuration [17]. Since this antenna has a balanced mode of operation, a balun was used to convert the antenna's balanced feed to the NFC's single ended feed. The input matching characteristics of the balun-fed antenna is shown in Fig. 4.6. The entire matching network consisting of the NFC and inductive transformer was fabricated on an FR-4 printed circuit board (PCB) and attached to the antenna. When the NFC bias was turned off, the inductive resistance transformer acted as a passive matching network and provided a measured -6 dB match from 157 MHz to 177 MHz as shown in Fig. 4.6. When the NFC bias was turned on, we achieved an improved measured -6 dB matching bandwidth from 30 MHz to 135 MHz. In Fig. 4.6, it is seen that $|S_{11}|$ is greater than 1 for some low frequencies. However, the NFC was found to be stable at all frequencies. The simulated and measured input matching characteristics are very similar as seen in Fig. 4.6. The measured bandwidth corresponds to

a measured antenna quality factor of 0.91 computed using [8]

$$Q_{meas} = \frac{1}{fractional\ bandwidth}\left(\frac{VSWR-1}{\sqrt{VSWR}}\right). \tag{4.1}$$

The Wheeler-Chu minimum antenna quality factor corresponding to an antenna of electrical size ka=0.28 at the matched center frequency is found to be 48.75 using [8]

$$Q_{Chu} = \frac{1}{ka} + \frac{1}{(ka)^3}. \tag{4.2}$$

Thus the active matching network provides a matching bandwidth that is 53.7 times the maximum Wheeler-Chu bandwidth for an antenna of electrical size ka=0.28.

4.4 Conclusion

Generalized broadband non-Foster matching networks have been detailed for the small dipole antenna model and the small loop antenna model. Measured results have also been presented for a non-Foster matched capacitively loaded loop antenna and a non-Foster matched cylindrical slot antenna. The results show that non-Foster matching can overcome the Wheeler-Chu bandwidth limits.

The efficiency of a passive impedance matching network is determined by its resistive loss. For an active matching network, the efficiency should not only be determined by the loss in the circuit, but also by the noise generated by the active and passive circuit components. A perfectly lossless active matching circuit can have 100% efficiency, but can still be detrimental to a receiving antenna if it adds more noise than the signal gain it provides. Therefore it is important to study the noise generated by the NFC and the matching network. A detailed noise analysis will be performed for the non-Foster matched cylindrical slot antenna in the next chapter.

Section 4.1 and 4.3 is based on the following paper which is under review: M. M. Jacob and D. F. Sievenpiper, ”Gain and Noise Analysis of Non-Foster Matched Antennas,” under review at *Antennas and Propagation, IEEE Transactions on*

Chapter 5

Non-Foster Matched Antennas for Receive Applications

The demand for miniaturized, broadband communication systems has created a need for electrically small, broadband antennas. However, all passive electrically small antennas have a fundamental gain-bandwidth limitation as first described by Wheeler [1] and Chu [3]. In recent years, active non-Foster circuits (NFCs) have been used to improve the matching bandwidth of electrically small antennas [12, 43, 44]. However, for an NFC matched antenna in the receiving mode, the noise added by the active NFC can degrade the received signal to noise ratio (SNR) beyond an acceptable limit and counteract the benefits of bandwidth improvement. While there have been quite a few publications on the improved matching bandwidth of NFC matched antennas, only few publications have examined the NFC's noise performance [12, 45]. But these publications present conflicting conclusions on the SNR advantage provided by non-Foster matched antennas. Further, their results have not been validated with corresponding measurements and simulations that can provide an understanding of the effects of environmental noise, the receiver's noise floor and circuit noise contributions.

With that objective, we designed a non-Foster matching network for a small antenna that provided a matching bandwidth from 30 MHz to 135 MHz, performed noise

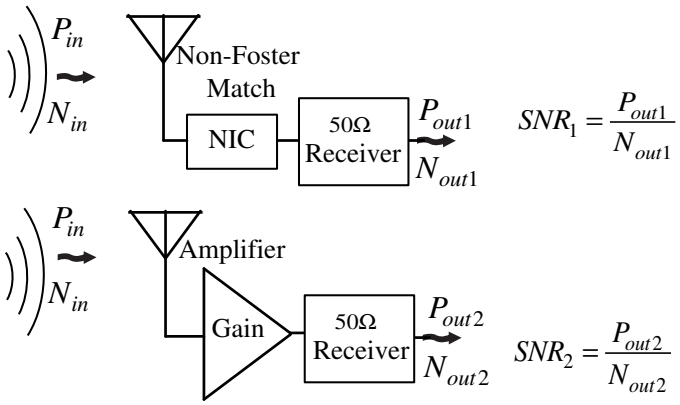

Figure 5.1. Received signal to noise ratio of a non-Foster matched antenna compared to that of a passive antenna attached to a low noise amplifier

simulations, and verified those simulation results with measurement results. We found that the non-Foster matched antenna did not provide a measured SNR improvement over the passive antenna, in contrast to the findings in [12]. We therefore undertook a detailed analysis of the various noise contributions in a non-Foster receiving system, namely from the environment, the receiver's noise floor and the NFC. Generalized noise models were derived for the balanced and unbalanced Linvill Negative Impedance Convertor circuits [17] to understand the effects of bias currents, transistors and attached RLC components. The alternative to non-Foster matching is to connect the antenna directly to an amplifier, as shown in Fig. 5.1. To provide a fair comparison, we analyze these two cases using the same transistor technology and bias conditions for the NFC and the amplifier. This paper will present the results of noise figure comparisons for both systems, for various biasing currents, small antenna types, and most importantly, for different internal noise floor levels of the receiver, to address the question of if or under what conditions non-Foster matching can provide an advantage in small antenna receive applications.

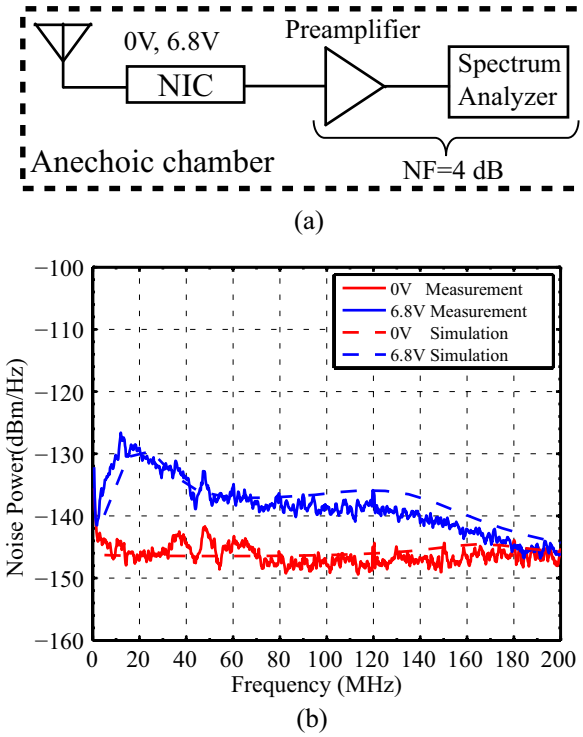

Figure 5.2. (a) Measurement setup to determine noise added by the NFC. (b) Measured and simulated noise power.

5.1 Gain and Noise Measurements for the Cylindrical Slot Antenna

A broadband non-Foster match was designed for a cylindrical slot antenna as presented in Chapter 4. In order to measure the received SNR improvement with the non-Foster match compared to a passive match, noise and gain measurements were performed for the non-Foster matched antenna and the passive matched antenna.

5.1.1 Noise Measurements

To perform accurate noise measurements, it is important to have a receiver that has a low noise figure (*NF*) or noise temperature (*NT*) so that small noise power levels will not be masked by the noise floor of the receiver. A Keysight EXA N9010A spectrum analyzer was used to measure the noise spectrum of our NFC matched antenna. Since

the spectrum analyzer had a noise figure of 23 dB as calculated from its noise floor power level, we attached a low noise preamplifier with a gain of 25 dB and a *NF* of 3 dB to the spectrum analyzer to obtain a receiver that had a low *NF* of 4 dB under matched conditions. The cylindrical slot antenna with the non-Foster matching network was attached to this receiver, and the entire system was placed in an anechoic chamber as shown in Fig. 5.2(a). The noise spectrum at the receiver(spectrum analyzer with preamplifier) was recorded when the NFC was turned off (0V) and on (6.8V) and the measured results are shown in Fig. 5.2(b). A noise simulation was also performed using ADS where the co-simulation model of the NFC was attached to the noise models of the preamplifier and spectrum analyzer. Thermal noise from the resistive loss in the balun has also been taken into account (both in measurements and simulations in Fig. 5.2(b)) for the active as well as the passive antenna. We see from Fig. 5.2(b) that the simulated noise is similar to the measured noise, validating our noise measurements. The total noise at the receiver is a measure of the received environmental noise, the added NFC noise, and the receiver noise floor. The added noise from the NFC cannot be isolated from the total measured noise, and so it is not possible to calculate the noise figure of this system. However, we can calculate the improvement in received SNR with non-Foster matching relative to the passive match with a measurement of the gain improvement.

5.1.2 Gain Measurements

To assess the signal gain provided by the matching network, we set up a measurement system in the anechoic chamber as shown in Fig. 5.3(a). The transmitting horn antenna was connected to port 1 of a vector network analyzer (VNA) and the NFC matched antenna with the preamplifier was attached to port 2 of the VNA. The frequency of the transmitted signal was swept from 5 MHz to 200 MHz and the S_{21} was measured with the NFC turned off (0V) and on (6.8V). The difference in S_{21} between the on and

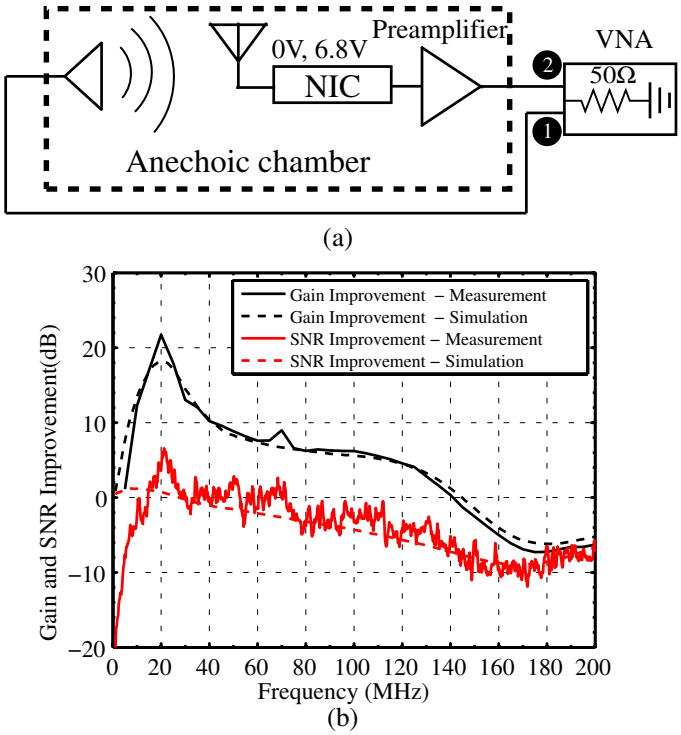

Figure 5.3. (a) Measurement setup to determine gain improvement with the NFC. (b) Gain improvement compared to the SNR improvement.

off case gives the gain improvement provided by the NFC over the passive match of the inductive transformer. The subtraction in S_{21} also eliminates the effects of path loss and cable loss common to both the on and off case. We see that the NFC provides a gain improvement greater than 0 dB in the low frequencies where $|S_{11}|$ of the NFC matched antenna is greater than 1, and also in the bandwidth where the 6.8V NFC provides better matching than the 0V NFC (Fig. 5.3(b) and Fig. 4.6). The measured gain improvement is very similar to the simulated gain improvement (also calculated using the difference in S_{21} between the on and off case of the NFC) as shown in Fig. 5.3(b). We see that in the matching bandwidth from 30 MHz to 135 MHz, the NFC provides an average 7 dB signal improvement. The improvement in gain is a measure of the difference in the received signal levels between the on and off case. The received noise levels have also been measured for the on and off case. The difference in the gain and noise levels

have been used to calculate the improvement in received SNR between the on and off case. From the simulated and measured results in Fig. 5.3(b), we see that there is no improvement in the received SNR in the matching bandwidth. Thus, although the non-Foster matching network provided a broad matching bandwidth and a high signal gain improvement over a passive match, the added noise resulted in a lower received SNR compared to a passive match.

These results are contradictory to the results presented in [12] wherein measured results showed an SNR advantage with non-Foster matching. Therefore we decided to conduct a thorough investigation of the gain and noise of non-Foster matched antennas, starting with the basis of ideal non-Foster matching for small antennas.

5.2 System Configuration for the Noise Analysis of Non-Foster Matched and Gain-Enhanced Passive Antennas

The basic simulation setup of Fig. 5.1 has been extended and shown in Fig. 5.4 for a non-Foster matched antenna system and in Fig. 5.5 for a gain-enhanced unmatched antenna system.

In Fig. 5.4(a), the antenna has been modeled as a reactance jX_{ANT} and a radiation resistance R_r with an antenna noise temperature T_{ANT} [46]. The values of jX_{ANT} and R_r have been calculated using the equations shown in Fig. 4.1(a). All loop antenna models presented in this paper assume that the number of turns $N = 2$. The antenna noise temperature T_{ANT} has been modeled as man-made environmental noise in quiet rural areas as reported in [47]. This frequency dependent antenna noise temperature has been defined in [47] using the antenna noise figure Fa as

$$Fa = 53.6 - 28.6\log(f) \tag{5.1}$$

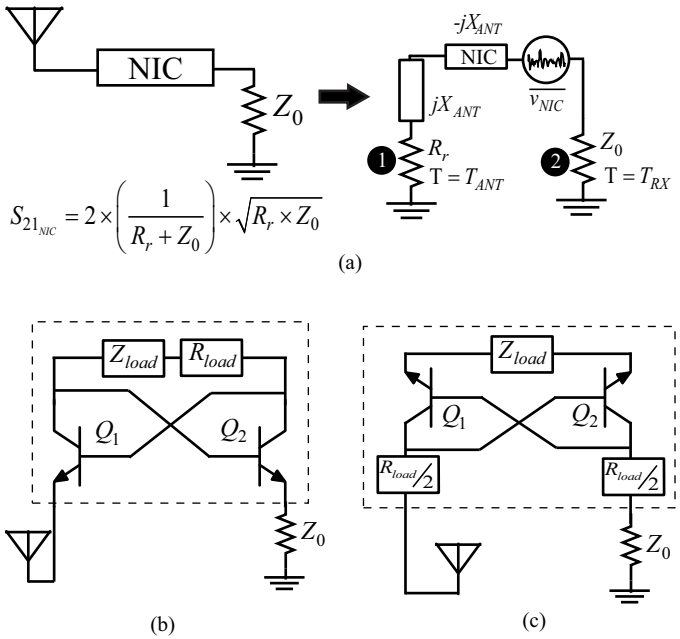

Figure 5.4. (a) A floating NIC attached to a small antenna and a noisy receiver. Ideal gain shown after a lossless reactance cancellation (b) An open circuit stable balanced NIC for a dipole antenna (c) A short circuit stable balanced NIC for a loop antenna.

where f is the frequency in MHz and Fa is defined as $Fa = dB(T_{ANT}/T_0)$ [48].

The receiver is represented as a resistance Z_0 with a noise temperature T_{RX} where T_{RX} is related to the noise factor F of the receiver as

$$T_{RX} = (F-1)T_0 \tag{5.2}$$

where T_0 is the standard noise temperature of 290K.

The importance of including the receiver's noise floor in the system's noise analysis has been pointed out in [49]. Typically, higher-frequency systems are internally noise-limited and lower-frequency systems are externally noise-limited. But if the lower-frequency systems have antennas with high mismatch or low efficiency such that the received noise power falls below the receiver's noise floor, these systems too can become internally noise-limited. It will be shown later that the noise floor of the receiver can

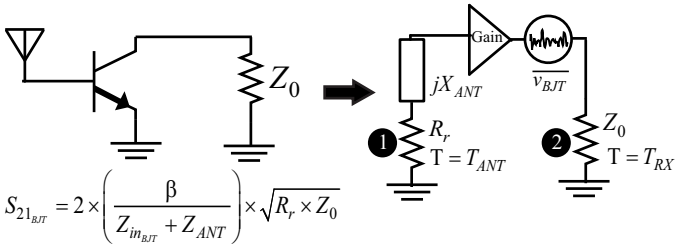

Figure 5.5. An amplifier attached to a small antenna and a noisy receiver.

affect the SNR advantage provided by non-Foster receiving systems.

The NIC is modeled as a perfectly lossless reactance $-jX_{ANT}$, along with an equivalent open circuit noise voltage $\overline{v_{NIC}}$ that is independent of any external loads attached to the NIC. If the NIC perfectly cancels the reactance of the antenna, then the gain of the system given by $|S21_{NIC}|^2$ between the radiation resistance of the antenna and the receiver is as shown in Fig. 5.4(a).

Fig. 5.4(b) and Fig. 5.4(c) represent general non-Foster matching systems for a dipole antenna and a loop antenna respectively. All non-Foster matching configurations considered in this paper will assume a simple balanced Linvill Negative Impedance Convertor (NIC) [17] that completely cancels the reactance of the antenna while the radiation resistance remains frequency dependent. A capacitive dipole antenna typically requires an open circuit stable (OCS) NIC for stability whereas an inductive loop antenna requires a short circuit stable (SCS) NIC for stability. In both NIC models, Z_{load} is a reactive impedance (capacitor in the case of the OCS NIC and inductor in the case of the SCS NIC) that is negated to cancel the reactance of the antenna. An ideal balanced Linvill NIC with a finite transistor transconductance g_m has an intrinsic resistive loss (positive resistive loss in the case of the OCS NIC and negative resistive loss in the case of the SCS NIC), so a compensating R_{load} is added to both models as shown to realize a perfectly lossless balanced NIC.

Fig. 5.5 represents a gain-enhanced antenna receiving system, with a simple BJT

amplifier providing the required gain. The bias network for the transistor has not been shown in the schematic. The antenna and receiver models are the same as for the non-Foster receiving systems, but the NIC of Fig. 5.4(a) has been replaced by a transistor along with the output-referred noise voltage of the transistor $\overline{v_{BJT}}$ [50]. The gain of this system given by $|S_{21_{BJT}}|^2$ between the radiation resistance of the antenna and the receiver is as shown in Fig. 5.5 where $Z_{in_{BJT}}$ is the input impedance seen looking into the transistor and β represents the current gain of the transistor.

A key difference between the non-Foster receiving system and the gain-enhanced antenna system is that the non-Foster receiving system can only have a maximum gain of 1 whereas the gain-enhanced antenna system can have a gain much greater than 1 depending on the current gain β of the transistor. Another important difference between the two systems is that the NIC is reciprocal while the amplifier is not. In the non-Foster receiving system, the internal noise of the receiver gets transmitted through the NIC and radiated out through the antenna based on the reciprocal gain $|S_{21_{NIC}}|^2$ of the system. However, in the gain-enhanced passive antenna, the internal noise of the receiver sees a large impedance at the output of the amplifier and is retained at the receiver. The ramifications of these differences become apparent while analyzing overall system noise figures for receivers with a high internal noise floor.

The overall system noise factor F is defined as the total noise power at the receiver divided by the transmitted input noise power. The noise figure NF is the noise factor expressed in decibels (dB).

$$NF = 10\log\left(1+\frac{N_{NIC/BJT}+N_{RX_{NIC/BJT}}}{N_{in}\cdot Gain_{NIC/BJT}}\right) \tag{5.3}$$

where $N_{NIC/BJT}$ is the noise power from the NIC or the BJT seen at the receiver. This can be obtained after a voltage division of $\overline{v_{NIC}}$ or $\overline{v_{BJT}}$ at Z_0 to obtain $\overline{v_{n,Zo}}$, and computing

the noise power as $|\overline{v_{n,Zo}}|^2/Z_0$. The internal receiver noise power retained at the receiver for the NIC matched antenna or the gain-enhanced antenna is denoted as $N_{RX_{NIC/BJT}}$ and can be less than the original noise floor if the system is reciprocal. The input noise power N_{in} is given by kT_{ANT}. Equations for each of these parameters will be derived in the subsequent sections.

The output noise voltage of the BJT amplifier has been previously derived [50, 51] and so we will focus on the noise model of the NIC in the next section.

5.3 Noise Model of the NIC

The general topology of the Negative Impedance Convertor circuit is shown in Fig. 5.6(a) along with the simplified unbalanced input impedances seen looking into each of the 4 ports. The balanced OCS input impedance is seen looking into ports Z_1 and Z_2 and the balanced SCS input impedance is seen looking into ports Z_3 and Z_4.

Fig. 5.6(b) is the extended topology of Fig. 5.6(a) showing the small signal model of the two transistors along with the noise sources of the transistors [50] and the attached loads. The intrinsic base-emitter capacitor and base-collector capacitor of the transistors have been excluded for simplicity, both in the model and the subsequent simulations. All resistors, including the base resistor r_b, the collector resistor r_c, the emitter resistor r_e, and the real part of the attached loads Z_1, Z_2, Z_3 and Z_4, have a thermal noise voltage $\overline{v_{r_b}}$, $\overline{v_{r_c}}$, $\overline{v_{r_e}}$, $\overline{v_{z_1}}$, $\overline{v_{z_2}}$, $\overline{v_{z_3}}$ and $\overline{v_{z_4}}$ associated with them. These noise voltages are considered as sinusoidal generators with root mean-square values equal to $\sqrt{4kTR}$. The collector current and base current have corresponding shot noise currents represented as $\overline{i_c}$ and $\overline{i_b}$, with rms values equal to

$$\overline{i_c} = \sqrt{2qI_c} \tag{5.4}$$

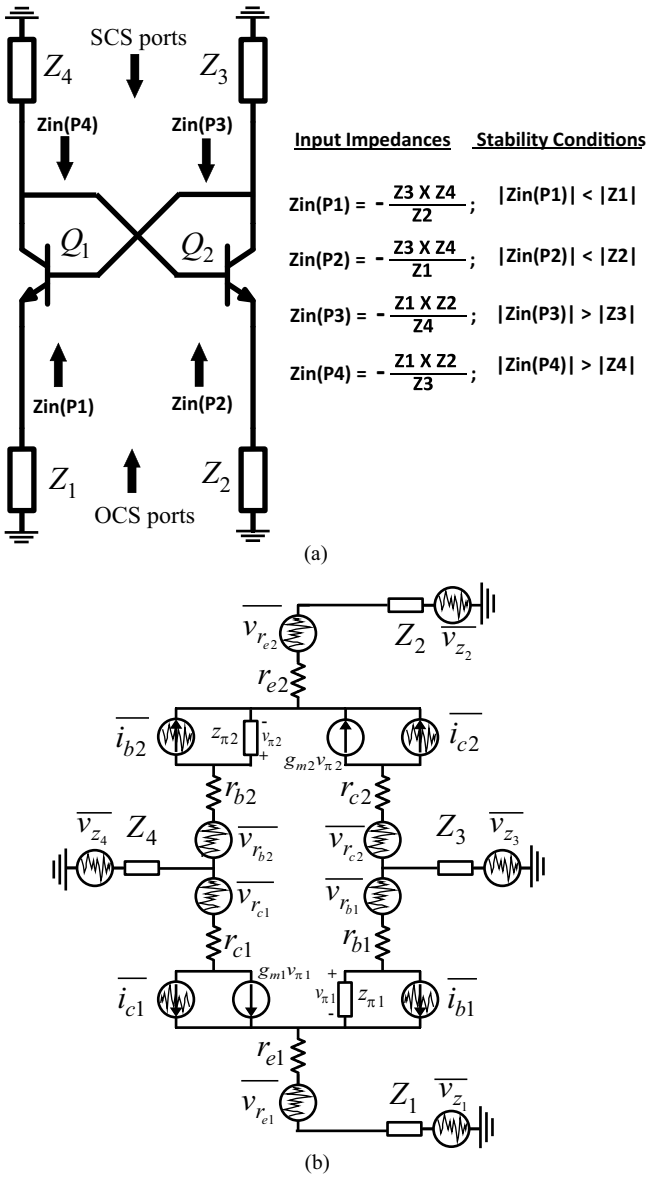

Figure 5.6. (a) General topology of a negative impedance convertor (NIC) circuit and the input impedances seen into each of the four ports (b) Representation of the voltage and current noise sources in a general NIC configuration.

and

$$\overline{i_b} = \sqrt{2q\frac{I_c}{\beta}} \tag{5.5}$$

where I_c is the collector bias current and β is the current gain. Burst noise and flicker noise in the base current have been ommitted for simplicity. This general circuit model

$$Z_{in_{OCS,U}} \approx r_{e1} + \frac{1}{g_{m1}} - \frac{g_{m2}Z_3Z_4}{1+g_{m2}(r_{e2}+Z_2)}$$

$$\overline{v_{i_{c1,eq}}} \approx \left|\overline{i_{c1}} \times \left[Z_{in_{OCS,U}} - r_{e1} + Z_4\left(\frac{g_{m2}Z_3}{1+g_{m2}(r_{e2}+Z_2)}\right)\right]\right|$$

$$\overline{v_{i_{c2,eq}}} \approx \left|\overline{i_{c2}} \times \left[Z_2\left(\frac{g_{m2}Z_3}{1+g_{m2}(r_{e2}+Z_2)}\right) - Z_3\right]\right|$$

$$\overline{v_{i_{b1,eq}}} = \left|\overline{i_{b1}} \times \left[Z_{in_{OCS,U}} - r_{e1} - r_{b1} - Z_3\right]\right|$$

$$\overline{v_{i_{b2,eq}}} \approx \left|\overline{i_{b2}} \times \left[(Z_4 + r_{b2} + Z_2)\left(\frac{g_{m2}Z_3}{1+g_{m2}(r_{e2}+Z_2)}\right)\right]\right|,$$

where $\overline{i_c} = \sqrt{2qI_c}$ and $\overline{i_b} = \sqrt{2q\frac{I_c}{\beta}}$.

$$\overline{v_{r_{e1,eq}}} = \sqrt{4kTr_{e1}}$$

$$\overline{v_{r_{e2,eq}}} \approx \left|\sqrt{4kTr_{e2}} \times \left(\frac{g_{m2}Z_3}{1+g_{m2}(r_{e2}+Z_2)}\right)\right|$$

$$\overline{v_{r_{b1,eq}}} = \sqrt{4kTr_{b1}}$$

$$\overline{v_{r_{b2,eq}}} \approx \left|\sqrt{4kTr_{b2}} \times \left(\frac{g_{m2}Z_3}{1+g_{m2}(r_{e2}+Z_2)}\right)\right|$$

$$\overline{v_{z_{2,eq}}} \approx \left|\sqrt{4kT * real(Z_2)} \times \left(\frac{g_{m2}Z_3}{1+g_{m2}(r_{e2}+Z_2)}\right)\right|$$

$$\overline{v_{z_{3,eq}}} = \sqrt{4kT * real(Z_3)}$$

$$\overline{v_{z_{4,eq}}} \approx \left|\sqrt{4kT * real(Z_4)} \times \left(\frac{g_{m2}Z_3}{1+g_{m2}(r_{e2}+Z_2)}\right)\right|$$

(a)

$$Z_{in_{SCS,U}} \approx -\frac{(1+g_{m1}(Z_1+r_{e1}))(1+g_{m2}(Z_2+r_{e2}))}{g_{m1}g_{m2}Z_3}$$

$$\overline{v_{i_{c1,eq}}} \approx \left|\overline{i_{c1}} \times \left[Z_{in_{SCS,U}} + (Z_1+r_{e1})\left(\frac{1+g_{m2}(Z_2+r_{e2})}{g_{m2}Z_3}\right)\right]\right|$$

$$\overline{v_{i_{c2,eq}}} \approx \left|\overline{i_{c2}} \times \left[Z_3\left(\frac{1+g_{m2}(Z_2+r_{e2})}{g_{m2}Z_3}\right) - (Z_2+r_{e2})\right]\right|$$

$$\overline{v_{i_{b1,eq}}} \approx \left|\overline{i_{b1}} \times \left[(Z_3 + r_{b1} + Z_1 + r_{e1})\left(\frac{1+g_{m2}(Z_2+r_{e2})}{g_{m2}Z_3}\right)\right]\right|$$

$$\overline{v_{i_{b2,eq}}} = \left|\overline{i_{b2}} \times \left[Z_{in_{SCS,U}} - (Z_2+r_{e2}) - r_{b2}\right]\right|,$$

where $\overline{i_c} = \sqrt{2qI_c}$ and $\overline{i_b} = \sqrt{2q\frac{I_c}{\beta}}$.

$$\overline{v_{r_{e1,eq}}} \approx \left|\sqrt{4kTr_{e1}} \times \left(\frac{1+g_{m2}(Z_2+r_{e2})}{g_{m2}Z_3}\right)\right|$$

$$\overline{v_{r_{e2,eq}}} = \sqrt{4kTr_{e2}}$$

$$\overline{v_{r_{b1,eq}}} \approx \left|\sqrt{4kTr_{b1}} \times \left(\frac{1+g_{m2}(Z_2+r_{e2})}{g_{m2}Z_3}\right)\right|$$

$$\overline{v_{r_{b2,eq}}} = \sqrt{4kTr_{b2}}$$

$$\overline{v_{z_{1,eq}}} \approx \left|\sqrt{4kT * real(Z_1)} \times \left(\frac{1+g_{m2}(Z_2+r_{e2})}{g_{m2}Z_3}\right)\right|$$

$$\overline{v_{z_{2,eq}}} = \sqrt{4kT * real(Z_2)}$$

$$\overline{v_{z_{3,eq}}} \approx \left|\sqrt{4kT * real(Z_3)} \times \left(\frac{1+g_{m2}(Z_2+r_{e2})}{g_{m2}Z_3}\right)\right|$$

(b)

Figure 5.7. (a) Input-referred equivalent noise sources for an unbalanced, open circuit stable NIC (b) Input-referred equivalent noise sources for an unbalanced, short circuit stable NIC.

is used to derive the equivalent open circuit noise voltage $\overline{v_{NIC}}$ for 4 different configurations, namely, an unbalanced OCS NIC looking into Z_1 (Fig. 5.7(a)), an unbalanced SCS NIC looking into Z_4 (Fig. 5.7(b)), a balanced OCS NIC looking into $Z_1 - Z_2$ (Fig. 5.8(a))

$$Z_{in_{OCS,B}} \approx r_{e1} + r_{e2} + \frac{1}{g_{m1}} + \frac{1}{g_{m2}} - Z_{load} - R_{load}$$

$$\overline{v_{i_{c,eq}}} = \left| \overline{i_c} \times \left[\frac{Z_{load}}{2} + \frac{Z_{in_{OCS,B}}}{2} - r_e + \frac{R_{load}}{2} \right] \right|$$

$$\overline{v_{i_{b,eq}}} = \left| \overline{i_b} \times \left[\frac{Z_{load}}{2} - \frac{Z_{in_{OCS,B}}}{2} + r_e + r_b + \frac{R_{load}}{2} \right] \right|,$$

where $\overline{i_c} = \sqrt{2qI_c}$ and $\overline{i_b} = \sqrt{2q\frac{I_c}{\beta}}$.

$$\overline{v_{r_{e,eq}}} = \sqrt{4kTr_e}$$

$$\overline{v_{r_{b,eq}}} = \sqrt{4kTr_b}$$

$$\overline{v_{R_{load,eq}}} = \sqrt{4kTR_{load}}$$

(a)

$$Z_{in_{SCS,B}} \approx -r_{e1} - r_{e2} - \frac{1}{g_{m1}} - \frac{1}{g_{m2}} - Z_{load} + R_{load}$$

$$\overline{v_{i_{c,eq}}} = \left| \overline{i_c} \times \left[\frac{Z_{load}}{2} + \frac{Z_{in_{SCS,B}}}{2} + r_e - \frac{R_{load}}{2} \right] \right|$$

$$\overline{v_{i_{b,eq}}} = \left| \overline{i_b} \times \left[\frac{Z_{load}}{2} - \frac{Z_{in_{SCS,B}}}{2} + r_e + r_b + \frac{R_{load}}{2} \right] \right|,$$

where $\overline{i_c} = \sqrt{2qI_c}$ and $\overline{i_b} = \sqrt{2q\frac{I_c}{\beta}}$.

$$\overline{v_{r_{e,eq}}} = \sqrt{4kTr_e}$$

$$\overline{v_{r_{b,eq}}} = \sqrt{4kTr_b}$$

$$\overline{v_{R_{load,eq}}} = \sqrt{4kTR_{load}}$$

(b)

Figure 5.8. (a) Input-referred equivalent noise sources for a balanced, open circuit stable NIC (b) Input-referred equivalent noise sources for a balanced, short circuit stable NIC.

$$\overline{v_{NIC_{OCS,U}}} = \sqrt{\left|\overline{v_{i_{c1,eq}}}\right|^2 + \left|\overline{v_{i_{c2,eq}}}\right|^2 + \left|\overline{v_{i_{b1,eq}}}\right|^2 + \left|\overline{v_{i_{b2,eq}}}\right|^2 + \left|\overline{v_{r_{e1,eq}}}\right|^2 + \left|\overline{v_{r_{e2,eq}}}\right|^2 + \left|\overline{v_{r_{b1,eq}}}\right|^2 + \left|\overline{v_{r_{b2,eq}}}\right|^2 + \left|\overline{v_{z_{2,eq}}}\right|^2 + \left|\overline{v_{z_{3,eq}}}\right|^2 + \left|\overline{v_{z_{4,eq}}}\right|^2}$$

$$\overline{v_{NIC_{SCS,U}}} = \sqrt{\left|\overline{v_{i_{c1,eq}}}\right|^2 + \left|\overline{v_{i_{c2,eq}}}\right|^2 + \left|\overline{v_{i_{b1,eq}}}\right|^2 + \left|\overline{v_{i_{b2,eq}}}\right|^2 + \left|\overline{v_{r_{e1,eq}}}\right|^2 + \left|\overline{v_{r_{e2,eq}}}\right|^2 + \left|\overline{v_{r_{b1,eq}}}\right|^2 + \left|\overline{v_{r_{b2,eq}}}\right|^2 + \left|\overline{v_{z_{1,eq}}}\right|^2 + \left|\overline{v_{z_{2,eq}}}\right|^2 + \left|\overline{v_{z_{3,eq}}}\right|^2}$$

$$\overline{v_{NIC_B}} = \sqrt{2\left|\overline{v_{i_{c,eq}}}\right|^2 + 2\left|\overline{v_{i_{b,eq}}}\right|^2 + 2\left|\overline{v_{r_{e,eq}}}\right|^2 + 2\left|\overline{v_{r_{b,eq}}}\right|^2 + \left|\overline{v_{R_{load,eq}}}\right|^2}$$

Figure 5.9. Total input-referred equivalent noise voltage for the unbalanced and balanced NIC.

and a balanced SCS NIC looking into $Z_3 - Z_4$ (Fig. 5.8(b)). For each of these configurations, the input of the NIC is left as an open and the individual noise sources are referred to the input. Each internal noise source is considered in turn and standard sinusoidal circuit analysis calculations are used to transform each noise source to a corresponding equivalent open circuit noise voltage at the input. The equivalent noise transformations are shown in Fig. 5.7 and Fig. 5.8 for all 4 configurations of the Linvill NIC. For instance, in Fig. 5.7(a), $Z_{in_{OCS,U}}$ is the input impedance of the unbalanced, open circuit stable NIC configuration seen looking into Z_1. The noise voltage $\overline{v_{i_{c1,eq}}}$ is the equivalent

open circuit noise voltage at the input due to the noise source $\overline{i_{c1}}$ from the collector current of transistor $Q1$ in Fig. 5.6(b). It is interesting to note that $\overline{v_{i_{c1,eq}}}$ is a a function of the input impedance $Z_{in_{OCS,U}}$. Similar equations have been derived for all internal noise sources. For ease of representation, the equations shown are approximations assuming a large $z_{\pi 1}$ and $z_{\pi 2}$ in Fig. 5.6(b). The thermal noise voltage associated with the collector resistor has a negligible effect since it is in series with a high collector impedance. Since all the individual noise sources are independent, the total noise voltage $\overline{v_{NIC}}$ at the input is the square root of the sum of the individual input-referred mean-square noise voltages as shown in Fig. 5.9. For the balanced NIC models, the input-referred noise voltages are identical for the two transistors, leading to a factor of 2 for the mean-square noise voltages within the equation for $\overline{v_{NIC_B}}$. Thus, the equations in Fig. 5.9 represent the total open circuit equivalent noise voltage $\overline{v_{NIC}}$ in Fig. 5.4(a).

An interesting result of this analysis is the discovery that the total equivalent noise of the NIC is proportional to the magnitude of the input impedance of the NIC for all 4 configurations of the NIC. This becomes apparent after simplifying the equations in Fig. 5.7 and Fig. 5.8 assuming a very large transconductance g_m, and a near-zero emitter resistance and base resistance. It will be seen that in such ideal conditions, the majority of noise comes from the base current's shot noise. To illustrate this for the balanced, open circuit stable NIC in Fig. 5.8(a), approximations of infinite transconductance and near-zero emitter resistance and base resistance(which eliminates the need for loss compensation using R_{load}) are used to simplify the equations. This results in the input impedance $Z_{in_{OCS,B}}$ being equal to $-Z_{load}$. Using this result, we see that $\overline{v_{i_{c,eq}}}$ goes to 0. The only non-zero equivalent noise voltage in Fig. 5.8(a) is $\overline{v_{i_{b,eq}}} = |i_b \times Z_{load}|$. Thus we see that the total equivalent noise is proportional to the impedance of the NIC. A similar analysis can be done for all four models of the NIC in Fig. 5.7 and Fig. 5.8. Further, with the knowledge of these equations, we can choose a combination of exter-

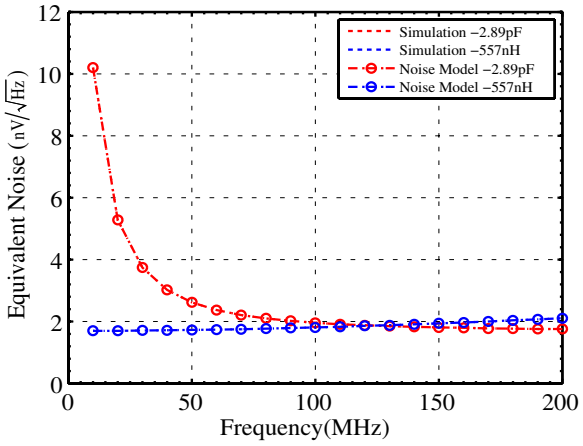

Figure 5.10. Simulated and calculated total input-referred equivalent noise for a balanced OCS negative capacitor and a balanced SCS negative inductor.

nal loads Z_1, Z_2, Z_3 and Z_4 that will yield the minimum noise for a specific required non-Foster impedance. For instance, if an SCS unbalanced $-L$ were required looking into port Z_4, a configuration with Z_2 as an inductor and Z_1, Z_3 as resistors would yield the minimum noise as opposed to inverting a capacitor at Z_3.

Noise simulations were done in Keysight ADS using the die model of the Avago transistor AT41511, but with the internal capacitors set to zero. The same transistor model was used to mathematically calculate the equivalent noise $\overline{v_{NIC}}$ using the complete form of the equations in Fig. 5.9 (including correct values of $z_{\pi 1}$ and $z_{\pi 2}$). An exact match was obtained between the simulated and calculated results as shown in Fig. 5.10 for a balanced OCS negative capacitor and a balanced SCS negative inductor. A bias current of 0.5 mA was set for all the transistors, and required values of R_{load} were set to compensate for the intrinsic loss of the NIC. The values of $-C$ and $-L$ were chosen to cancel the reactance of a small dipole and a small loop that fit within a sphere of radius $a = 10$ *cm* as shown in Fig. 4.1(a). We can further see from the calculated equivalent noise voltages that the noise voltage of the $-C$ and $-L$ NIC have the same frequency dependence as the magnitude of their respective non-Foster impedances. The unbalanced

noise model's equations were also verified with simulations and found to be an exact match. After verifying the noise models, we proceeded to noise figure simulations of the non-Foster matched and gain-enhanced passive antennas.

5.4 Noise Figure of Non-Foster Matched and Gain-Enhanced Small Antennas

Noise figure simulations were done using the simulation setup in Fig. 5.4(b) for a non-Foster matched small dipole antenna and the setup in Fig. 5.4(c) for a non-Foster matched small loop antenna. The setup in Fig. 5.5 was used to simulate the noise figure of a gain-enhanced dipole antenna as well as a gain-enhanced loop antenna. The simulated noise figure corresponds to the calculation in (5.3). The parameters in (5.3) can be further expanded as shown below.

$$N_{NIC} = \left| \overline{v_{NIC}} \times \frac{Z_0}{Z_0 + Z_{in_{NIC}} + Z_{ANT}} \right|^2 \times \frac{1}{Z_0} \tag{5.6}$$

$$N_{BJT} = \left| \overline{v_{BJT}} \times \frac{Z_0}{Z_0 + Z_{out_{BJT}}} \right|^2 \times \frac{1}{Z_0} \tag{5.7}$$

$$N_{RX_{NIC}} = \left| 2\sqrt{kT_{RX}Z_0} \cdot \frac{Z_{in_{NIC}} + Z_{ANT}}{Z_0 + Z_{in_{NIC}} + Z_{ANT}} \right|^2 \times \frac{1}{Z_0} \tag{5.8}$$

$$N_{RX_{BJT}} = \left| 2\sqrt{kT_{RX}Z_0} \times \frac{Z_{out_{BJT}}}{Z_0 + Z_{out_{BJT}}} \right|^2 \times \frac{1}{Z_0} \tag{5.9}$$

$$N_{in} \cdot Gain_{NIC/BJT} = kT_{ANT} \times |S_{21_{NIC/BJT}}|^2 \tag{5.10}$$

In the above equations, N_{NIC} and N_{BJT} correspond to noise from the NIC and the BJT respectively, delivered to the receiver of impedance Z_0. $Z_{in_{NIC}}$ is the input impedance of the NIC given by the equations in Fig. 5.7 and Fig. 5.8 and Z_{ANT} is the impedance of the antenna, given by the equations in Fig. 4.1(a). $Z_{out_{BJT}}$ is the impedance

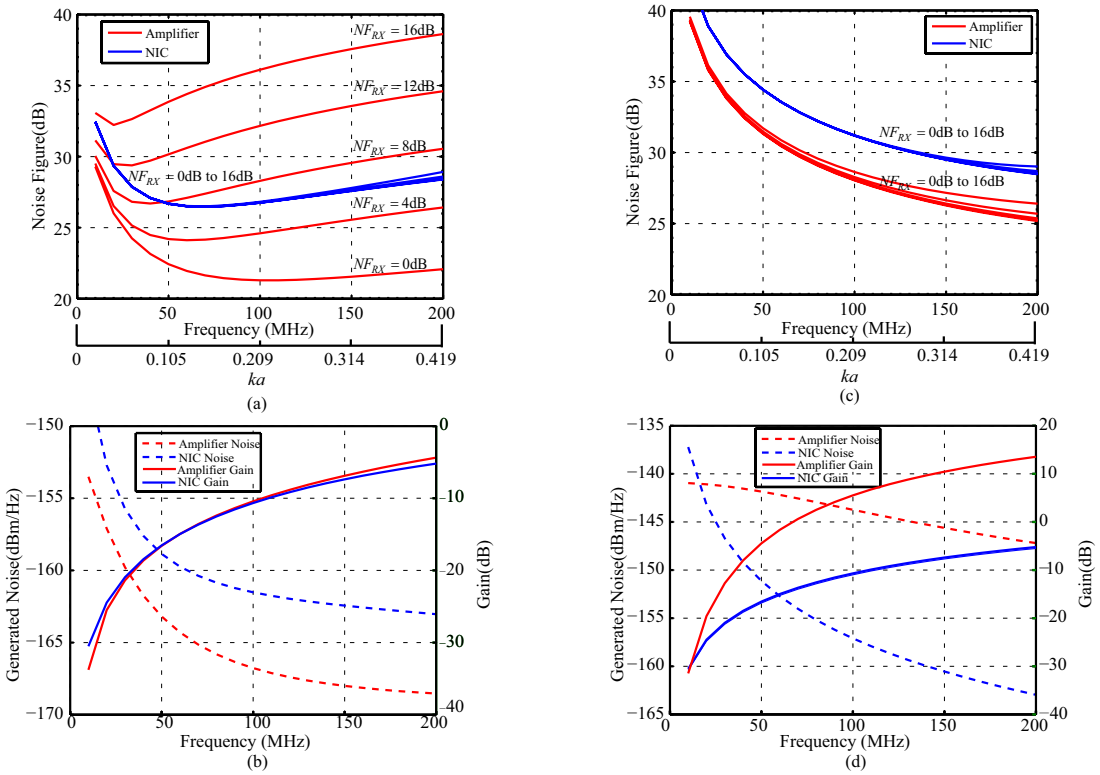

Figure 5.11. (a) Noise figure comparison between a non-Foster matched and gain-enhanced dipole antenna for different noisy receivers, where all transistors are biased at 0.5mA (b) Noise generated by the -C NIC and the amplifier at the 50Ω receiver, and the net gain comparison for both systems, where all transistors are biased at 0.5mA (c) Noise figure comparison between a non-Foster matched and gain-enhanced dipole antenna for different noisy receivers, where all transistors are biased at 5mA (d) Noise generated by the -C NIC and the amplifier at the 50Ω receiver, and the net gain comparison for both systems, where all transistors are biased at 5mA.

seen looking from the receiver into the output of the amplifier in Fig. 5.5. T_{RX} and T_{ANT} are noise temperatures of the receiver the antenna as defined in previous sections.These equations are helpful in analyzing the results that are presented in the following subsections.

5.4.1 Noise Figure Comparison for a Small Dipole Antenna

First, a small dipole antenna was assumed to fit within a sphere of radius $a = 10\ cm$ as shown in Fig. 4.1(a) and the relevant antenna parameters were calculated. The

same dipole was attached to an NIC and the input of a BJT as shown in Fig. 5.4(b) and Fig. 5.5 respectively. All transistors were biased with a collector current of $I_c = 0.5\ mA$ and the required R_{load} was added to the NIC to realize a lossless NIC. In both systems, the receiver's noise figure was swept from 0 dB (ideal noiseless receiver) to 16 dB and the overall system noise figure was simulated as shown in Fig. 5.11(a). The added noise from the NIC and the BJT as seen at the receiver ($N_{NIC/BJT}$) has been plotted in Fig. 5.11(b) along with the net gain of both systems. Fig. 5.11(a) shows that the noise figure of the non-Foster matched small dipole antenna is largely independent of the swept receiver noise levels, unlike the gain-enhanced antenna system. This is because the internal noise of the receiver gets radiated back out through the antenna in the reciprocal non-Foster system, leading to a receiver noise level $N_{RX_{NIC}}$ in (5.3) that is about 20 dB less than the noise level $N_{RX_{BJT}}$ of the gain-enhanced antenna system, as verified through (5.8) and (5.9).Therefore the effect of N_{RX} in (5.3) can be neglected for the non-Foster matched antenna system. It is thus seen that for receivers with noise figures below 6 dB, the non-Foster matched antenna has a higher overall system noise figure compared to the gain-enhanced antenna system. It is only when the receiver is noisy with noise figures above 6 dB, that the non-Foster matched antenna provides a received SNR advantage compared to the gain-enhanced passive antenna.

The simulations have been repeated for a transistor bias current of 5 mA for all transistors, and the results have been plotted in Fig. 5.11(c) and Fig. 5.11(d). For such a large bias current, both the NIC and the BJT generate higher noise power levels as shown in Fig. 5.11(d). Further, the noise generated by the BJT overpowers the internal noise of the receiver, leading to an overall system noise figure that is fairly independent of the internal noise of the receiver. For the non-Foster matched antenna, the internal noise of the receiver gets radiated away as before, and the overall system noise figure is again independent of the noise floor of the receiver. The most important difference

between the two biasing conditions is in the gain of the two systems. The BJT provides a much larger gain than the non-Foster matched antenna, leading to overall lower system noise figures for all considered receivers.

Thus, if there are constraints on the DC power consumption, the non-Foster matched antenna could provide an SNR advantage over the gain-enhanced antenna, but only for noisy receivers with a fairly high noise floor. If there are no constraints on the DC power consumption, it is possible to increase the gain of the amplifier to a level that provides an SNR advantage over non-Foster matched antennas for all practical receivers.

5.4.2 Noise Figure Comparison for a Small Loop Antenna

The noise figure simulations were repeated for a small loop antenna that was assumed to fit within a sphere of radius $a = 10\ cm$. Similar results were obtained as for the small dipole antenna. It is again interesting to note that for a bias condition of $I_c = 0.5\ mA$ for all transistors, the non-Foster matching system is better than the gain-enhanced passive system only for receivers of noise figure 6 dB and above. Under a bias condition of $I_c = 5\ mA$, the gain-enhanced loop antenna is better than the non-Foster matched loop antenna for all considered receivers.

It is also important to note that even if we were to force the power consumption to be the same in both the non-Foster system and the gain enhanced system by supplying twice the bias current of the NIC's transistors to the BJT, the gain-enhanced system would still provide an SNR advantage over the non-Foster receiving system for practical, low noise receivers.

5.4.3 Noise Figure vs. Antenna Size

The results obtained for the dipole antenna and loop antenna raise questions as to the validity of those conclusions for different small antenna sizes. Therefore we

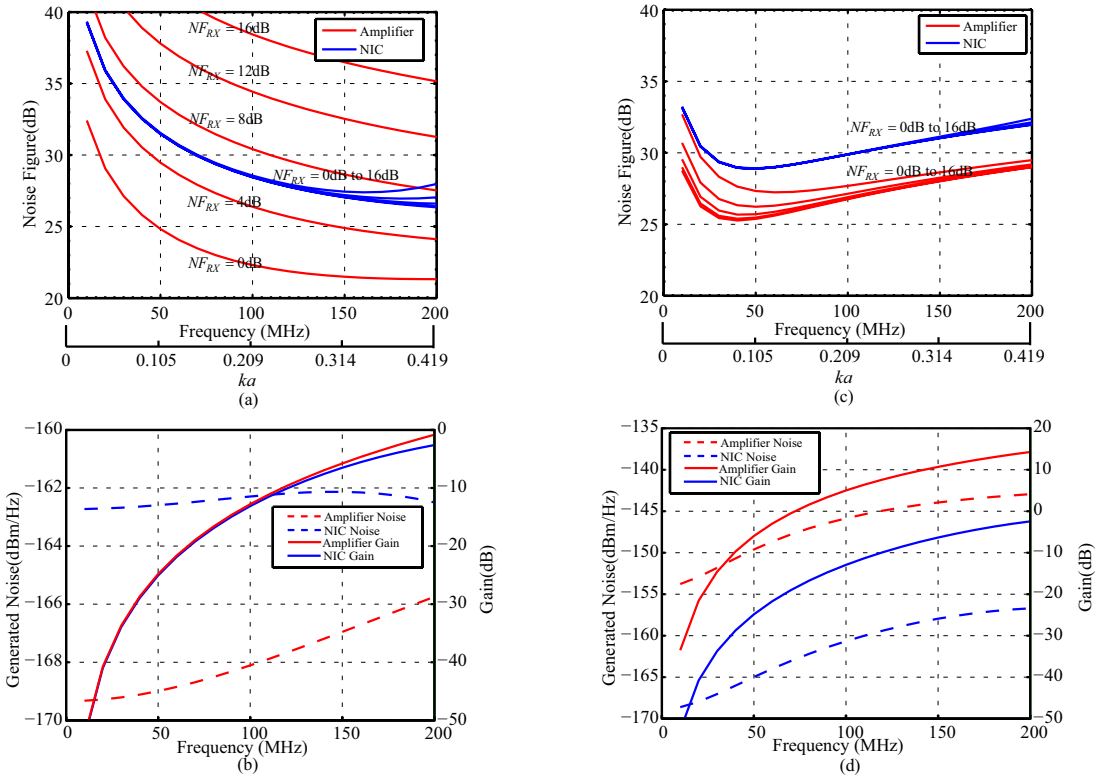

Figure 5.12. (a) Noise figure comparison between a non-Foster matched and gain-enhanced loop antenna for different noisy receivers, where all transistors are biased at 0.5mA (b) Noise generated by the -L NIC and the amplifier at the 50Ω receiver, and the net gain comparison for both systems, where all transistors are biased at 0.5mA (c) Noise figure comparison between a non-Foster matched and gain-enhanced loop antenna for different noisy receivers, where all transistors are biased at 5mA (d) Noise generated by the -L NIC and the amplifier at the 50Ω receiver, and the net gain comparison for both systems, where all transistors are biased at 5mA.

repeated the simulations for different small antennas assumed to fit within spheres of radius 10 cm, 20 cm, 30 cm, 40 cm and 50 cm, ranging in electrical size from $ka = 0.2095$ to $ka = 1.0472$ at 100 MHz. The overall system noise figure values at 100 MHz for the non-Foster matched antenna system and the gain-enhanced antenna system have been plotted against the electrical size of the antenna in Fig. 5.13. The simulations have been done for two receivers, the first being an ideal noiseless receiver with a noise figure of 0 dB, and the second being a receiver of noise figure 8 dB. It is seen that with a perfect noiseless receiver, the non-Foster matched antenna has a higher overall system

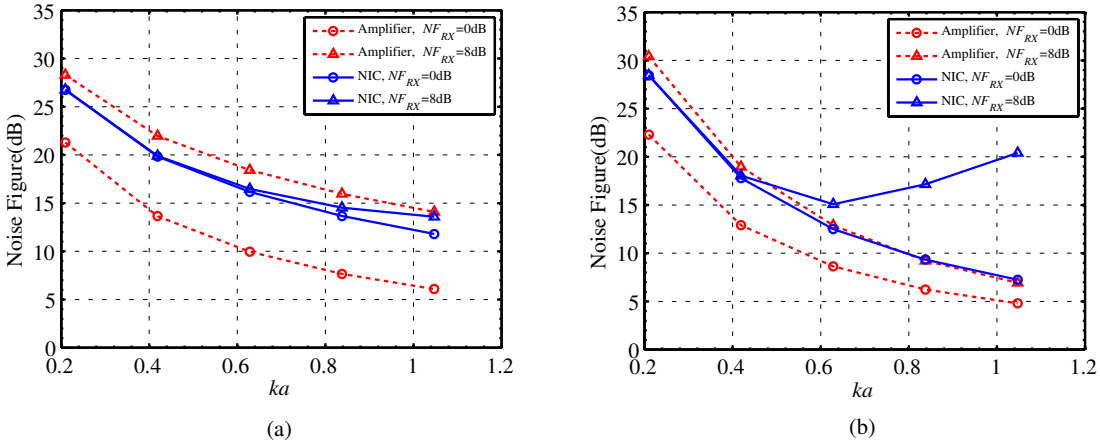

Figure 5.13. (a) Noise figure comparison between a non-Foster matched and gain-enhanced dipole antenna at 100 MHz for different antenna sizes (b) Noise figure comparison between a non-Foster matched and gain-enhanced loop antenna at 100 MHz for different antenna sizes.

noise figure compared to the gain-enhanced antenna, for both the dipole and the loop antenna. With the receiver of noise figure 8 dB, it can be seen from Fig. 5.13(a) that the non-Foster matched dipole antenna has a slightly lower noise figure than the gain-enhanced dipole antenna until the antenna's electrical size approaches 1, at which point the non-Foster matched dipole antenna starts losing its advantage. The corresponding results for the small loop antenna system have been presented in Fig. 5.13(b). Since the loop antenna has a radiation resistance that is proportional to the fourth power of frequency, its radiation resistance becomes significant for electrical sizes greater than 0.5. Further, the inductance of the loop antenna also becomes quite large considering a 2-turn loop, and the required non-Foster inductance and the corresponding generated noise also become substantial for $ka > 0.5$. Therefore with the receiver of noise figure 8 dB, the overall noise figure of the non-Foster matched small loop antenna is lower than that of the gain-enhanced loop antenna only for $ka < 0.5$.

Thus, the conclusion that non-Foster matched antennas do not provide an SNR advantage over gain-enhanced small antennas for low-noise receivers with a noise figure

below say, 6 dB, has been shown to be true for various small antenna sizes.

5.5 Conclusion

The noise analysis and simulations presented in this paper provide explanations as to why our gain and noise measurements indicate no SNR advantage over the passive antenna whereas measurements in [12] indicate otherwise. The measurements in [12] have been done using a receiver of noise figure 8 dB whereas the measurements presented in this paper have been done with a receiver of noise figure 4 dB. Further, it has been conceded in [12] that non-Foster receiving systems provide an SNR advantage over passive systems only in cases where the system is device-noise limited, or when the receiver noise dominates. In this case, the noise generated by the NIC gets masked by the receiver's noise floor and does not affect the overall system noise figure. Further, gain-enhanced passive antennas also have a much larger gain compared to non-Foster matched antennas, resulting in more sensitive systems that can detect lower signal levels. Therefore, non-Foster matched small antennas might not provide an actual performance advantage over gain-enhanced antennas in low-noise receiver systems.

The noise model derived for the NIC is an independent, original model that can be used for noise analysis in any application.

In high power transmit applications, the noise performance of active circuits is not critical. It is instead nonlinearities of the active devices that can lead to a degradation in performance. We will therefore analyze nonlinear effects of the cylindrical slot antenna in the next chapter.

Chapter 5 is based on the following paper which is under review: M. M. Jacob and D. F. Sievenpiper, "Gain and Noise Analysis of Non-Foster Matched Antennas," under review at *Antennas and Propagation, IEEE Transactions on*.

Chapter 6

Non-Foster Matched Antennas for Transmit Applications

Non-Foster circuits (NFCs) are powerful tools to overcome bandwidth and performance limitations of passive antennas and metamaterial stuructures. However, they are active circuits with nonlinear transistors which can introduce undesirable effects at high signal power levels. A non-Foster circuit with very low parasitics and high quality factors can still introduce nonlinearity issues at signal power levels as low as -25 dBm [26]. To determine the distortion or nonlinear characteristics of non-Foster circuits, high power measurements and simulations have been performed for the non-Foster matched cylindrical slot antenna described in Chapter 4. Its broadband matching capability has been examined at varying signal power levels. It has been observed that the NFC impedance changes considerably as the signal power increases, thus reducing its matching capability as well as introducing stability problems for signal power levels above -15 dBm. Two-tone inputs of varying signal power levels were then given to the NFC matched antenna, and the reflected mixing products were measured to analyze stability issues. The alternative to a non-Foster matched antenna with a transmit power amplifier is an unmatched antenna with the same transmit power amplifier as shown in Fig. 6.1. The gain of the two systems was compared for varying input signal power lev-

els. Radiated third order output intercept point (OIP3) simulations were also performed for the two systems. Overall results show that for the particular NFC matched antenna under consideration, the unmatched antenna system has better high-power performance in terms of gain and OIP3, despite being more poorly matched than the NFC matched antenna. However, on increasing the bias current in the NFC design, the OIP3 was found to improve for the NFC matched antenna. Therefore further research needs to be done on optimum design techniques for high-power NFC matched antennas to guarantee minimal gain degradation along with improved stability and OIP3.

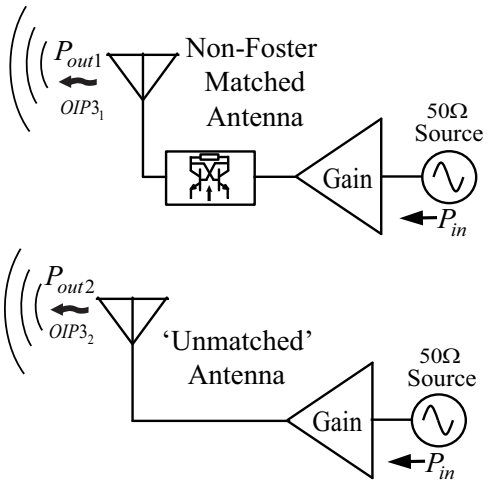

Figure 6.1. Gain-bandwidth product and OIP3 of the non-Foster matched antenna compared to the unmatched antenna with the same amplifier attached to both systems

6.1 Large Signal Input Match and Gain

6.1.1 Large Signal Input Match

Large signal S-parameter simulations were conducted for the NFC matched cylindrical slot antenna for various input signal power levels ranging from -30 dBm to 5 dBm. From the simulation results (Fig. 6.2(a)), it can be observed that at small input power levels (< -25 dBm), the matching bandwidth is the same as that seen in

S-parameter small signal simulations (Fig. 4.6). As the input power increases, the matching begins to degrade, both in terms of S_{11} magnitude as well as matching bandwidth. Thus the matching capability of the NFC becomes less pronounced as the input power increases. At input power levels greater than 5 dBm, the input match is as if the NFC bias were turned off (Fig. 4.6).

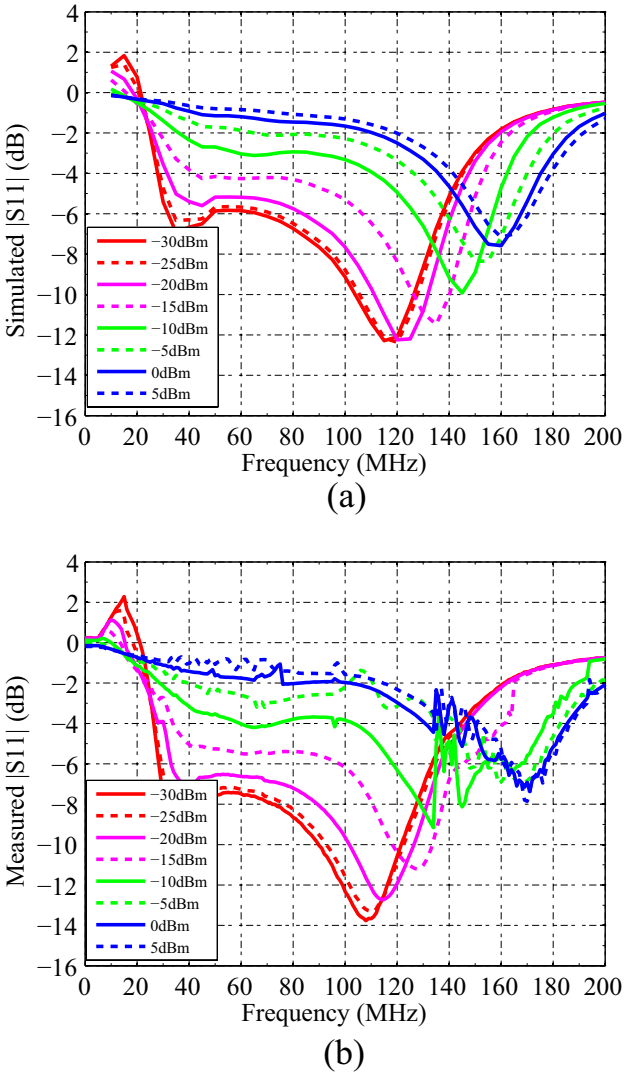

Figure 6.2. (a) Simulated $|S_{11}|$ of the NFC matched antenna for input power levels from -30 dBm to 5 dBm. (b) Measured $|S_{11}|$ of the NFC matched antenna for input power levels from -30 dBm to 5 dBm

These results were verified through measurements, as seen in (Fig. 6.2(b)). It can also been observed that at certain high input power levels, there are measured spikes in the reflection characteristics, corresponding to instabilities at these frequencies. The possible reasons for these instabilities will be discussed in following sections. Performing a smoothing operation on these curves gives similar results to the simulation curves [52]. Thus although harmonic balance simulations can predict most nonlinear effects, transient high power instability could not be accurately simulated.

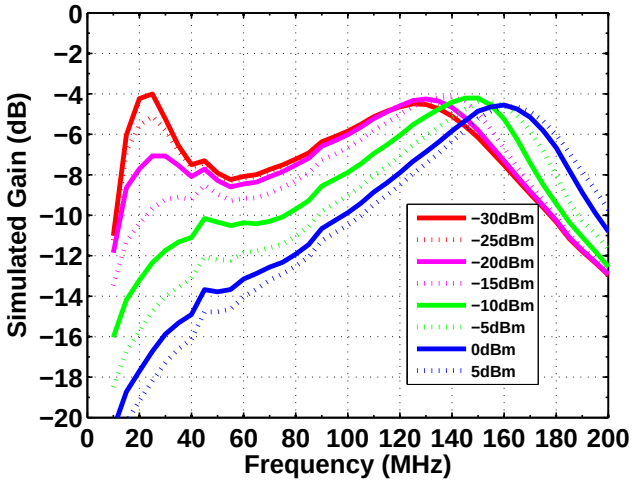

Figure 6.3. Simulated gain from the NFC matched antenna to a 50 ohm receiver for signal power levels from −30 dBm to 5 dBm.

6.1.2 Large Signal Gain

Gain simulations were also done by assigning the 50 ohm receiver input in (Fig. 4.4) as port 2 and the passive antenna as port 1, and computing S_{21} for different input power levels from −30 dBm to 5 dBm (Fig. 6.3). It can be seen that the gain reduces considerably as the input power is increased. This is partly due to the poor input match at high power levels, and also due to the non-ideal NFC impedance at high power levels as seen in Fig. 6.4. As input power increases, the reactance of the NFC deviates from its designed values and the resistive loss increases, leading to an input mismatch

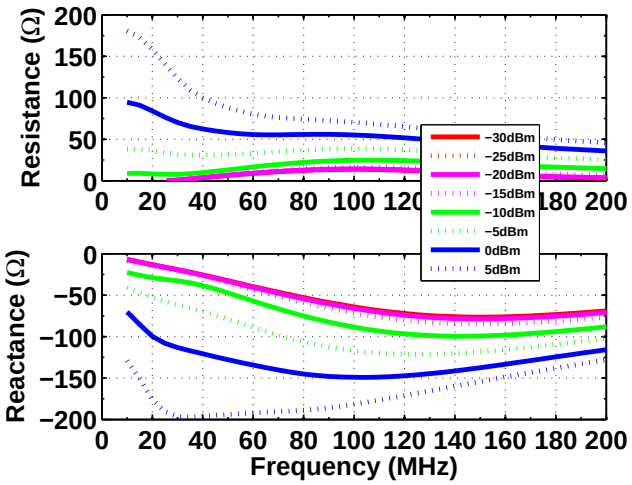

Figure 6.4. Simulated NFC resistance and reactance for input power levels from −30 dBm to 5 dBm.

and a loss in gain. The high power NFC impedance magnitude is seen to be much higher than the low power impedance magnitude, and therefore this does not violate the short circuit stable condition of the NFC. To further investigate the cause of instabilities, high power two-tone measurements were performed.

6.2 Harmonics and Mixing Products at High Power

Typically, a two-tone measurement in a nonlinear system yields harmonics of the two tones, along with 2^{nd} order and 3^{rd} order mixing products, according to the following power series expansion for distortion [51]

$$V_{out} = a_1 V_{in} + a_2 {V_{in}}^2 + a_3 {V_{in}}^3 ..., \tag{6.1}$$

where, a_1, a_2 , a_3 etc are the first-order, second-order and third-oder coefficients of nonlinearity. Highly nonlinear systems have nonlinearity coefficients of the fourth order and higher, leading to a greater number of mixing products in the output.

In a radiating system, it is difficult to measure radiated mixing products gener-

ated by active circuits before the antenna. One reason is that the generated harmonics and mixing products are typically about 20 dB or more below the power of the fundamental tones, and therefore it becomes harder to measure low power radiated mixing products. Another reason is that the antenna acts like a natural filter due to the frequency dependence of the gain, with the harmonics seeing much lower gain than the fundamental tones. Therefore in order to capture most of the nonlinear harmonics and mixing products generated by the non-Foster circuit attached to the antenna, a measurement setup was devised to measure the reflected mixing products instead of the radiated mixing products as shown in Fig. 6.5(a).

6.2.1 Measured Reflected Mixing Products

Two signal generators generate two independent tones P_{in_1} and P_{in_2} that are combined in a splitter. The combined two-tone input is then sent through a coupler to the NFC matched antenna. The reflections from the NFC are measured using a spectrum analyzer at the coupled port as shown in Fig. 6.5(a). The coupler used in the setup was a -10 dB 3-port directional coupler (Mini Circuits ZFDC-10-1+),with the 'input port' attached to the NFC matched antenna to measure the coupled reflected mixing products.

To verify this setup, simulations were done with a two-tone input of 99 MHz and 100 MHz (at the mid-band of the matching bandwidth of the cylindrical slot antenna Fig. 6.2) with both inputs at -17 dBm and using measured models for the splitter and the coupler. Taking into account the 3 dB loss of the splitter, the input tones going into the coupler are each at -20 dBm. At this input power level, the second order harmonics were visible, along with the typical 'Christams tree' of mixing products around the fundamental tones and the second harmonic tones. For visual clarity, only the fundamental tones have been shown along with the mixing products around them in Fig. 6.5(b). The simulations closely matched with the measured results as shown.

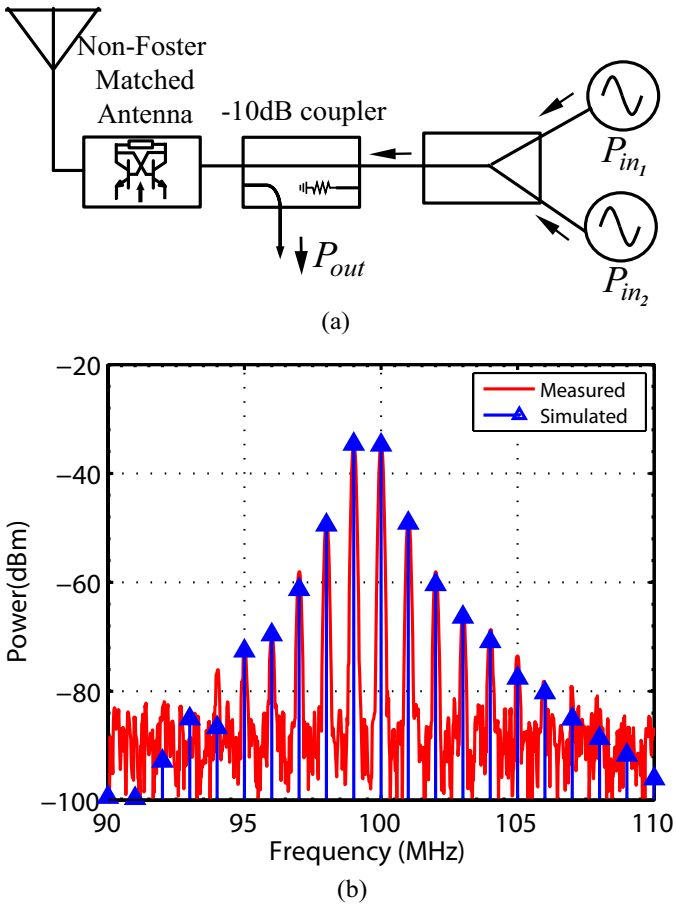

Figure 6.5. (a) Experimental setup to measure reflected nonlinear mixing products from the non-Foster matched antenna. (b) Simulation and measurement results of the reflected mixing products for the setup shown where P_{in1} is 99 MHz at -17 dBm and P_{in2} is 100 MHz at -17 dBm.

The large number of mixing products around the fundamental tones indicate the high nonlinearity of the NFC. This was confirmed on increasing the power of the input tones. When the input is a single tone of 99 MHz at 0 dBm (Fig. 6.6(a)), the reflected coupled power at the spectrum analyzer shows only the fundamental tone and the second harmonic. When a two-tone input is sent, with the addition of 100 MHz at 0 dBm, the reflected power shows mixing products across a wide range of frequencies as shown in Fig. 6.6(b), instead of the typical 'Christmas tree' profile. This could be due to the mixing products mixing amongst themselves due to the positive feedback within the

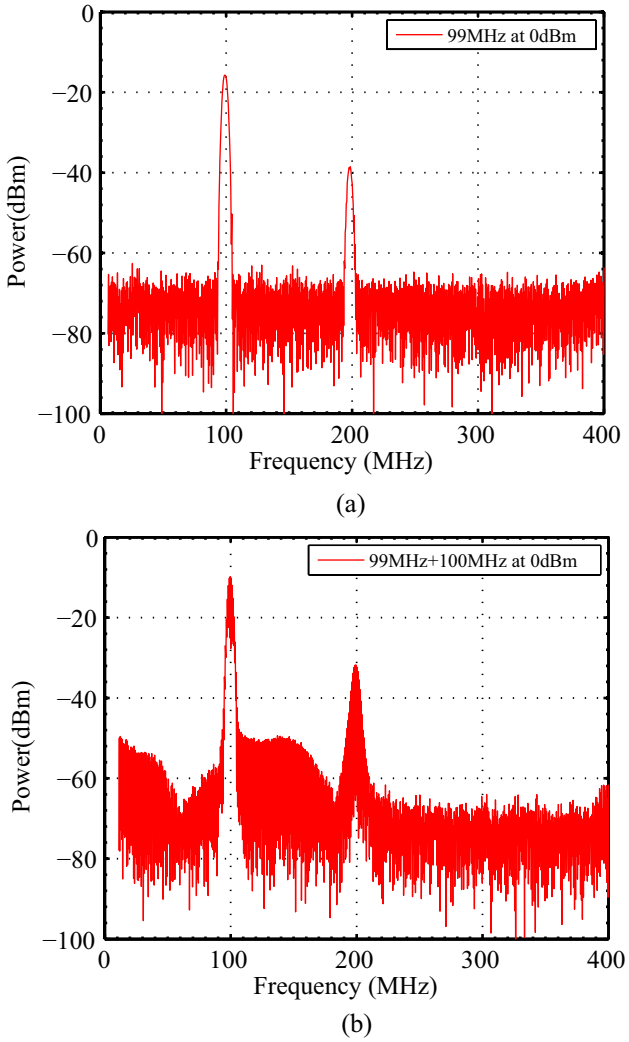

Figure 6.6. (a) Coupled reflected power for a single tone input with P_{in1} of 99 MHz at 0 dBm in Fig. 6.5. (b) Coupled reflected power for a two-tone input with P_{in1} of 99 MHz at 0 dBm and P_{in2} of 100 MHz at 0 dBm in Fig. 6.5.

NFC, generating new mixing products of various frequencies.

It should also be noted that at high power, the harmonic balance simulations cannot accurately predict measurement results unless a very large mixing order is enabled in the simulations (due to the positive feedback effect). Current resources did not enable us to perform simulations with the mixing order required to generate mixing products across the wide range of frequencies seen in the 0 dBm input measurements.

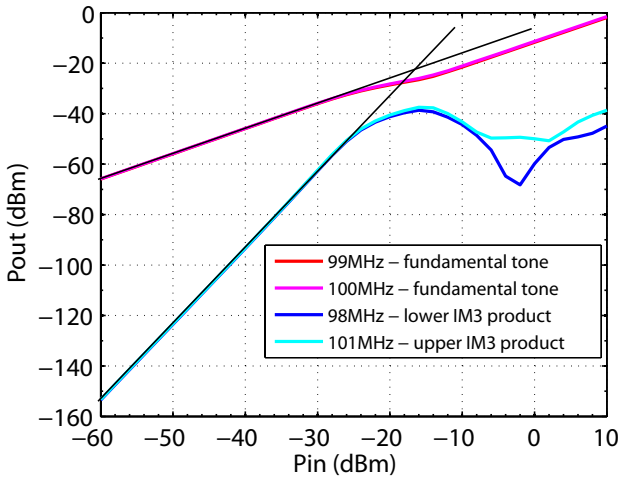

Figure 6.7. Simulation results for the non-Foster matched antenna showing the fundamental radiated tone along with the radiated third order mixing product.

6.2.2 Simulated Two-tone Radiated Distortion Products

Two-tone simulations were performed for the NFC matched antenna to analyze the power of the radiated fundamental tones versus the power of the radiated 3^{rd} order intermodulation product. Two tones of f_1=99 MHz and f_2=100 MHz were sent to the input of the NFC matched antenna, and the radiated fundamental tones f_1 and f_2 were calculated, along with the lower IM3 product $2f_1 - f_2$ and the upper IM3 product $2f_2 - f_1$. Care must be taken to ensure that the power calculation takes into account the frequency dependent impedance of the antenna. The simulated results are shown in Fig. 6.7.

A visual inspection of Fig. 6.7 shows that the extrapolated third order intermodulation product intersects the fundamental tone at around $P_{in} = -16$ dBm. This gives the third order intermodulation input intercept point (IIP3). The third order intermodulation output intercept point (OIP3) is given by the output of the extrapolated linear fundamental power at the IIP3, which is equivalent to -22 dBm as seen in Fig. 6.7. The reason for the OIP3 being lower in power than the IIP3 is that the NFC matched antenna has a

gain lower than 1 (The maximum gain of an antenna is 1, whereby all the input power is radiated).

The OIP3 can also be calculated using the following equations.

$$OIP3_{low}(\text{dBm}) = P(f_1) + 0.5\,(P(f_2) - P(2f_1 - f_2)) \tag{6.2}$$

$$OIP3_{high}(\text{dBm}) = P(f_2) + 0.5\,(P(f_1) - P(2f_2 - f_1)) \tag{6.3}$$

In the above equations, $P(f_1)$ is the output power of the lower fundamental tone (in dBm), $P(f_2)$ is the output power of the upper fundamental tone (in dBm), $P(2f_1 - f_2)$ is the output power of the lower IM3 product (in dBm) and $P(2f_2 - f_1)$ is the output power of the upper IM3 product (in dBm). $OIP3_{low}$ and $OIP3_{high}$ should be identical for a systems where the gain is invariant across the frequencies from $2f_1 - f_2$ to $2f_2 - f_1$. Due to the small gain variation of the NFC matched antenna across these frequencies, the two values of OIP3 are not exactly the same, but have variations under 0.3 dBm. The simulations required for the power values in the OIP3 calculations must be performed at well below the compression point of the NFC matched antenna to guarantee accurate results.

The IIP3 can be calculated as

$$IIP3_{low}(\text{dBm}) = OIP3_{low}(\text{dBm}) - Gain(\text{dB}) \tag{6.4}$$

The simulated IIP3 of -16 dBm is quite low compared to most high power amplifiers. But more worrying is the presence of instabilities at power levels greater than -15 dBm.

6.3 Reason for High Power Instability

One of the reasons for high power instability could be the large number of mixing products generated across the bandwidth of operation due to positive feedback and self-mixing. This could manifest itself as 'instability' in S_{11} measurements as seen in Fig. 6.6(b).

Another reason could be observed from the IM3 products in Fig. 6.6. The IM3 starts to deviate from its linear curve and starts to dip at input power levels around -15 dBm. This could be explained by the cancellation of the IM3 products from the 3^{rd} order term a_3 by the 5^{th} order term a_5 as seen from the following equation

$$IM3 = \frac{3}{4}a_3{V_{in}}^3 + \frac{25}{8}a_5{V_{in}}^5 \ldots \tag{6.5}$$

While these sweet spots are good for choosing power levels with very good linearity (low IM3 power levels compared to the fundamental tones), they are also spots where a gain expansion occurs instead of gain compression. This can be understood from the fact that gain compression at high power (denoted by the $P-1$dB level) is typically due to a_3. When the contribution from a_5 starts cancelling that from a_3, a gain expansion occurs instead of a gain compression. This effect is noticeable in the fundamental power at around -15 dBm in Fig. 6.7, where a slight dip in the fundamental power is followed immediately by a slight increase. This gain expansion could cause unexpected effects when coupled with positive feedback.

Thirdly, the nonlinear intrinsic capacitances (base-emitter, base-collector and substrate capacitances) in the transistors vary with varying power levels. The values of these capacitances determine the location of the poles in the NFC network impedance function. As the input power increases, the changing values of the capacitances change the impedance of the NFC. This could possibly force the poles to move from a stable

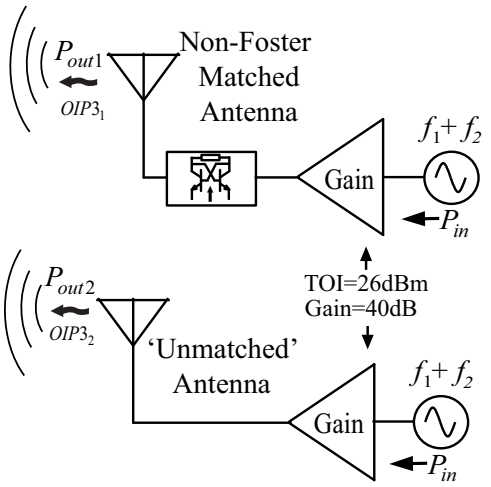

Figure 6.8. Gain-bandwidth product and OIP3 of the non-Foster matched antenna compared to the unmatched antenna with the same amplifier attached to both systems

region to an unstable region in the complex frequency plane, depending on the swamping impedance. Although the short circuit stability conditions were not violated at high power in this particular NFC matched antenna design, care should be taken to determine that the NFC impedance at high power satisfies stability conditions.

Further studies need to be done on high power instability to determine if it simply a manifestation of generated mixing products from extreme nonlinearity, or if the variation in device gain and parasitics cause unexpected instability issues.

6.4 NFC Matched Antenna vs. Unmatched Antenna

To determine the true advantage of NFC matched antennas attached to a power amplifier in transmit applications, they should be compared to the unmatched antenna attached to the same amplifier. The main parameters to be compared to establish a figure of merit are the output power and the OIP3 of the two systems across the bandwidth under consideration.

The simulations were performed by attaching the non-Foster matched antenna to a measured model of an amplifier with an OIP3 of 26 dBm and a gain of 40 dB under

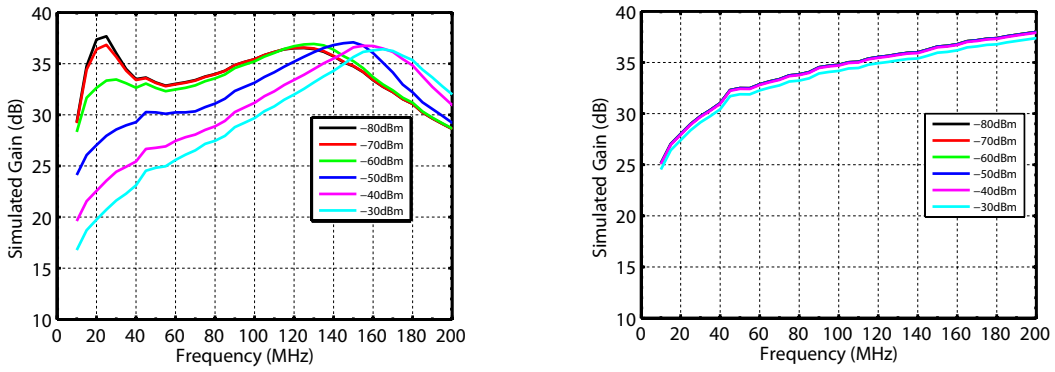

Figure 6.9. (a) Simulated gain of the NFC matched antenna system for various signal power levels. (b) Simulated gain of the unmatched antenna system for various signal power levels

matched conditions. The unmatched antenna was then attached to the same amplifier and two-tone simulations were performed for both (Fig. 6.1).

6.4.1 Gain (P_{out}) Comparison

Fig. 6.9 presents simulated gain for the two systems for varying input power levels. The input power levels are very low to take into account the 40 dB gain of the amplifier.

It can be seen from Fig. 6.9(a) that the gain variation of the NFC matched antenna system is very similar to the gain variation shown in Fig. 6.3 for the NFC matched antenna by itself , indicating that the amplifier attached to the NFC matched antenna does not degrade the linearity of the system significantly. This is further reinforced in Fig. 6.9(b) for the gain variation of the unmatched antenna attached to the same amplifier. It can be seen that the gain does not vary for the unmatched antenna system for almost all input power levels under consideration. A comparison of the gain variation for the two systems shows that although the NFC matched antenna system has higher gain (and therefor higher P_{out}) for lower input power levels, the unmatched antenna systems

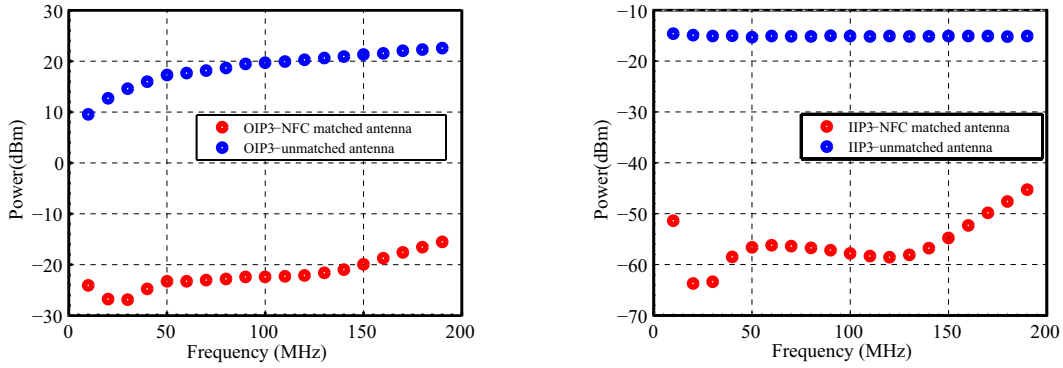

(a) (b)

Figure 6.10. (a) Simulated OIP3 of the NFC matched antenna system compared to that of the unmatched antenna system. (b) Simulated IIP3 of the NFC matched antenna system compared to that of the unmatched antenna system.

delivers higher P_{out} at higher power levels.

6.4.2 OIP3 and IIP3 Comparison

OIP3 and IIP3 simulations were performed for the setup shown in Fig. 6.1 for the bandwidth under condsideration, and the results are presented in Fig. 6.10. In all simulations,the fundamental tones f_1 and f_2 have a 1 MHz separation. The OIP3 results shown in Fig. 6.10(a) indicate that the OIP3 of the unmatched antenna systems is much higher than the OIP3 of the NFC matched antenna system. The IIP3 of the unmatched antenna systems is also much higher than the IIP3 of the NFC matched antenna system across the bandwidth under consideration (Fig. 6.10)(b).

Therefore the results indicate that at high power, the unmatched antenna system with the amplifier delivers higher P_{out} and also has lower IM3 products in terms of better OIP3 and IIP3.

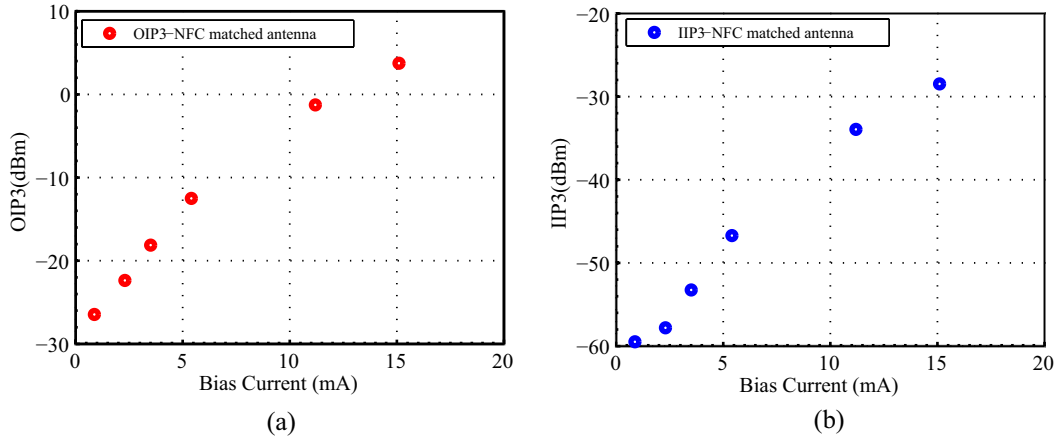

Figure 6.11. (a) Simulated OIP3 of the NFC matched antenna for various bias currents (b) Simulated IIP3 of the NFC matched antenna for various bias currents

6.5 Linearity Improvement Techniques for the NFC Matched Antenna

A typical brute force linearization technique is to increase the bias current in the active devices. On increasing the bias current I_c for the two transistors in the NFC matching network by increasing the bias voltage, the OIP3 and IIP3 of the NFC matched antenna system (including the amplifier) has been found to increase almost exponentially with bias current for small initial increments in bias current as shown in Fig. 6.11. The simulations have been done for a two-tone input of f_1=99 MHz and f_2=100 MHz. However, for large bias currents, the OIP3 and IIP3 is seen to saturate. Therefore for this particular NFC matched antenna system, it might not be possible to exceed the 20 dBm OIP3 of the unmatched antenna system for the same input frequencies shown in Fig. 6.10(a). The simulations have not taken into account the stability of the NFC at these bias conditions. At higher bias currents, achieving stability can be a challenge due to the increased gain of the transistors. However, it might be possible to improve the linearity of the NFC matched antenna using other bias topologies.

6.6 Conclusion

The effects of nonlinearity in an NFC matched antenna have been identified in terms of match degradation, gain degradation and potential instability. A performance merit has been established for an NFC matched transmit antenna by comparing it to an unmatched antenna for the same transmitting system. Simulations on overall system gain and OIP3 indicate that at low bias currents, the unmatched antenna is superior to the NFC matched antenna at high power. However, high bias currents for the NFC indicate much greater improvement in IP3. Therefor optimum design techniques should be studied in order to achieve broadband non-Foster matched transmit antennas with high gain and high linearity.

Chapter 6 is based on the following papers: M. M. Jacob, J. Long, and D. F. Sievenpiper, "Nonlinear effects of non-Foster matching networks," in *Antennas and Propagation and USNC/URSI National Radio Science Meeting, 2015 IEEE International Symposium on*, 2015, pp. 1248-1249 ; M. M. Jacob and D. F. Sievenpiper, "Non-Foster Matched Antennas for High-Power Applications," in preparation.

Chapter 7

Conclusion

7.1 Summary of Work

This thesis presents a comprehensive overview of the advantages and limitations of non-Foster circuits in small antenna applications.

Chapter 1 presents the theory of the Wheeler-Chu bandwidth limits for small antennas and introduces the need for non-Foster circuits.

Chapter 2 presents the design, simulation and measurement of fixed and tunable non-Foster circuits. Applications of these circuits for broadband matching and for reduction of phase dispersion have been explained.

Chapter 3 introduces a non-Foster loaded parasitic array designed to reduce phase dispersion and obtain squint-free patterns. Measured results show that the non-Foster loaded parasitic array can be used to obtain almost 2:1 instantaneous squint-free bandwidth compared to typical 10-15% squint-free bandwidths of passive parasitic arrays.

Chapter 4 illustrates broadband non-Foster matching with two design examples for non-Foster matched small antennas whose matching bandwidth exceeds the Wheeler-Chu bandwidth limit.

Chapter 5 analyzes limitations of non-Foster matched antennas in receive appli-

cations. An objective study has been done to determine the true advantage of non-Foster matched antennas attached to a receiver by comparing the received signal to noise ratio (SNR) against that of an unmatched antenna attached to an amplifier and a receiver. An independent noise model for a generalized non-Foster circuit has been derived to be used in any application. The studies show that non-Foster matched antennas might provide an SNR advantage only when the system is externally noise limited by high-noise receivers.

Chapter 6 analyzes imitations of non-Foster matched antennas in transmit applications. Distortion effects such as matching and gain degradation have been shown. A non-Foster matched transmit antenna attached to an amplifier has then been compared to the unmatched antenna attached to the same amplifier. Third order output intercept point simulations and high power gain simulations have been performed across the bandwidth under consideration for both systems to determine the true advantage of non-Foster matched antennas in the transmit mode. The results indicate that with the optimum design to ensure high power stability and linearity, non-Foster matched transmit antennas could be a competitive alternative to a passive antenna.

7.2 Future Work

A small signal noise model has been developed in this thesis to identify noise limitations in small signal non-Foster applications. A similar large signal nonlinear model needs to be developed for the non-Foster circuit to be used in high power applications. This model should be able to identify optimum biasing conditions which would yield the required gain, bandwidth and OIP3, in addition to being stable at high power.

Although non-Foster matched antennas might yield a performance advantage only in certain environments for receive applications (high external noise), non-Foster circuits have valuable potential in other applicaions such as fast wave propagation in su-

perluminal waveguides [34], and slow wave propagation in artifical impedance surfaces [53]. They are also useful in achieving a broadband impedance match in applications where added noise is less critical and in sufficiently low-power applications where linearity issues do not arise.

Future progress on non-Foster circuits would need to include self-tuning non-Foster circuits for reconfigurable antennas [54], and integrated circuit designs for high frequency applications [55].

Bibliography

[1] H. A. Wheeler, "Fundamental limitations of small antennas," *Proceedings of the IRE*, vol. 35, no. 12, pp. 1479–1484, 1947.

[2] ——, "Small antennas," *Antennas and Propagation, IEEE Transactions on*, vol. 23, no. 4, pp. 462–469, 1975.

[3] L. J. Chu, "Physical limitations of omnidirectional antennas," *Journal of Applied Physics*, vol. 19, no. 12, pp. 1163–1175, 1948. [Online]. Available: http://scitation.aip.org/content/aip/journal/jap/19/12/10.1063/1.1715038

[4] R. C. Hansen, "Fundamental limitations in antennas," *Proceedings of the IEEE*, vol. 69, no. 2, pp. 170–182, 1981.

[5] J. S. McLean, "A re-examination of the fundamental limits on the radiation q of electrically small antennas," *Antennas and Propagation, IEEE Transactions on*, vol. 44, no. 5, p. 672, 1996.

[6] R. E. Collin and S. Rothschild, "Evaluation of antenna q," *Antennas and Propagation, IEEE Transactions on*, vol. 12, no. 1, pp. 23–27, 1964.

[7] A. D. Yaghjian and S. R. Best, "Impedance, bandwidth, and q of antennas," *Antennas and Propagation, IEEE Transactions on*, vol. 53, no. 4, pp. 1298–1324, 2005.

[8] D. F. Sievenpiper, D. C. Dawson, M. M. Jacob, T. Kanar, K. Sanghoon, L. Jiang, and R. G. Quarfoth, "Experimental validation of performance limits and design guidelines for small antennas," *Antennas and Propagation, IEEE Transactions on*, vol. 60, no. 1, pp. 8–19, 2012.

[9] R. M. Fano, "Theoretical limitations on the broadband matching of arbitrary impedances," *Journal of the Franklin Institute*, vol. 249, no. 1, pp. 57–83, 1950.

[10] H. Bode, *Network Analysis and Feedback Amplifier Design*. Van Nostrand, 1945. [Online]. Available: https://books.google.com/books?id=kSYhAAAAMAAJ

[11] R. M. Foster, "A reactance theorem," *Bell System Technical Journal*, vol. 3, no. 2, pp. 259–267, 1924.

[12] S. E. Sussman-Fort and R. M. Rudish, "Non-foster impedance matching of electrically-small antennas," *Antennas and Propagation, IEEE Transactions on*, vol. 57, no. 8, pp. 2230–2241, 2009.

[13] M. M. Jacob, J. Long, and D. F. Sievenpiper, "Non-foster loaded parasitic array for broadband steerable patterns," *Antennas and Propagation, IEEE Transactions on*, vol. 62, no. 12, pp. 6081–6090, 2014.

[14] L. Jiang, M. M. Jacob, and D. F. Sievenpiper, "Broadband fast-wave propagation in a non-foster circuit loaded waveguide," *Microwave Theory and Techniques, IEEE Transactions on*, vol. 62, no. 4, pp. 789–798, 2014.

[15] D. F. Sievenpiper, "Superluminal waveguides based on non-foster circuits for broadband leaky-wave antennas," *Antennas and Wireless Propagation Letters, IEEE*, vol. 10, pp. 231–234, 2011.

[16] H. Mirzaei and G. V. Eleftheriades, "Arbitrary-angle squint-free beamforming in series-fed antenna arrays using non-foster elements synthesized by negative-group-delay networks," *Antennas and Propagation, IEEE Transactions on*, vol. 63, no. 5, pp. 1997–2010, 2015.

[17] J. G. Linvill, "Transistor negative-impedance converters," *Proceedings of the IRE*, vol. 41, no. 6, pp. 725–729, 1953.

[18] A. Larky, "Negative-impedance converters," *Circuit Theory, IRE Transactions on*, vol. 4, no. 3, pp. 124–131, 1957.

[19] T. Yanagisawa, "Rc active networks using current inversion type negative impedance converters," *Circuit Theory, IRE Transactions on*, vol. 4, no. 3, pp. 140–144, 1957.

[20] K. Chang-Kiang and K. Su, "Some new four-terminal nic circuits," *Circuit Theory, IEEE Transactions on*, vol. 16, no. 3, pp. 379–381, 1969.

[21] R. D. Middlebrook, "Null double injection and the extra element theorem," *Education, IEEE Transactions on*, vol. 32, no. 3, pp. 167–180, 1989.

[22] M. Tian, V. Visvanathan, J. Hantgan, and K. Kundert, "Striving for small-signal stability," *Circuits and Devices Magazine, IEEE*, vol. 17, no. 1, pp. 31–41, 2001.

[23] S. D. Stearns, "Incorrect stability criteria for non-foster circuits," in *Antennas and Propagation Society International Symposium (APSURSI), 2012 IEEE*, Conference Proceedings, pp. 1–2.

[24] "Ansys hfss." [Online]. Available: http://www.ansys.com

[25] "Advanced design system." [Online]. Available: http://www.keysight.com

[26] C. R. White, J. W. May, and J. S. Colburn, "A variable negative-inductance integrated circuit at uhf frequencies," *Microwave and Wireless Components Letters, IEEE*, vol. 22, no. 1, pp. 35–37, 2012.

[27] D. C. Youla, "A new theory of broad-band matching," *Circuit Theory, IEEE Transactions on*, vol. 11, no. 1, pp. 30–50, 1964.

[28] M. M. Jacob, L. Jiang, and D. F. Sievenpiper, "Broadband non-foster matching of an electrically small loop antenna," in *Antennas and Propagation Society International Symposium (APSURSI), 2012 IEEE*, Conference Proceedings, pp. 1–2.

[29] I. Frigyes and A. J. Seeds, "Optically generated true-time delay in phased-array antennas," *Microwave Theory and Techniques, IEEE Transactions on*, vol. 43, no. 9, pp. 2378–2386, 1995.

[30] R. F. Harrington, "Reactively controlled directive arrays," *Antennas and Propagation, IEEE Transactions on*, vol. 26, no. 3, pp. 390–395, 1978.

[31] K. Gyoda and T. Ohira, "Design of electronically steerable passive array radiator (espar) antennas," in *Antennas and Propagation Society International Symposium, 2000. IEEE*, vol. 2, Conference Proceedings, pp. 922–925 vol.2.

[32] B. Alshami, H. Aboulnour, and M. Dib, "Design of a broadband espar antenna," in *Microwave Symposium (MMS), 2009 Mediterrannean*, Conference Proceedings, pp. 1–6.

[33] J. D. Kraus, *Antennas*. New York [u.a.]: McGraw-Hill, 1992.

[34] L. Jiang, M. Jacob, and D. F. Sievenpiper, "Electronically steerable antenna using superluminal waveguide and tunable negative capacitors," in *Antennas and Propagation Society International Symposium (APSURSI), 2012 IEEE*, Conference Proceedings, pp. 1–2.

[35] A. Sutinjo, M. Okoniewski, and R. H. Johnston, "An octave band switched parasitic beam-steering array," *Antennas and Wireless Propagation Letters, IEEE*, vol. 6, pp. 211–214, 2007.

[36] R. Schlub and D. V. Thiel, "Switched parasitic antenna on a finite ground plane with conductive sleeve," *Antennas and Propagation, IEEE Transactions on*, vol. 52, no. 5, pp. 1343–1347, 2004.

[37] S. D. Stearns, "Non-foster circuits and stability theory," in *Antennas and Propagation (APSURSI), 2011 IEEE International Symposium on*, Conference Proceedings, pp. 1942–1945.

[38] D. Sievenpiper, M. Jacob, and J. Long, "Active electromagnetic structures, metamaterials, and antennas," in *Antenna Technology (iWAT), 2012 IEEE International Workshop on*, Conference Proceedings, pp. 289–292.

[39] T. Ohira and K. Iigusa, "Electronically steerable parasitic array radiator antenna," *Electronics and Communications in Japan (Part II: Electronics)*, vol. 87, no. 10, pp. 25–45, 2004. [Online]. Available: http://dx.doi.org/10.1002/ecjb.20081

[40] G. Skahill, R. Rudish, and J. Pierro, "Apparatus and method for broadband matching of electrically small antennas," 2000. [Online]. Available: http://www.google.com/patents/US6121940

[41] R. W. Ziolkowski, L. Chia-Ching, J. A. Nielsen, M. H. Tanielian, and C. L. Holloway, "Design and experimental verification of a 3d magnetic ez antenna at 300 mhz," *Antennas and Wireless Propagation Letters, IEEE*, vol. 8, pp. 989–993, 2009.

[42] J. Church, J. C. S. Chieh, X. Lu, J. D. Rockway, and D. Arceo, "Uhf electrically small box cage loop antenna with an embedded non-foster load," *Antennas and Wireless Propagation Letters, IEEE*, vol. 13, pp. 1329–1332, 2014.

[43] C. R. White, J. S. Colburn, and R. G. Nagele, "A non-foster vhf monopole antenna," *Antennas and Wireless Propagation Letters, IEEE*, vol. 11, pp. 584–587, 2012.

[44] M. M. Jacob, L. Jiang, and D. F. Sievenpiper, "Noise in non-foster antenna matching circuits," in *Antennas and Propagation Society International Symposium (APSURSI), 2013 IEEE*, Conference Proceedings, pp. 2205–2206.

[45] C. Stedler, V. Wienstroer, and R. Kronberger, "Noise performance of an antenna matching network with negative-impedance converter (nic)," in *Antennas and Propagation (EuCAP), 2014 8th European Conference on*, Conference Proceedings, pp. 2709–2713.

[46] C. A. Balanis, *Antenna theory : analysis and design*. Hoboken, NJ: Wiley Interscience, 2005.

[47] D. Sailors, "Techniques for estimating the effects of man-made radio noise on distributed military systems," in *In AGARD, Use or Reduction of Propagation and Noise Effects in Distributed Military Systems 14 p (SEE N91-30362 22-32)*, vol. 1, Conference Proceedings.

[48] CCIR, "Characteristics and applications of atmosphericradio noise data," International Radio Consultative Committee,International Telecommunication Union,Geneva, Switzerland, Report 322-2, 1983.

[49] S. R. Best, "Realized noise figure of the general receiving antenna," *Antennas and Wireless Propagation Letters, IEEE*, vol. 12, pp. 702–705, 2013.

[50] P. R. Gray, P. J. Hurst, S. H. Lewis, and R. G. Meyer, *Analysis and design of analog integrated circuits*. Chichester: John Wiley, 2008.

[51] T. H. Lee, *The design of CMOS radio-frequency integrated circuits*. Cambridge: Cambridge University Press, 2009.

[52] M. M. Jacob, L. Jiang, and D. F. Sievenpiper, "Nonlinear effects of non-foster matching networks," in *Antennas and Propagation and USNC/URSI National Radio Science Meeting, 2015 IEEE International Symposium on*, Conference Proceedings, pp. 1248–1249.

[53] L. Jiang and D. Sievenpiper, "Dispersion-reduced high impedance surface loaded with non-foster impedances," in *Antennas and Propagation and USNC/URSI National Radio Science Meeting, 2015 IEEE International Symposium on*, Conference Proceedings, pp. 69–70.

[54] Z. A. Xu, C. R. White, M. W. Yung, Y. J. Yoon, D. A. Hitko, and J. S. Colburn, "Non-foster circuit adaptation for stable broadband operation," *Microwave and Wireless Components Letters, IEEE*, vol. 22, no. 11, pp. 571–573, 2012.

[55] C. R. White and M. W. Yung, "An s-band negative-inductance integrated circuit," in *Microwave Symposium (IMS), 2015 IEEE MTT-S International*, Conference Proceedings, pp. 1–4.

[56] "Avago at41511." [Online]. Available: http://www.avagotech.com/pages/en/rf_microwave/transistors/silicon_bipolar/at-41511/

[57] "Matlab." [Online]. Available: http://www.mathworks.com/

[58] "Modelithics." [Online]. Available: http://www.modelithics.com/

[59] J. T. Aberle and R. Loepsinger-Romak, *Antennas with non-Foster matching networks*. San Rafael, CA: Morgan and Claypool Publishers, 2007.

[60] J. B. Andersen and S. Berntsen, "Comments on "the foster reactance theorem for antennas and radiation q," *Antennas and Propagation, IEEE Transactions on*, vol. 55, no. 3, pp. 1013–1014, 2007.

[61] E. Brookner and J. M. Howell, "Right way to calculate reflector and active-phased-array antenna system noise temperature taking into account antenna mismatch," in *Phased Array Systems and Technology, 2003. IEEE International Symposium on*, Conference Proceedings, pp. 130–135.

[62] J. Brownlie, "On the stability properties of a negative impedance converter," *Circuit Theory, IEEE Transactions on*, vol. 13, no. 1, pp. 98–99, 1966.

[63] H. Y. Chen, C. T. Chan, and P. Sheng, "Transformation optics and metamaterials," *Nature Materials*, vol. 9, no. 5, pp. 387–396, 2010.

[64] G. Fei, Z. Fushun, L. Jiang, M. Jacob, and D. Sievenpiper, "Non-dispersive tunable reflection phase shifter based on non-foster circuits," *Electronics Letters*, vol. 50, no. 22, pp. 1616–1618, 2014.

[65] A. Grbic and G. V. Eleftheriades, "Practical limitations of subwavelength resolution using negative-refractive-index transmission-line lenses," *Antennas and Propagation, IEEE Transactions on*, vol. 53, no. 10, pp. 3201–3209, 2005.

[66] D. J. Gregoire, C. R. White, and J. S. Colburn, "Wideband artificial magnetic conductors loaded with non-foster negative inductors," *Antennas and Wireless Propagation Letters, IEEE*, vol. 10, pp. 1586–1589, 2011.

[67] S. Hrabar, I. Krois, I. Bonic, and A. Kiricenko, "Negative capacitor paves the way to ultra-broadband metamaterials," *Applied Physics Letters*, vol. 99, no. 25, 2011.

[68] S. Keum-Su and R. G. Rojas, "Non-foster impedance matching of electrically small antennas," in *Antennas and Propagation Society International Symposium (APSURSI), 2010 IEEE*, Conference Proceedings, pp. 1–4.

[69] S. Koulouridis and J. L. Volakis, "Non-foster circuits for small broadband antennas," in *Antennas and Propagation Society International Symposium, 2009. APSURSI '09. IEEE*, Conference Proceedings, pp. 1–4.

[70] H. Mirzaei and G. V. Eleftheriades, "An active artificial transmission line for squint-free series-fed antenna array applications," in *Microwave Conference (EuMC), 2011 41st European*, Conference Proceedings, pp. 503–506.

[71] ——, "Antenna applications of non-foster elements," in *Antenna Technology (iWAT), 2012 IEEE International Workshop on*, Conference Proceedings, pp. 281–284.

[72] W. Ng, A. A. Walston, G. L. Tangonan, J. J. Lee, I. L. Newberg, and N. Bernstein, "The first demonstration of an optically steered microwave phased array antenna using true-time-delay," *Lightwave Technology, Journal of*, vol. 9, no. 9, pp. 1124–1131, 1991.

[73] Z. Ning and R. W. Ziolkowski, "Active metamaterial-inspired broad-bandwidth, efficient, electrically small antennas," *Antennas and Wireless Propagation Letters, IEEE*, vol. 10, pp. 1582–1585, 2011.

[74] Y. Ojiro, H. Kawakami, K. Gyoda, and T. Ohira, "Improvement of elevation directivity for espar antennas with finite ground plane," in *Antennas and Propagation Society International Symposium, 2001. IEEE*, vol. 4, Conference Proceedings, pp. 18–21 vol.4.

[75] W. J. Padilla, D. N. Basov, and D. R. Smith, "Negative refractive index metamaterials," *Materials Today*, vol. 9, no. 7-8, pp. 28–35, 2006, iSI Document Delivery No.: 113UH Times Cited: 68 Cited Reference Count: 60 Padilla, Willie J. Basov, Dimitri N. Smith, David R. Padilla, Willie/A-7235-2008; Smith, David/E-4710-2012 Padilla, Willie/0000-0001-7734-8847; 70 Elsevier sci ltd Oxford.

[76] J. B. Pendry, "A chiral route to negative refraction," *Science*, vol. 306, no. 5700, pp. 1353–1355, 2004, 10.1126/science.1104467.

[77] S. A. Ramakrishna, "Physics of negative refractive index materials," *Reports on Progress in Physics*, vol. 68, no. 2, p. 449, 2005. [Online]. Available: http://stacks.iop.org/0034-4885/68/i=2/a=R06

[78] V. M. Shalaev, "Optical negative-index metamaterials," *Nature Photonics*, vol. 1, no. 1, pp. 41–48, 2007.

[79] R. A. Shelby, D. R. Smith, and S. Schultz, "Experimental verification of a negative index of refraction," *Science*, vol. 292, no. 5514, pp. 77–79, 2001. [Online]. Available: http://science.sciencemag.org/sci/292/5514/77.full.pdf

[80] D. R. Smith, J. B. Pendry, and M. C. K. Wiltshire, "Metamaterials and negative refractive index," *Science*, vol. 305, no. 5685, pp. 788–792, 2004, 10.1126/science.1096796. [Online]. Available: http://www.sciencemag.org/content/305/5685/788

[81] D. R. Smith, D. Schurig, M. Rosenbluth, S. Schultz, S. A. Ramakrishna, and J. B. Pendry, "Limitations on subdiffraction imaging with a negative refractive index slab," *Applied Physics Letters*, vol. 82, no. 10, pp. 1506–1508, 2003.

[82] C. Sohl, M. Gustafsson, and G. Kristensson, "Bounds on metamaterials in scattering and antenna problems," in *Antennas and Propagation, 2007. EuCAP 2007. The Second European Conference on*, Conference Proceedings, pp. 1–4.

[83] S. D. Stearns, "Circuit stability theory for non-foster circuits," in *Microwave Symposium Digest (IMS), 2013 IEEE MTT-S International*, Conference Proceedings, pp. 1–3.

[84] S. E. Sussman-Fort, "Non-foster vs. active matching of an electrically-small receive antenna," in *Antennas and Propagation Society International Symposium (APSURSI), 2010 IEEE*, Conference Proceedings, pp. 1–4.

[85] S. E. Sussman-Fort and R. M. Rudish, "Non-foster impedance matching for transmit applications," in *Antenna Technology Small Antennas and Novel Metamaterials, 2006 IEEE International Workshop on*, Conference Proceedings, pp. 53–56.

[86] S. E. Sussman-Fort, "Matching network design using non-foster impedances," *International Journal of RF and Microwave Computer-Aided Engineering*, vol. 16, no. 2, pp. 135–142, 2006. [Online]. Available: http://dx.doi.org/10.1002/mmce.20118

[87] K. F. Warnick and M. A. Jensen, "Signal and noise analysis of small antennas terminated with high-impedance amplifiers," in *Antennas and Propagation, 2007. EuCAP 2007. The Second European Conference on*, Conference Proceedings, pp. 1–6.

[88] G. Wen, P. Jarmuszewski, and Q. Yihong, "The foster reactance theorem for antennas and radiation q," *Antennas and Propagation, IEEE Transactions on*, vol. 48, no. 3, pp. 401–408, 2000.

[89] R. W. Ziolkowski and J. Peng, "Introduction of internal matching circuit to increase the bandwidth of a metamaterial-inspired efficient electrically small antenna," in *Antennas and Propagation Society International Symposium, 2008. AP-S 2008. IEEE*, Conference Proceedings, pp. 1–4.